QUANTIFYING THE ROLE OF LYMPHATICS IN LIPID TRANSPORT AND LYMPHATIC FILARIASIS USING NOVEL ENGINEERING APPROACHES

A Dissertation
Presented to
The Academic Faculty

by

Timothy Kassis

In Partial Fulfillment
of the Requirements for the Degree
Doctor of Philosophy in the
School of Electrical and Computer Engineering

Georgia Institute of Technology
August 2015

QUANTIFYING THE ROLE OF LYMPHATICS IN LIPID TRANSPORT AND LYMPHATIC FILARIASIS USING NOVEL ENGINEERING APPROACHES

Approved by:

Dr. J. Brandon Dixon, Advisor
George W. Woodruff School of Mechanical Engineering
Georgia Institute of Technology

Dr. Philip Santangelo
Wallace H. Coulter Department of Biomedical Engineering
Georgia Institute of Technology

Dr. W. Robert Taylor
Wallace H. Coulter Department of Biomedical Engineering
Georgia Institute of Technology

Dr. Laura O'Farrell
Physiological Research Lab
Georgia Institute of Technology

Dr. Anatoliy Gashev
Department of Medical Physiology
Texas A&M University

Date Approved: May, 26 2015

ACKNOWLEDGEMENTS

Over the course of my Ph.D. I have had a tremendous amount of support from family, friends, mentors and colleagues. Describing and thanking people who have been part of my graduate studies would fill as many pages as my actual thesis. I hope our future interactions demonstrate the extent of my thankfulness. So instead, I'm going to just say:

Thank you to everyone who was part of this experience.

Thank you to God for giving me the opportunity to glorify him and better know Him through his works.

TABLE OF CONTENTS

LIST OF TABLES

LIST OF FIGURES

SUMMARY

The lymphatic system has fundamental physiological roles in maintaining fluid homeostasis, immune cell trafficking and lipid transport from the small intestine to the venous circulation. Lymphatic vessels are the main functional organ responsible for the diverse transport roles the system plays. Unlike the blood vasculature, the lymphatic system does not have a central pump, such as the heart, and relies on a variety of factors to move lymph through. It was long thought that only external factors, such as skeletal muscle contraction and lymph formation, played a role in the functional transport capacity of these vessels. With the advancement of imaging capabilities (both hardware and software), it has become clear in the past two decades or so that the main factor in driving lymph transport is the ability of these vessels to intrinsically contract whereby each vessel is comprised of a chain of 'mini pumps' in series. The functional capacity of these vessels is thus now understood to be primarily determined by this pumping activity that has been shown to be regulated by various mechanical and biochemical cues. Lymphatic vessel dysfunction has been implicated in a variety of diseases including many lipid related pathologies and a neglected tropical disease known as lymphatic filariasis. While it has been possible to study the vessel function in the context of fluid drainage and immune cell trafficking, the capability to understand the role of lymphatic vessels in lipid transport has not been available due to the lack of experimental animal models and acquisition systems. As part of this thesis, we sought to develop an experimental animal model along with hardware and software tools to investigate the interplay between lymphatics and their lipid content. We report the first functional measurements of how vessels respond to elevated lipid loads. We further utilized our engineering expertise to develop an experimental platform allowing us to further understand the parasite known as *B. malayi* that migrates to and resides in lymphatic vessels.

I. Introduction and Literature Survey

1.1 Background and Motivation

The lymphatic vasculature exists in nearly all tissues of the body and plays essential roles in maintaining fluid balance through fluid and protein clearance of the interstitium, in immune cell trafficking, and in lipid transport. Lymphatic vessels achieve these functions through two main types of vessels; initial lymphatics and collecting lymphatics. Initial lymphatics are blind-ended structures comprised of one endothelial cell layer with specialized junctional complexes [1–3]. Initial lymphatics feed into the larger collecting lymphatics that have a smooth muscle media, allowing them to contract [4,5]. Collecting lymphatics also contain unidirectional valves[6] dividing the vessel into segments called lymphangions (**Figure 1**).

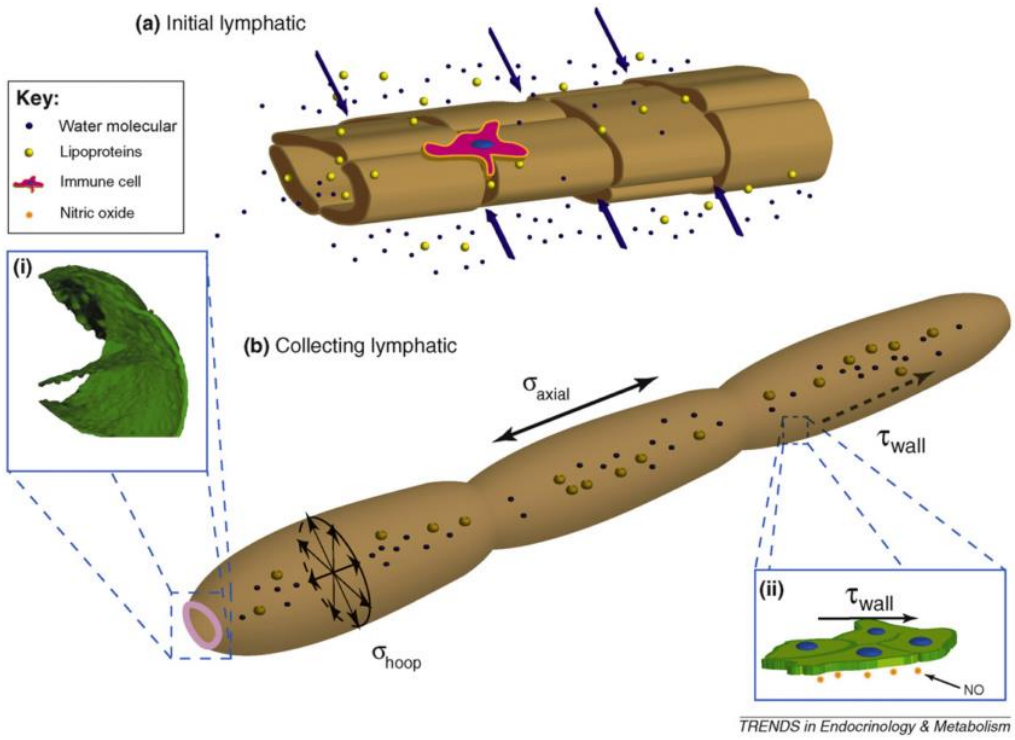

***Figure 1**: Initial lymphatics are made of endothelial cells with specialized overlapping junctions that allow for easy entry of fluid, proteins and cells into the vessel. These lymphatics lack smooth muscle and therefore cannot contract. (b) Collecting lymphatics consist of individual contracting units known as lymphangions, which are lined with smooth muscle and separated by valves. (i) Confocal reconstruction of an isolated rat lymphatic vessel showing valve leaflets (courtesy of Dave Zawieja and Anitoliy Gashev). The collecting vessels are under a variety of mechanical loads: hoop stress (σ_{hoop}), axial stress (σ_{axial}) and wall shear stress (τ_{wall}). These forces have been shown to modulate contractile function. For example, an increase in (ii) wall shear stress through enhanced fluid flow has been shown to cause upregulation of eNOS and subsequent release of NO, which acts as a vasodilator on the smooth muscle and inhibits vessel contraction.[7] Blue spheres are water molecules, yellow spheres are lipoproteins, pink are immune cells, orange stars are NO molecules. (Image taken from Dixon 2010 [8]).*

The collecting vessel's contractile ability, along with the unidirectional valves, result in a pumping mechanism that provides an active transport system to move lymph back into circulation against a pressure gradient. Lymph flow is a consequence of various active (intrinsic) and passive (extrinsic) forces. The phasic contraction of lymphangions accounts for the dominant intrinsic pumping mechanism. Extrinsic factors include the driving force of lymph formation, influences of cardiac and arterial pulsations, contractions of skeletal muscles in proximity to the lymphatic vessels, central venous pressure fluctuations, gastrointestinal peristalsis, and respiration [9]. Previous research has shown that the intrinsic mechanism is regulated through alterations in both intraluminal pressure [10] and wall shear stress, such that increases in wall shear stress imposed through elevated flow inhibit contraction [11] through NO release [7]. Failure of the lymphatic pump results in pathologies ranging from breast cancer-related lymphedema [12] and elephantiasis [13] (**Figure 2**), to intestinal bowl disease (IBD) [14].

Figure 2*: Elephantiasis is a disease resulting from lymphatic filariasis, a parasitic infection of the collecting lymphatics, which manifests itself with dramatic swelling of the lower limbs or genitals. Image courtesy of Maggie Steber (Washington Post)*

Previous studies have shown that after a meal, lipids are broken down into fatty acids and transported into intestinal enterocytes where they are esterified into triglycerides and packaged into hydrophilic lipoproteins called chylomicrons. Once formed, the chylomicrons are then taken up by the lacteals of the intestinal villi and transported through the lymphatic system to the venous circulation [15–19]. Until recently, the lymphatics have been treated as a passive system for the collection and transport of chylomicrons in lymph, without considering their active role in transport [20]. Lymph flow rates, however, have been shown to affect chylomicron transport [21], and lymph flow rate increases after lipid absorption [22]. ***What remains unclear is the exact relationship and molecular underpinnings that modulate lymphatic pump function in the context of the drastic changes in lipid uptake and lymph flow/formation that occur during the normal dietary functions of the intestine***. This information is a vital link in understanding the significance of the lymphatic system in the context of lipid-related diseases and the implications of lymphatic pump failure on the progression and severity of these pathologies.

Malformations of mesentery lymphatics result in various clinical pathologies [23]. A mouse model of lymphatic vasculature dysfunction, which resulted in lymphatic leakage was reported to manifest signs of adult onset obesity [24], thus suggesting compromised lymphatic lipid transport may be a contributing factor to the onset of obesity. Furthermore, protein-losing enteropathies, for example, are characterized by the progressive loss of protein from bowel due to elevated lymphatic pressure, lymphatic congestion and nonulcerative mucosal disease as well as inflammatory and ulcerative diseases. Primary intestinal lymphangiectasia (PIL) is one important form of protein-losing enteropathy. PIL is a disorder characterized by dilated intestinal lacteals which presumably cause lymph leakage into the small bowel lumen. Quantitatively understanding how normal lymphatic pump behavior responds to lipid load will give scientists the basis to compare how this changes, and possibly even drives the pathology, in a PIL diseased state and will provide quantitative data to the extent of leakage, and potentially disease severity. A low-fat diet associated with medium-chain triglyceride

supplementation is the cornerstone of PIL medical management. The absence of fat in the diet prevents chyle engorgement of the intestinal lymphatic vessels thereby preventing their rupture with its ensuing lymph loss. Medium-chain triglycerides are absorbed directly into the portal venous circulation and avoid lacteal overloading [25]. ***A long chain fatty acid (LCFA) fluorescent analogue such as BODIPY C_{16} can be used to better understand how the contribution of loading the lacteals contributes to the disease by investigating the active role that the collecting lymphatic vessel plays to clear the extra load***. Even before PIL symptoms develop, patients have shown delayed transport of lipid from the intestine, suggesting that lymphatic lipid transport function is compromised at an early stage of the disease [23]. In addition, inflammatory bowl diseases (IBDs) such as Crohn's disease (CD), present themselves with several lymphatic abnormalities [14]. Lymphatic contractile activity was shown to be impaired in an isolated vessel model of gut inflammation, suggesting that lymphatic function might be compromised in inflammatory diseases such as CD [8]. While alleviating the lipid burden on lymphatics is clinically beneficial in many of these intestinal disorders, the exact mechanisms of lymphatic failure and the interplay between the lipid absorption process and lymphatic function is unclear.

In addition to the role of lymphatics in lipid transport, there is another research area that is in dire need of further investigation. That area is the disease known as Lymphatic Filariasis (LF). LF is the single largest world-wide source of secondary lymphedema [26] and is caused by adult parasitic nematodes that target and dwell in the lymphatic system. An estimated 120 million people in 73 countries are currently infected, and a further 1.4 billion live in areas where filariasis is endemic [27]. Of the 120 million people harboring the parasites, 90% have *Wuchereria bancrofti*, while *Brugia malayi* and *Brugia timori* infections account for the other 10% [28]. All three parasites use mosquitoes as transmission vectors [29]. Infection is initiated when the host-seeking mosquito deposits an infective third-stage larva (L3) on the skin of the host during the process of obtaining a blood meal. The infective larvae then penetrate the skin at the site of the bite, presumably guided by chemoattractants [30], and migrate to the lymphatic vessels and

lymph nodes of the host where after 6-12 months they mature into adult worms. The adult worms may reside within the lymphatic system for years before the host shows any clinical manifestations such as lymphedema, hydrocele, elephantiasis, chyluria and compromised immunity [31–37]. Following mating in the lymphatics, the parasites release live progeny called microfilariae, which circulate in the bloodstream. These microfilariae can then be ingested by a mosquito during a blood meal, where they undergo development to form L2 and finally L3 larvae. Hence, the life cycle continues [32].

In the year 2000, the World Health Organization (WHO) launched the Global Alliance to Eliminate Lymphatic Filariasis (GAELF). The GAELF has been one of the most rapidly expanding global health programs in the history of public health with the goal of eliminating LF by 2020 through annual mass drug administration (MDA) [27,29,38,39]. ***While killing the adult worms is considered one of the best strategies, the drugs used in MDA are only effective at killing microfilaria, and not the adult worms [40–45]. Thus, breaking the cycle of transmission has proven to be difficult unless we can repurpose current FDA approved drugs as macrofilaricides***. Additionally, these treatment strategies provide no relief for the estimated 120 million people already infected. As we move from controlling the disease to eliminating it, an ***understanding of the mechanisms by which L3 filarial parasites target and migrate towards lymphatics*** and how they behave in the presence of the lymphatic environment will be crucial in developing treatment strategies targeting the migration process as well as the lymphatic-inhabiting adult worms. Developing a better understanding of these parasites will further enable the development of strategies to possibly reverse the damage these parasites have cause in patients that are already suffering from lymphedema as a consequence of the infection [46].

In the following sections we describe various engineering approaches to elucidate the role of lymphatics in both lipid and filarial diseases.

1.2 Research Goals

The overall research goals of this thesis can be separated into two primary objectives:

1. Elucidating the role of collecting lymphatic vessels in lipid uptake and transport both *in vivo* and *in vitro*.
2. Developing a better understanding of filarial parasites, primarily their migration pattern and ways to eliminate the adult version in an effort to limit their lifecycle and subsequent lymphatic vessel damage.

These objectives were further broken down into the following specific goals:

1. Develop an *in vivo* animal model along with the required imaging hardware to acquire both vessel lipid content and functional metrics describing vessel behavior (***Chapter 2***).
2. Quantify the effect of lipid loads on lymphatic vessel function (***Chapter 3***)
3. Measure the post-prandial viscosity of lymph following a high-fat meal to clarify the contribution of changes in viscosity to shear stress (***Chapter 4***)
4. Quantify the sensitivity of lymphatic endothelial cells to shear stress in the context of the microenvironment these cells experience, including oscillatory shear stress and high lipid loads through intracellular calcium signaling (***Chapter 5***).
5. Develop an *in vitro* platform to mimic the skin-lymphatic interface along with an automated imaging platform to quantify the migratory behavior of *B. malayi* within a multicellular microenvironment (***Chapter 6***).

II. DUAL-CHANNEL *IN SITU* OPTICAL IMAGING SYSTEM FOR QUANTIFYING LIPID UPTAKE AND LYMPHATIC PUMP FUNCTION

2.1. Abstract

Nearly all dietary lipids are transported from the intestine to venous circulation through the lymphatic system, yet the mechanisms that regulate this process remain unclear. Elucidating the mechanisms involved in the functional response of lymphatics to changes in lipid load would provide valuable insight into recent implications of lymphatic dysfunction in lipid related diseases. Therefore, we sought to develop an *in situ* imaging system to quantify and correlate lymphatic function as it relates to lipid transport. The imaging platform provides the capability of dual-channel imaging of both high-speed bright-field video and fluorescence simultaneously. Utilizing post-acquisition image processing algorithms, we can quantify correlations between vessel pump function, lymph flow, and lipid concentration of mesenteric lymphatic vessels *in situ*. All image analysis is automated with customized LabVIEW virtual instruments: local flow is measured through lymphocyte velocity tracking, vessel contraction through measurements of the vessel wall displacement and lipid uptake through fluorescence intensity tracking of an orally administered fluorescently labelled fatty acid analogue, BODIPY FL C_{16}. This system will prove to be an invaluable tool for scientists studying intestinal lymphatic function in health and disease, and those investigating strategies for targeting the lymphatics with orally delivered drugs to avoid first pass metabolism.

2.2. Introduction

The lymphatic vasculature exists in nearly all tissues of the body and plays essential roles in maintaining fluid balance through fluid and protein clearance of the interstitium, in immune cell trafficking, and in lipid transport. Lymphatic vessels achieve these desired functions through two main types of vessels; initial lymphatics and the collecting lymphatics. Initial lymphatics are blind-ended structures comprised of one endothelial cell layer with specialized junctional complexes [1–3]. Initial lymphatics feed into the larger collecting lymphatics that have a smooth muscle media, allowing them to be

contractile[4,5]. They also contain unidirectional valves[6] dividing the vessel into segments called lymphangions. The collecting vessels' contractile ability, along with the unidirectional valves, result in a pumping mechanism that provides an active transport system to move lymph back into circulation. It has been shown that this mechanism is regulated through alterations in both intraluminal pressure[10] and wall shear stress, such that increases in wall shear stress imposed through elevated flow inhibit contraction[11].

Dietary lipid uptake and transport after a meal is one of the primary functions of the lymphatic system[16], yet very little is known about the mechanisms through which the lymphatics fulfill these roles. Previous studies have shown that after a meal, lipids are broken up into fatty acids and transported into intestinal enterocytes where they are esterified into triglycerides and packaged into hydrophilic lipoproteins called chylomicrons. Once formed, the chylomicrons are then taken up by the lacteals and transported through the lymphatic system to the venous circulation[15–19]. A mouse model of lymphatic vasculature dysfunction, which resulted in lymphatic leakage was reported to manifest signs of adult onset obesity[24], thus suggesting compromised lymphatic lipid transport may be a contributing factor to the onset of obesity. Until recently, the lymphatics have been treated as a passive system for the collection and transport of chylomicrons in lymph, without considering their active role in transport[20]. Lymph flow rates, however, have been shown to affect chylomicron transport[21], and lymph flow rate increases after lipid absorption[22]. What remains less clear is the exact relationship and molecular underpinnings that modulate lymphatic pump function in the context of the drastic changes in lipid uptake and lymph flow/formation that occur during the normal dietary functions of the intestine. This information is a vital link in understanding the significance of the lymphatic system in the context of lipid-related diseases and the implications of lymphatic pump failure on the progression and severity of these pathologies.

Several models have previously been reported in the literature studying lipid uptake and transport through lymphatics. A tissue-engineered model recapitulates the absorptive properties of the intestinal lymphatic interface using both Caco2 cells

differentiated into enterocytes and lymphatic endothelial cells cultured on opposite sides of a porous membrane[47], but the model does not allow the study of the active role of the lymphatic pump. Various animal models have previously been used to investigate lymphatic development and function including the canine[48], sheep[49–51], rat[52–55], mouse[56,57] and zebrafish[58,59]. Most commonly, rats have been used to quantify lipid absorption[60] which involves the collection of systemic blood to quantify lipoprotein concentrations. Studies over the past two decades have mostly used Bollman's technique[61] for collecting lymph from the mesenteric thoracic duct. Passive collection through the duct could alter the transport time of chylomicrons since these vessels are normally working against a pressure gradient that is no longer present during this preparation. Thus, there is a need for a method for quantifying lipid concentrations that both has minimal effect on the lymphatic vessel and is able to simultaneously provide quantifiable lymphatic pump function measurements.

With the advancement in imaging hardware, computational power and image processing algorithms, it is now possible to use these tools to reliably perform *in situ* lymphatic pump function measurements of lymph flow rate and contraction with reliable accuracy[62–64]. In addition, by combining fluorescence imaging of a fluorescent long chain fatty acid analogue[24,47,65], BODIPY FL C_{16}, one can investigate direct correlations between lymphatic pump function and lipid uptake, and determine the extent to which lipoproteins modulate lymphatic function and in turn the consequences of lymphatic dysfunction to lipid transport and homeostasis. We thus developed a highly sensitive dual-channel optical imaging system capable of acquiring high-speed bright-field video and fluorescence images simultaneously, along with preprocessing and quantitative processing algorithms to extract relative lipid concentrations, vessel pump function metrics, and lymph flow rates, providing the capability to quantitatively elucidate the role of lymphatics in lipid transport.

2.3. Materials and Methods

Dual-Channel Optical Imaging System

A custom-built optical set-up provides dual-channel imaging of both high-speed bright-field video and fluorescence images simultaneously (**Figure 3**). This is achieved through optically dividing the microscope light path into two bands, one for fluorescence (495-550nm) and the other for bright-field (> 560nm). Two light sources are used to illuminate the vessel. A halogen light source built into the microscope (AxioScope, Carl Zeiss Microscopy, Thornwood, NY) offers transmission illumination and a mercury arc lamp (X-Cite, Lumen Dynamics, Ontario, Canada) provides reflective illumination. A band pass excitation filter centered at 475/40nm is positioned in the filter cube within the AxioScope (Zeiss). A 495nm long pass dichroic (Zeiss), also within the cube, allows for reflected light to pass through while restricting the excitation wavelength. A dual phototube adapter (Zeiss) allows us to divide the light path between two ports by using a 560nm long pass dichroic (T555LPXR, Chroma, Bellows Falls, VT). A 530/40nm emission band pass filter (HQ530/40m, Chroma, Bellows Falls, VT) is placed before the fluorescence camera (PIXIS 1024B, Princeton Instruments, Trenton, NJ). An adjustable 60N to C-mount adapter (Zeiss) provides us with the flexibility of aligning the camera in the plane perpendicular to the light path in addition to adjusting focus and angular rotation. A 580nm long pass filter (HQ580lp, Chroma, Bellows Falls, VT) with an optical density (OD) of 5 intercepts the halogen light path and only allows wavelengths greater than 580nm to pass. A 10x water immersion objective (Zeiss) with a numerical aperture (NA) of 0.3 is used to achieve the required magnification.

A high-speed CMOS video camera (Falcon Dalsa VGA300 HG, Teledyne Dalsa, Billerica, MA) allows a frame capturing rate of up to 300 fps with a resolution of 640 x 480 and provides images of individual lymphocytes flowing in the lymph. The 12-bit fluorescence camera utilizes a back-illuminated CCD that is cooled to -70 $^{\circ}$C which eliminates thermal noise and provides high sensitivity, allowing the detection of small changes in fluorescence intensity.

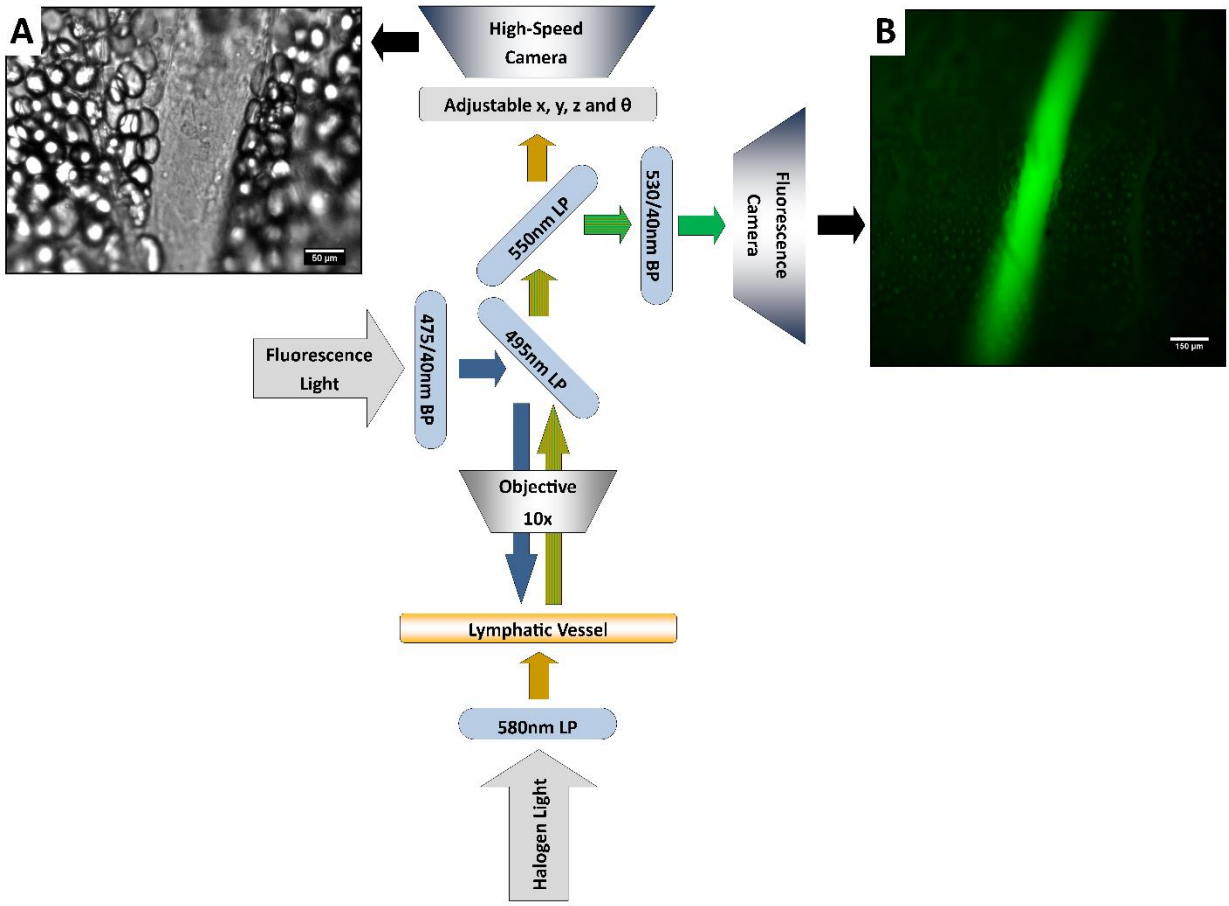

Figure 3: A dual-channel optical system. Both a fluorescence and halogen light source are used to illuminate the vessel. *A long pass filter (580 nm LP) is used to attenuate wavelengths below 580 nm. An excitation band-pass filter (475/40nm BP) is used for the fluorescence light source. A dichroic (550nm LP) effectively splits the wavelengths into two channels; >550nm for the bright-field channel and <550nm for fluorescence. An emission band pass filter (530/40nm) is placed in front of the fluorescence camera. An adjustable adapter allows focusing of the two cameras independently. A) Representative bright-field image from high-speed video of the vessel. B) Representative fluorescence image of the same vessel. BODIPY C_{16}, an orally delivered fluorescent long chain fatty acid analogue, is used as our fluorophore.*

Tissue Phantom Preparation

A 147 µm diameter channel fabricated in polydimethylsiloxane (PDMS; SYLGARD 184, Dow Corning, Midland, MI) served as a mock lymphatic vessel to quantify the minimum detectable concentration of BODIPY FL C_{16} (Life Technologies, Grand Island, NY) with the system and the fluorescence camera's linearity within a given concentration range of BODIPY (Excitation: 490 nm, Emission: 520 nm) in a 10 mg/mL bovine albumin (MP Biomedicals, Auckland, New Zealand) solution. A copper wire running through two holes in a polystyrene petri-dish was used as a PDMS mold. A 10:1 (elastomer to base) PDMS mixture was poured into the mold after removing air bubbles and cured overnight

at 60 ˚C. The wire was then pulled out to create a hollow cylindrical channel thus mimicking a collecting lymphatic vessel in both dimensions and optical clarity.

An Integrated Image Acquisition Platform

Using third-party toolkits (R Cubed Software, Lawrenceville, NJ and BitFlow, Woburn, WA) for both cameras, an integrated image acquisition application was written using LabVIEW (National Instruments, Austin, TX) to streamline the acquisition process with minimal user input. The interface provides a live feed of the high speed video and fluorescence images throughout the experiment. The user can specify the duration of a high-speed video segment, the integration time of the fluorescence camera, and the interval at which to capture for both cameras. Both video sequences and fluorescence images are time-stamped for later processing.

High-speed video is captured at 250 fps using a Neon-CLB PCIe frame grabber (Bitflow, Woburn, MA) and is saved as an uncompressed AVI file. The program uses four memory buffers which, together with RAID 0 hard disks, and an 8-core central processing unit (CPU) configuration allows direct streaming of high-speed video frames to the hard drive without the RAM limitation of the camera or the computer reported previously[64]. This allows the user to capture an unlimited duration of high-speed video that is only limited by available hard disk space. Fluorescence images are captured at an interval of 5 seconds with an integration time of 100, which provides enough sensitivity to image low levels of fluorescence while minimizing blur due to motion artifacts. Images are stored as uncompressed 16-bit TIFF files.

Animal Preparation

A male Sprague-Dawley (SD) rat (Charles River, Wilmington, MA) was chosen to facilitate comparative studies of lymphatic contractility to previous studies performed on the same strain. The animal was housed in an American Association for Accreditation of Laboratory Animal Care facility. At 9 weeks of age weighing 311 g the rat was fasted the night before the experiment for 15 hours while water was available *ad libitum*. After fasting, a solution of 0.5 mL of olive oil (Great Value, Walmart, GA) and 100 µg of BODIPY

FL C_{16}, reconstituted in 20 µL of Dimethyl Sulfoxide (DMSO; Fisher Scientific, Pittsburgh, PA), was delivered via gavage.

After waiting 1.5 hours to allow for digestion, the rat was sedated with an intramuscular (IM) injection of Diazepam (2.5 mg/Kg, Hospira, Lake Forest, IL) and then anesthetized through an IM injection of a cocktail containing 0.12 mL/kg Fentanyl (Sigma Aldrich, St. Louis, MO) and 6 mL/kg Droperidol (Sigma Aldrich, St. Louis, MO) which has been previously observed to have minimal effect on lymphatic vessel contractility. Supplemental IM booster doses at half the initial dose were administered as needed. After preparing a surgical area around the abdominal cavity, a 2 cm incision was made at the midline starting 1 cm below the Xiphoid process. A segment of the small intestine distal to the duodenum was exteriorized and stabilized in a groove between two acrylic plates thus exposing the mesentery over an imaging window covered with a glass slide (**Figure 4**). An albumin physiological salt solution (APSS; in mM: 145.0 NaCl, 4.7 KCl, 2.0 $CaCl_2$, 1.2 $MgSO_4$, 1.2 NaH_2 PO4 , 5.0 glucose, 2.0 sodium pyruvate, 0.02 EDTA, 3.0 MOPS, and 10 g/L BSA) (all reagents from Sigma, St. Louis, MO and BSA from ICP Bio, New Zealand) with pH adjusted to 7.4 ± 0.1 at 38 $^{\circ}$C was temperature controlled at 36 $^{\circ}$C to 39 $^{\circ}$C and flowed at a rate of 12 mL/min to bathe the mesentery. The APSS bath recapitulates the oncotic extracellular environment found around the mesentery. The temperature of the rat was maintained through circulating hot water flowing in silicone tubing underneath the animal within the custom designed imaging board while body temperature was monitored and recorded with a rectal thermometer (Kent Scientific, Torrington, Connecticut). A lymphatic vessel was then located and placed over the imaging window allowing the imaging session to begin. Imaging was performed for a total of 70 minutes. All animal procedures were performed in accordance with the Georgia Institute of Technology Internal Animal Care and Use Committee and complied with the National Institutes of Health Guide for the Care and Use of Laboratory Animals. At the end of the experiment the rat was euthanized.

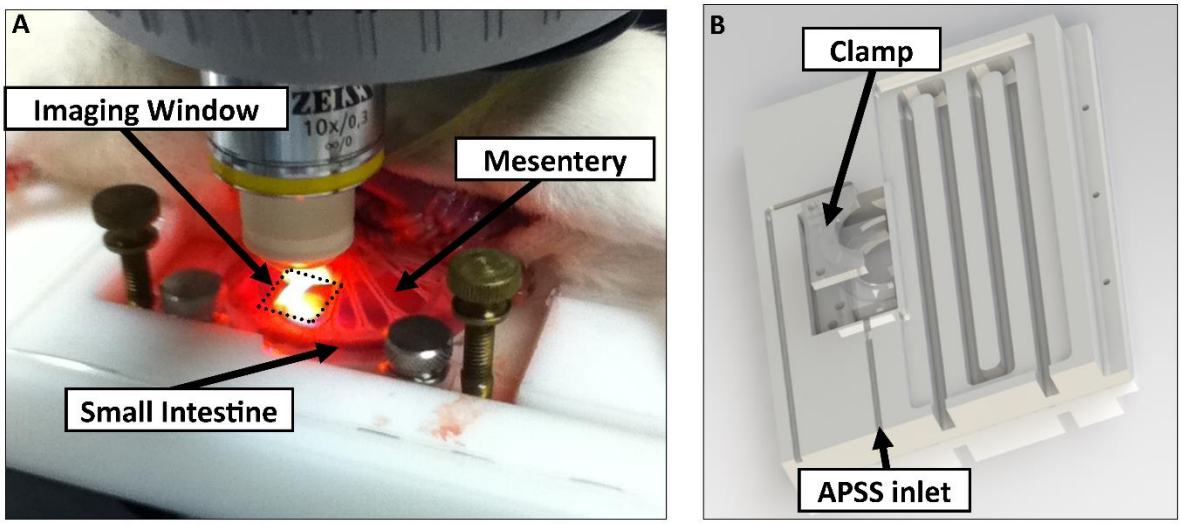

Figure 4: The surgical set-up. *A) The small intestine is stabilized in a loop via a two-piece clamp thus exposing the mesentery. The base of the platform is a glass slide which forms the imaging window. B) A custom designed imaging board that allows us to image the mesentery while bathing it in a circulating albumin physiological salt solution (APSS). The animal sits on a heated platform, which maintains the animal's core body temperature. The board is screwed into the microscope stage to insure long term field-of-view stability by limiting slight board movements.*

Post-Acquisition Image Processing

Lipid Intensity

Utilizing the fluorescence images, we defined a region of interest (ROI) in the middle of the vessel and quantified the mean pixel intensity over time to track the relative intensity of BODIPY C_{16}. The ROI spatially averages the fluorescent pixels in the x-y plane and is typically drawn as a square to encompass a maximum area within the vessel. A cross-correlation (CC) algorithm was implemented to track the same vessel region in every frame to compensate for vessel motion artifacts. Intensity values were averaged over a 35 second period (7 frames), which allows for sufficient imaging of the physiological changes in lipid concentration that occur on a much longer timescale, allowing us to correct for focus fluctuations due to motion artifacts.

Motion Compensation

Intestinal peristalsis greatly increases after a meal[66], which when coupled with the rat's respiration, introduces significant motion artifacts. While most researchers perform lymphatic pump function measurements on a fasted rat to minimize these effects[63], the

purposes of this study required the development of a multitemporal motion compensation algorithm that can be used to preprocess the video for subsequent analysis. Area-based methods are preferably applied when the images do not have many prominent details and the distinctive information is provided by graylevels/colors rather than by local shapes and structure[67]. An area-based intensity-based 2D cross-correlation (CC) image registration method was chosen over other methods as it was the least prone to changes due to loss of focus. A 100 x 100 pixel template window was drawn on the initial frame in the video sequence and the CC coefficient was calculated for the subsequent frames to find the best possible match above a correlation index threshold of 0.1. Such a low correlation is seen when the vessel is significantly out of the plane of focus. An image with correlation index <0.1 is not processed and instead is left as is. This does not affect diameter and velocity readings as those two algorithms ignore large frame shifts due to their inherent use of small CC windows for their processing. Once the best match was located, the image was offset in the x-y plane to overlap the original template window. The variability in adipocyte (fat cells) patterns in a given field-of-view (FOV) ensures accurate cross-correlation comparisons even when the image goes temporarily out of focus due to z-plane motion. The size of the frame in both the horizontal and vertical dimensions was kept constant by compensating with a black border. The video sequence was then rotated to align the vessel horizontally in preparation for diameter and lymphocyte velocity tracking.

Diameter Tracings

For quantifying lymphatic pump metrics an accurate diameter tracing algorithm was developed. In addition to the inherent low contrast, adipocytes accumulate around lymphatic vessels causing the vessel wall to become obscure and in most cases lose its sharp edge characteristics, thus common automatic edge detection algorithms did not prove to be accurate. This led us to use a 2D cross-correlation method based on previously published techniques[62] (**Figure 5A**). The user manually selects the two vessel walls in the first image of the sequence. The algorithm then draws a window around each of the vessel walls and sets the two windows as reference templates. To track the movement of these

windows, the template windows (solid green line) in a frame were correlated to search windows (dashed red line) in a subsequent frame and the maximum correlation coefficient calculated indicates the new position of the wall. The template window was centered on the current location of the vessel wall while the search window was larger and centered on the same coordinates in a subsequent frame. Typically the template window is 40 x 40 pixels while the search window is 80 x 80 pixels. The dimensions of these windows can be adjusted dynamically in the program in order to decrease computational time (by making the windows smaller) or to account for high contraction amplitudes in highly contractile vessels (by making the search windows larger). The diameter of the vessel was the distance separating the centers of the two windows and is tracked in every frame to give the diameter tracings over time.

Lymphocyte Velocity Tracking

While various demonstrated flow tracking systems are currently in use, each has its advantages and disadvantages. Laser speckle for example can measure speed but cannot differentiate the direction of flow[68] which is problematic given the oscillatory flow conditions in lymphatic vessels. Scanning laser image correlation (SLIC) might provide the ability to measure individual lymphocytes and distinguish particles flowing at various velocities in the field of view. While SLIC has been demonstrated in microfluidic channels and in zebrafish, it has yet to be adapted for use in larger animal models such as rats[69]. Therefore, a video based particle velocity algorithm was adapted from previous work[62,70] (**Figure 5B**) to track lymphocytes moving within the lumen of the vessel. The diameter tracings were used to set the spatial limit such that the template height was 80% of the average vessel diameter, the width was 50 pixels and centered at the midline of the vessel. This provided an adequate area to encompass several lymphocytes within the template window. In order to enhance the difference in correlation indices across the search area two consecutive frames were subtracted to remove static features in the vessel. This resulted in an apparent frame temporal separation (Δt) of 8ms instead of the expected 4ms resulting from an acquisition speed of 250 fps. Lymphocyte velocity was calculated as:

$$V^* = \frac{\Delta x}{\Delta t} \qquad (0.1)$$

The algorithm was verified using 15 µm polystyrene microspheres (Polysciences, Warrington, PA) attached to a glass slide. The size of the beads is comparable to lymphocyte diameters which range from 9-16 µm[71]. A custom .NET program was written to control a Zeiss AxioObserver Z1 motorized stage and move the slide at fixed velocities. High-speed video sequences were captured using the same imaging hardware and under the same magnification (100x) as our *in situ* experiment and compared to the known velocity values.

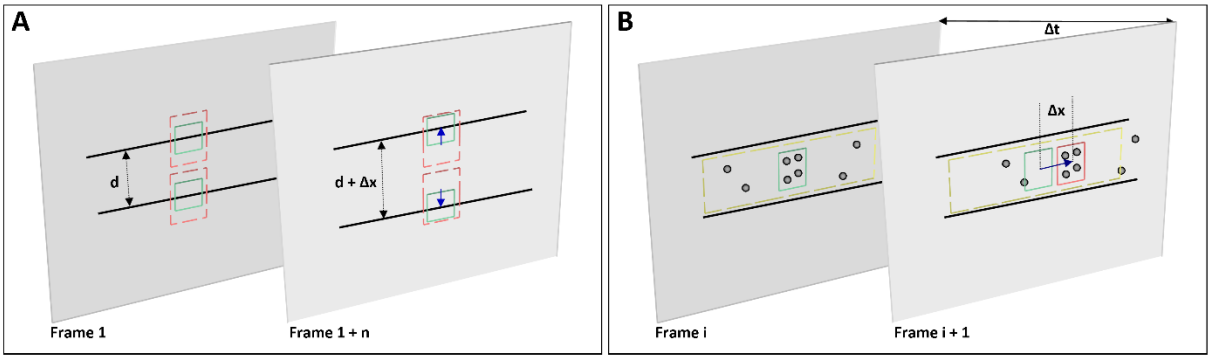

Figure 5: Post-acquisition image processing algorithms. *A) Diameter tracing algorithm. Green boxes (solid line) represent the template windows. Red boxes (dashed line) are the correlation search windows. The diameter (d) is the distance separating the centers of the two template windows as they are located across sequential frames. B) Lymphocyte velocity tracking algorithm. The green box (solid line) is the template window which is cross-correlated with the search window, yellow box (dashed line), the red box is the new template window location. Δt is the time separating two frames. The average velocity of lymphocytes is $V^*=\Delta x/\Delta t$.*

Fourier Analysis

An FFT amplitude spectrum was obtained for the diameter and velocity signals. Although the sampling rate was 250 fps, the resulting diameter and velocity signals are discontinuous with an inconsistent sampling period since the algorithm does not report back a diameter value when the image is highly out of focus. In addition, if there are too few lymphocytes to make an accurate velocity reading the velocity tracking algorithm will return a blank value. Thus before any processing was made, the signals were interpolated using linear interpolation then low pass filtered (Butterworth with cut-off of 5 Hz) to

remove high frequency measurement noise. The FFT amplitude spectrum was then obtained. All Fourier analysis was carried out with Mathworks MATLAB 2012a.

Quantifying Correlation Between Triglyceride Concentration and BODIPY C16 Fluorescence in Lymph

Animals

Male Sprague-Dawley (SD) rats weighing 250–350 g (Harlan, Indianapolis, IN) were individually housed in a temperature-controlled (21 ±1°C) vivarium on a 12-hr light, 12-hr dark cycle. Standard chow (LM-485 Mouse/Rat Sterilizable Diet, Harlan Laboratories) and water were provided *ad libitum* (except where noted). All animal procedures were performed in accordance with the University of Cincinnati Internal Animal Care and Use Committee and complied with the National Institutes of Health Guide for the Care and Use of Laboratory Animals.

Lymph fistula surgery and lymph collection

Rats were fasted for 24 hours prior to surgery, but retained free access to water. Rats were anesthetized with Isoflurane, then the superior mesenteric lymphatic duct was cannulated with polyvinyl chloride tubing (0.5 mm ID, 0.8 mm OD; Tyco Electronics, Castle Hill, Australia) according to the method of Bollman et al.[61] with slight modifications[72]. The lymph cannula was secured with cyanoacrylate glue (Krazy Glue, Columbus, OH). Intraduodenal cannulation was performed by inserting a silicone feeding tube (1.02 mm ID, 2.16 mm OD; VWR International, West Chester, PA) approximately 2 cm beyond the pylorus into the duodenum via a fundal incision of the stomach. The tube was secured by a purse-string ligature in the stomach and sealed by a drop of cyanoacrylate glue to prevent leakage. The lymph cannula and the intraduodenal feeding tube were exteriorized through the right flank. After surgery, the animals were placed in Bollman restraint cages and allowed to recover overnight; the animals were kept in a temperature-regulated chamber at 28 °C to prevent hypothermia and received a continuous intraduodenal infusion of 5% glucose-saline solution (145 mM NaCl, 4 mM KCl and 0.28 M glucose) at 3 mL/h for 6-7 hours. Rats then received continuous infusion of saline (0.15 M NaCl) at 3 mL/hr overnight prior to lipid infusion to compensate for fluid and electrolyte

loss due to lymphatic drainage. After overnight recovery, fasting lymph was collected on ice for 30 min prior to the start of the intraduodenal infusion. Rats received intraduodenal infusion of 3 mL of Liposyn III 20% concentration (Hospira) with 100 μg of BODIPY C_{16} (Life Technologies, Grand Island, NY) reconstituted in 20 μL of Dimethyl Sulfoxide (DMSO; Fisher Scientific, Pittsburgh, PA). Lymph was collected on ice for 30 min intervals for 4h min post-infusion. At the end of the lymph collection period rats were euthanized.

Measurement of triglyceride and BODIPY C16 in lymph

Lymphatic triglyceride concentrations were determined using a commercially available kit (Randox TG, Randox Laboratories Ltd., Crumlin, Northern Ireland, UK). Lymph samples were shipped on ice overnight from Cincinnati, OH to Atlanta, GA and BODIPY fluorescence was measured using a multimode fluorescence plate reader (DTX 880, Bechman Coulter, Indianapolis IN).

Quantitative Descriptors for Lymphatic Pump Function

From the diameter and velocity tracing the following metrics were calculated:

Constriction Wall Velocity (CWV). The velocity of the wall during vessel constriction for each contractile cycle averaged over the entire length of the video segment:

$$\frac{EDD - ESD}{\Delta t} \quad (0.2)$$

Where EDD is the End Diastolic Diameter, ESD is the End Systolic Diameter and *Δt* is the constriction time.

Dilation Wall Velocity (DWV). The velocity of the wall during vessel expansion for each contractile cycle averaged over the entire length of the video segment.

Volume Flow Rate (VFR). The lymphocyte velocity (V^*) calculated using the algorithm lies between the spatially averaged velocity ($\overline{V}$) and the maximum velocity (V_{Max}) assuming Poiseuille flow in a cylindrical tube. Since particles tend to locate themselves in the center

of a tube it can be assumed that V^* is closer to V_{Max}. Experimentally, a reasonable approximation was found to be $\overline{V} = \frac{2}{3}V^*$ [62].

Under these assumptions a volumetric flow rate is obtained:

$$VFR = \frac{\pi V^* d^2}{6} \qquad (0.3)$$

Where d is the diameter of the vessel when the lymphocyte velocity V^* is measured.

Stroke Volume (SV). Is defined as the total expected volume displaced during a contraction cycle of a lymphangion assuming an average lymphangion length and proper valve closure to prevent backflow:

$$SV = \pi\left[\left(\frac{EDD}{2}\right)^2 - \left(\frac{ESD}{2}\right)^2\right]L \qquad (0.4)$$

Where EDD is the End Diastolic Diameter, ESD is the End Systolic Diameter, *L* is the typical length of a rat lymphangion and is assumed to be 1 mm[73].

Ejection Fraction (EF). The fraction of end-diastolic volume ejected during a single phasic lymphatic contraction was calculated as:

$$EF = \frac{EDD^2 - ESD^2}{EDD^2} \qquad (0.5)$$

Where EDD is the End Diastolic Diameter, ESD is the End Systolic Diameter.

Fractional Pump Flow (FPF). An index of minute lymph pump flow[74] calculated as:

$$FPF = EF.CF.60 \qquad (0.6)$$

Where EF is the Ejection Fraction and CF is the Contraction Frequency measured in Hz.

Lymphatic Output (LO). Defined as the lymph flow rate due strictly to phasic contractions:

$$LO = SV.CF \quad (0.7)$$

Average and Max Wall Shear Stress (WSS). Assuming Poiseuille flow[70,75], WSS can be approximately calculated by:

$$WSS = \frac{4\mu V^*}{\frac{d}{2}} \quad (0.8)$$

Where μ is the dynamic viscosity of lymph and is on average equal to 1.5 centipoise (cP)[76], V^* is the lymphocyte velocity and d is the diameter of the vessel[70].

Effective Lipid Output (ELO). Representing the effective lipid output per minute and calculated as:

$$ELO = Intensity.VFR.60 \quad (0.9)$$

Where the intensity is the normalized BODIPY C_{16} fluorescence intensity and VFR is the Volume Flow Rate in µl/hr.

2.4. Results

Optical System Sensitivity to BODIPY

Our characterization experiments confirm the quantum yield of BODIPY exhibits a 7-fold increase when mixed with albumin (**Figure 6**). The increase in quantum yield quickly plateaus at an albumin concentration below that typically measured in lymph[77] suggesting fluctuations in fluorescence due to changes in albumin concentration are minimized. This increase in quantum yield is most often caused by alteration of the fluorophore de-excitation pathway, essentially increasing the probability of a radiative event[78]. Considering the limitations of this method, we calculate the minimum detectable concentration of BODIPY to be 24 ng/mL at 100 ms integration time (**Figure 7**) with the primary limiting factor being light leakage from the transmission halogen light source through the 580 nm LP filter with optical density (OD) of 5. A 100 ms integration time was used for all the experiments presented in this study.

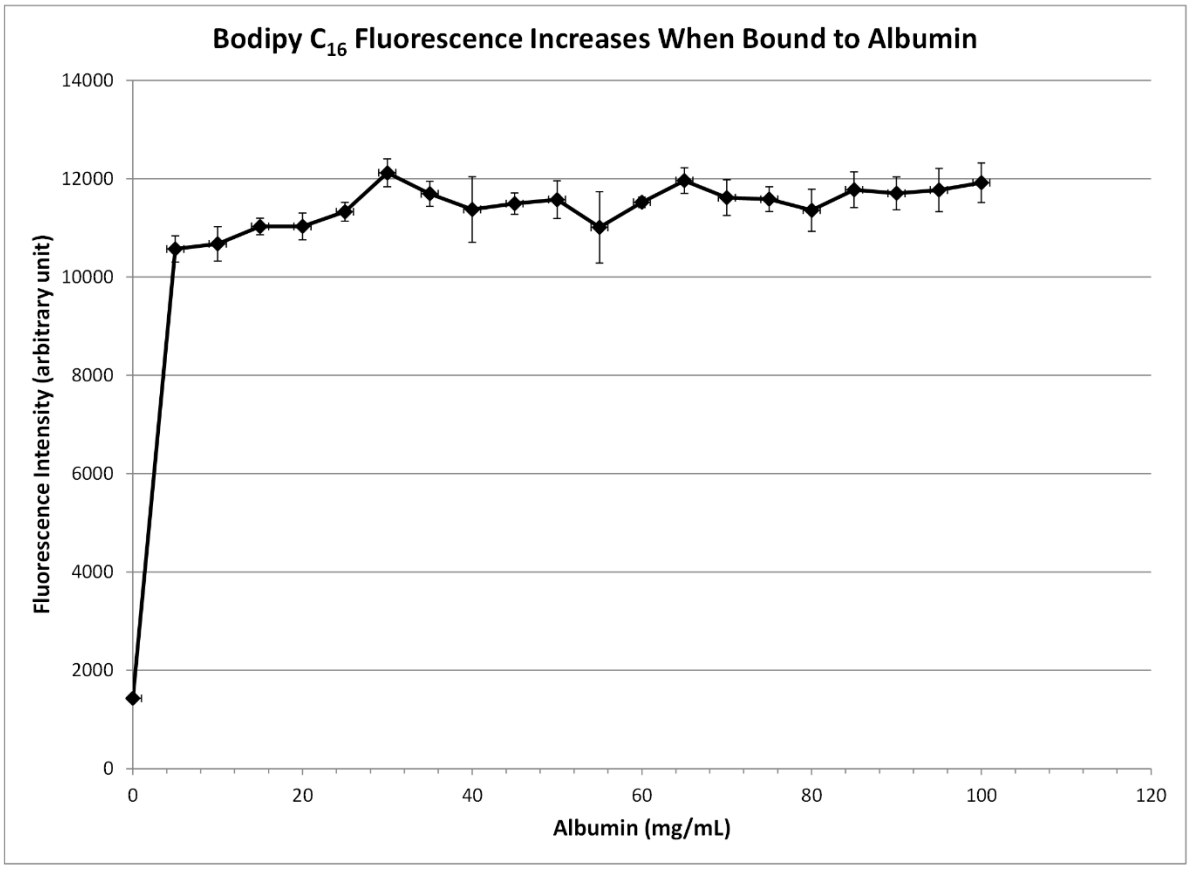

Figure 6: Fluorescence intensity in the presence of albumin. *BODIPY fluorescence intensity increased by approximately 7 fold when bound to albumin. Once bound, fluorescence is stable with the increase in albumin concentration. Error bars represent mean standard deviation (SD).*

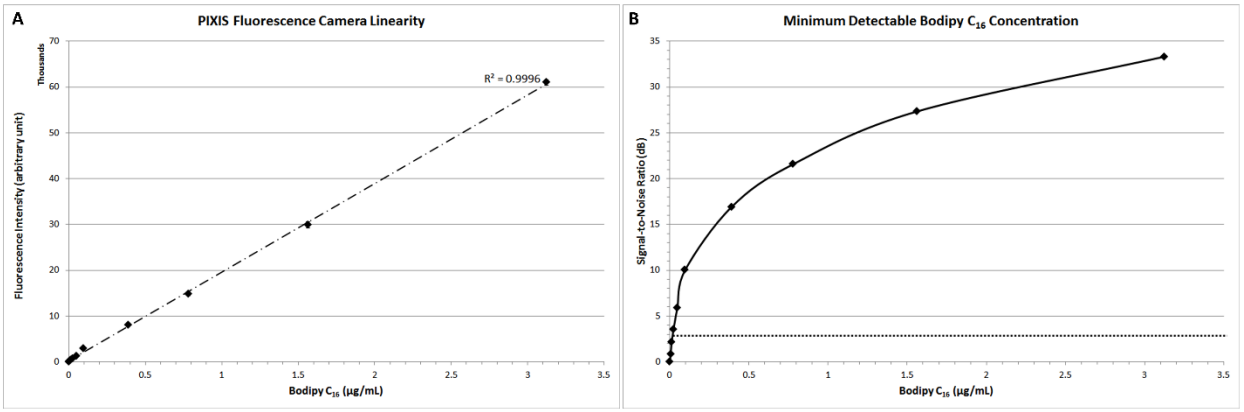

Figure 7: Performance characteristics of the fluorescence camera, the PIXIS. *A) A calibration curve shows the linearity of the PIXIS fluorescence camera and allows it to be used for quantitative fluorescence. B) Minimum detectable BODIPY concentration at 3dB signal-to-noise ratio (SNR) is 24 ng/mL in 10 mg/mL albumin solution.*

Correlation of BODIPY C_{16} Fluorescence and Triglyceride Concentration

In order to quantify the extent to which BODIPY C_{16} might be indicative of actual *in vivo* Triglyceride (TG) concentration we collected lymph from rats (n = 7) over a 4 hour period. Rats were infused with a lipid emulsion along with BODIPY C_{16}. It was found that the fluorescence trend correlates well with actual TG concentration (**Figure 8**) with a linear regression (R^2) value of approximately 0.83.

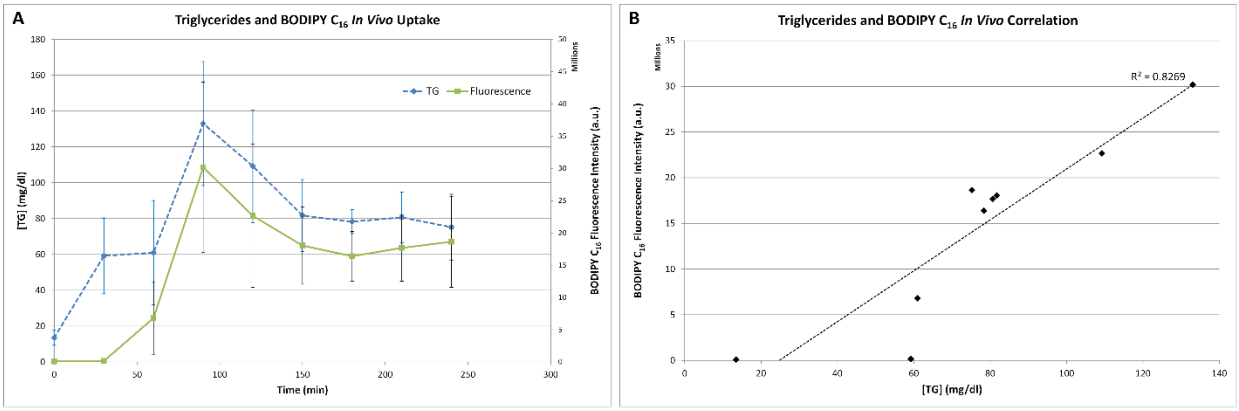

Figure 8: BODIPY C_{16} fluorescence correlates well with TG concentration. *A) TG concentration and BODIPY fluorescence in rat lymph. Lymph samples were collected at 30 minute intervals for 4 hours. TG concentration was quantified using a commercially available kit and fluorescence intensity values were obtained using a fluorescence plate reader. TG and fluorescence peak at around 2 hours after the start of intraduodenal lipid infusion. B) BODIPY fluorescence vs. TG concentration with a linear regression (R^2) value of almost 0.83. n = 7. Error bars represent mean standard deviation (SD).*

Image Processing Performance

Motion Compensation. The motion compensation algorithm significantly stabilized the high-speed video captured during intestinal peristalsis (**Figure 9**). A randomly chosen 60-second video segment was used to obtain performance characteristics. The standard deviation for the displacement of the original unstabilized video was 9 pixels with a maximum displacement of 45 pixels while that of the stabilized video was 0.4 and 3.5 pixels respectively (**Figure 9A**). The normalized correlation index of a window that was fixed in the FOV was calculated for the video segment. The standard deviation for the displacement of the original unstabilized video was 0.27 with a minimum correlation index of 0 (the contents of the window completely leave the area), while that of the stabilized video was 0.05 and 0.63 respectively (**Figure 9B**). The motion compensation algorithm developed can be easily applied to any video sequence.

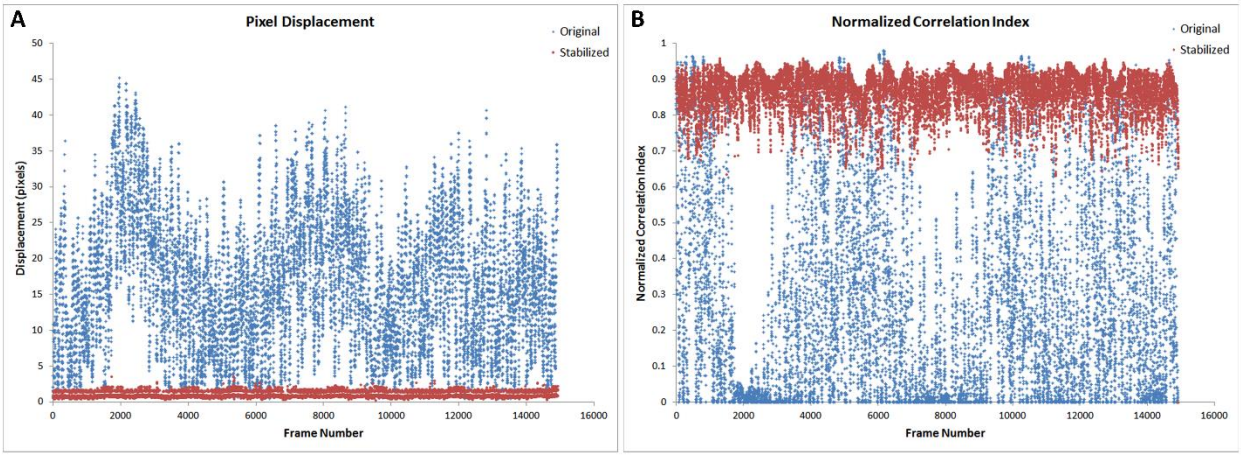

Figure 9: Motion compensation algorithm performance metrics. *A) Original vs. stabilized pixel displacement. The displacement of a template window was tracked as it moved in the field of view using 2D cross correlation. The standard deviation for the original unstabilized video was 9 pixels while that of the stabilized was 0.4 pixels. B) Original vs. stabilized normalized cross correlation values. The correlation index was tracked over time for a template window fixed in the field of view. The standard deviation of the normalized correlation index for the original unstabilized image was 0.28 while that of the stabilized was 0.05.*

Diameter Tracings. Manual measurements were carried out every one second of video by the user drawing a line connecting the vessel walls and measuring that distance. The manual measurements were then compared to the automated tracings (**Figure 10**). The average error rate between manual and algorithmic tracings was found to be around 3.3% and is likely a result of user subjectivity on the manual selection of where a vessel wall starts or ends. Diameter tracings obtained provide the basis for various parameters used to quantify lymphatic pump function (**Table 1**).

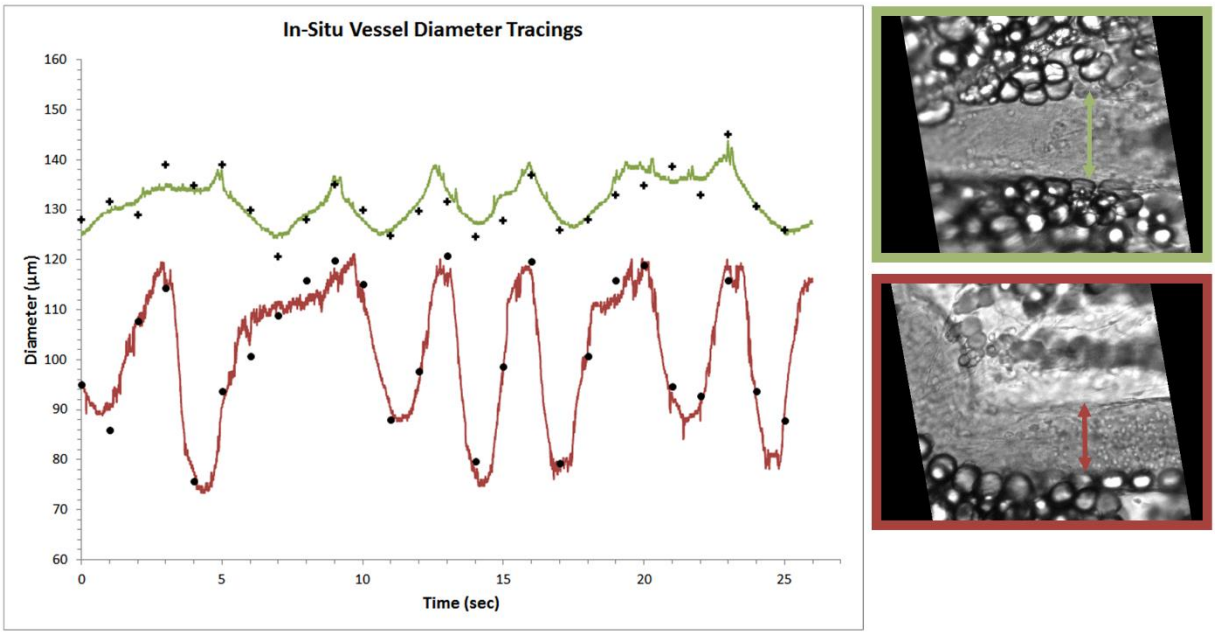

Figure 10: Verification of diameter tracing algorithm. *Two different vessels with varying morphology and sizes are displayed. Black markers indicate manual measurements where the user drew a line connecting the vessel walls and the distance was measured. Error rate between manual vs. algorithmic tracings was 3.3%.*

Table 1: Diameter related quantifiable parameters for characterizing BODIPY uptake and lymphatic pump function.

Time (min)	*BODIPY (Normalized a.u.)*	*AD (µm)*	*CF (Hz)*	*DC (µm)*	*EDD (µm)*	*ESD (µm)*	*CA (%)*	*CWV (µm/s)*	*DWV (µm/s)*
1	3.01	*144*	*0.26*	*11*	*150*	*139*	7	*7*	*5*
3	3.22	*138*	*0.24*	*13*	*146*	*133*	8	*8*	*6*
4	3.49	*137*	*0.22*	*19*	*147*	*129*	12	*9*	*11*
6	3.25	*141*	*0.24*	*13*	*148*	*133*	10	*8*	*9*
8	3.23	*133*	*0.16*	*17*	*138*	*123*	10	*9*	*8*
10	3.26	*148*	*0.16*	*11*	*153*	*142*	7	*7*	*6*
12	2.89	*148*	*0.18*	*8*	*151*	*142*	5	*5*	*4*
28	3.75	*153*	*0.24*	*5*	*156*	*151*	2	*5*	*3*
41	1.00	*144*	*0.12*	*7*	*147*	*140*	4	*3*	*4*
43	1.30	*142*	*0.24*	*4*	*145*	*140*	3	*2*	*3*
46	2.06	*144*	*0.26*	*6*	*147*	*141*	4	*3*	*5*
53	1.76	*143*	*0.18*	*13*	*150*	*138*	7	*3*	*8*
57	1.95	*128*	*0.16*	*10*	*136*	*125*	7	*3*	*7*
60	1.26	*157*	*0.24*	*3*	*159*	*156*	2	*1*	*3*

AD: Average Diameter, CF: Contraction Frequency, DC: Diameter Change, EDD: End-Diastolic Diameter, ESD: End-Systolic Diameter, CWV: Constriction Wall Velocity, DWV: Dilation Wall Velocity

Velocity Tracking. The algorithm has a 97% accuracy for measuring particle velocity in the range of lymphocyte velocities in the mesentery lymphatics reported in literature[70] (**Figure 11**). The motorized stage being used produced some inherently small jerky movements when moving at low speeds, this accounted for the somewhat jumpier than expected algorithm accuracy verification readings. Volume Flow Rates (VFR) and Wall Shear Stress (WSS) can be calculated from lymphocyte velocities as described previously[70] assuming Poiseuille flow in a cylindrical tube (

Table 2).

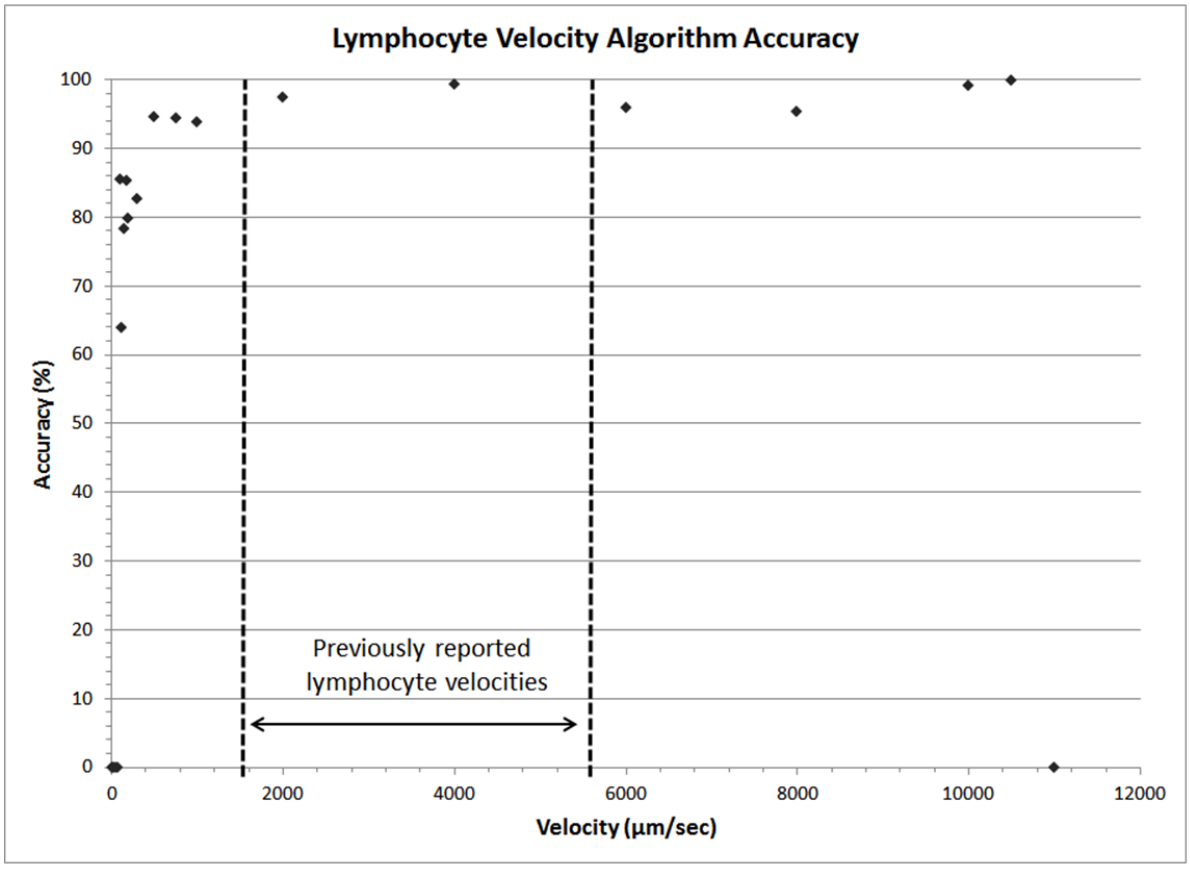

Figure 11: Accuracy of the lymphocyte velocity tracking algorithm. *Validation measurements were carried out by placing 15 µm beads on a slide and a motorized stage was programmed to move at certain velocities. Within the velocity range previously published the algorithm has close to a 97% accuracy rate in determining the velocity.*

Table 2: Lymphocyte velocity related quantifiable parameters for characterizing BODIPY uptake and lymphatic pump function

Time (min)	*BODIPY (Normalized a.u.)*	*MLV (µm/s)*	*Max. LV (µm/s)*	*Min. LV (µm/s)*	*VFR (µl/hr)*	*Avrg. WSS (dyn/cm²)*	*Max. WSS (dyn/cm²)*	*FPF (/min)*	*EF*	*SV (µL)*	*LO (µL/hr)*	*VFR/LO*	*ELO*
1	3.01	*43*	1928	-1512	*17*	0.06	2.00	2.14	0.14	0.02	22.77	1.10	0.84
3	3.22	*240*	2394	-1503	*87*	0.21	2.21	2.46	0.17	0.03	24.70	5.26	4.65
4	3.49	*289*	2111	-1578	*103*	0.24	1.84	3.12	0.24	0.04	32.09	4.79	5.96
6	3.25	*377*	2404	-1465	*143*	0.32	2.03	2.74	0.19	0.03	28.52	7.51	7.74
8	3.23	*392*	1933	-1378	*132*	0.35	1.89	1.98	0.21	0.03	17.98	11.03	7.11
10	3.26	*396*	1916	-1034	*164*	0.32	1.52	1.33	0.14	0.03	14.78	16.69	8.94
12	2.89	*527*	1845	-846	*219*	0.43	1.55	1.19	0.11	0.02	12.87	25.48	10.51
28	3.75	*504*	2024	-1407	*224*	0.40	1.68	0.78	0.05	0.01	8.95	37.61	14.03
41	1.00	*441*	2312	-1275	*173*	0.37	1.96	0.68	0.09	0.02	6.99	37.25	2.89
43	1.30	*326*	2665	-1736	*125*	0.27	2.35	0.93	0.06	0.01	9.19	20.38	2.71
46	2.06	*439*	2929	-1578	*174*	0.36	2.57	1.23	0.08	0.01	12.66	20.57	5.97
53	1.76	*435*	2670	-1557	*170*	0.35	2.21	1.65	0.15	0.03	17.52	14.53	4.97
57	1.95	*202*	2753	-1866	*63*	0.19	2.66	1.46	0.15	0.02	12.81	7.40	2.05
60	1.26	*399*	2559	-1456	*187*	0.30	2.06	0.67	0.05	0.01	8.04	34.84	3.91

MLV: Measured Lymphocyte Velocity, LV: Lymphocyte Velocity, VFR: Volume Flow Rate, WSS: Wall Shear Stress, FPF: Fractional Pump Flow, EF: Ejection Fraction, SV: Stroke Volume, LO: Lymphatic Output, ELO: Effective Lipid Output

2.5. Discussion

Alterative Imaging Systems

Miura et al. measured relative changes in lipid concentration in the mesentery lymph using graylevel ratios obtained by analyzing video images and were able to correlate them to an increase in lymphatic contraction frequency[22]. While some qualitative conclusions can be made, the sensitivity to changes in lipid concentration falls into a few discrete gray level values. The system is also limited by the fact that initial small changes in lipid uptake would not be detectable. However, using a back-illuminated 12-bit CCD along with BODIPY allows us to quantify changes in lipid concentrations as low as 24 ng/mL. With regards to quantifying lymphatic function, several systems are currently being used[74,79–82], however our set-up provides us with the capability of capturing an

unlimited duration of high-speed video allowing us to carry out measurements without any blind spots if the experimentalist wishes to do so. In addition, our motion compensation algorithm provides an integral tool for studies in the rat mesentery model, as unlike other systems, we do not need to fast our animal before an imaging experiment. This is also important since peristalsis is thought to provide an extrinsic mechanism for driving lymph flow[83], thus studies designed that intentionally minimize motion artifact by limiting peristalsis might actually be underestimating lymph flow rates in the mesentery. The system presented in this paper is both sensitive and able to provide us with various quantifiable data (**Table 1** and

Table 2) that comprehensively describe lymphatic pump function and lymph flow in the context of lipid uptake and transport.

Determining Intrinsic vs. Extrinsic Factors

Lymph flow is a consequence of various active (intrinsic) and passive (extrinsic) forces. The phasic contraction of lymphangions accounts for the dominant intrinsic pumping mechanism. Extrinsic factors include the driving force of lymph formation, influences of cardiac and arterial pulsations, contractions of skeletal muscles in proximity to the lymphatic vessels, central venous pressure fluctuations, gastrointestinal peristalsis, and respiration[9]. Because of this complexity the velocity peaks due to the actions of passive lymph pumps often are not synchronized with intrinsic contractile activity of lymphangions (**Figure 12**), flow profiles in lymphatic vessel are extremely variable and bidirectional[84]. By tracking both flow and contraction simultaneously during the absorptive process, we can quantity the significance of both the extrinsic and intrinsic pump on lymph flow. One such indicator for describing the dominant pumping is the Volume Flow Rate to Lymphatic Output ratio (VFR/LO). The VFR is the measured flow in the vessel obtained through lymphocyte tracking, while the LO is what is expected due to the intrinsic contractility of the lymphangion. In fasted rats this average ratio was 0.71[70]

while for the lipid fed rat shown here the average ratio was 11.64, indicating a dominance of extrinsic factors. This is most likely due to lymph formation serving as a dominant extrinsic factor[22], but more studies are warranted to determine the exact mechanism. Our system does, however, have the ability to distinguish between the expected flow rate due to vessel pumping and the actual flow rate, even in the context of lipid absorption and substantial intestinal peristalsis. In addition, obtaining a frequency spectrum of the underlying velocity and contraction frequencies (**Figure 13**) clearly shows that the fundamental frequencies of contraction and flow are independent, with flow having a higher fundamental frequency than contraction, further showing that extrinsic factors play a major role.

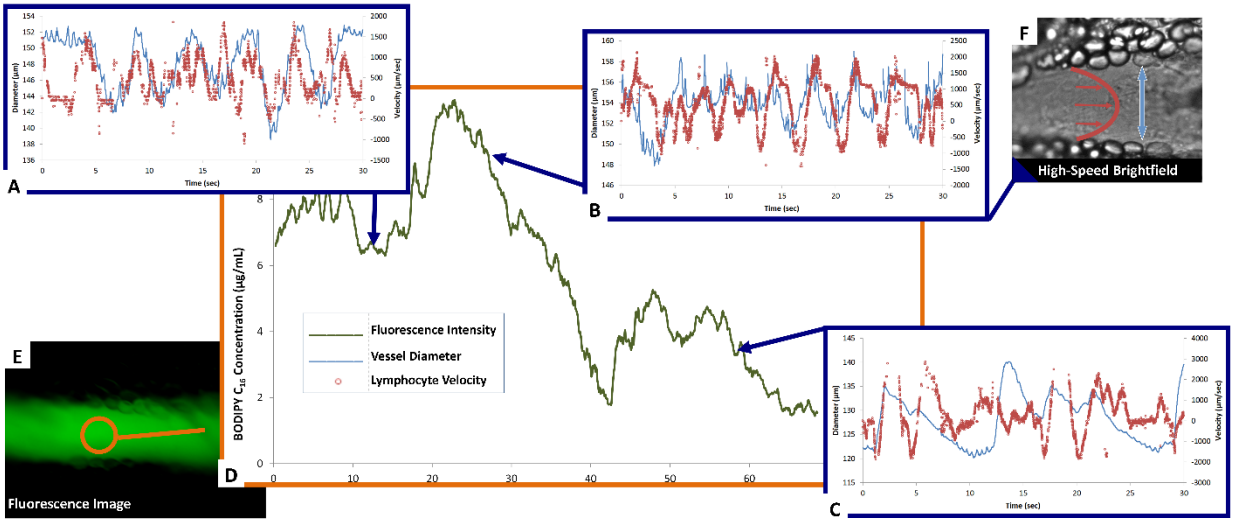

Figure 12: Correlating lipid uptake with lymphatic pump function. *A, B, C) Diameter tracings superimposed on velocity profiles for three time points at minutes 12, 28 and 57. C) Estimated BODIPY C_{16} concentration plot over a 68 minute period giving us relative lipid concentrations in the lymphatic vessel. E) Sample fluorescence image used for pixel intensity measurements. F) A single frame from a bright-field high-speed video segment used to extracting diameter and velocity data.*

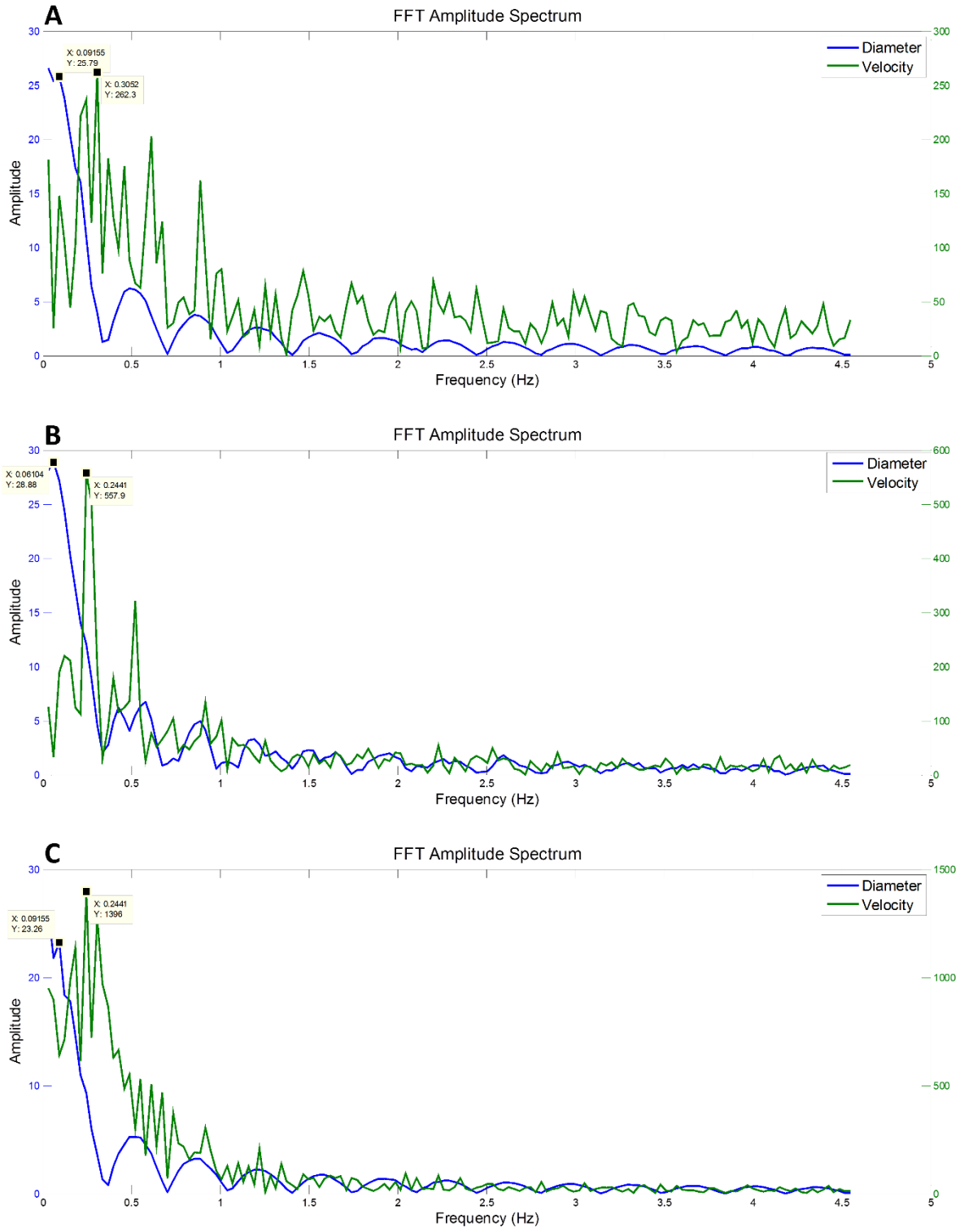

Figure 13: Fourier analysis of representative diameter and velocity tracings. *A) at 12 minutes (**Figure 12A**). B) at 28 minutes **Figure 12B**). C) at 57 minutes (**Figure 12C**). Fundamental frequencies for diameter and velocity tracings are different (see numerical labels), indicating that extrinsic factors might potentially be the dominant mechanism of transport as opposed to lymphatic contraction.*

Quantifying Intestinal Uptake

We have chosen BODIPY FL C_{16} (4,4-Difluoro-5,7-Dimethyl-4-Bora-3a,4a-Diaza-s-Indacene-3-Hexadecanoic Acid), a fluorescently labeled 16-carbon chain fatty acid, to quantify lipid uptake. BODIPY is an ideal choice due to having a high quantum yield and solvent photostability. The lymphatic transport characteristics of BODIPY C_{16} have been previously validated using a co-culture lacteal *in vitro* model[47,85] and have also been previously reported to be taken up into lymphatics *in vivo* after administration via gavage[24,47]. Because this fluorescent lipid analogue is a long-chain free fatty acid (LCFA), it is absorbed by the villi lining the small intestine and packaged along with the triglycerides present in the olive oil cocktail, to form fluorescent chylomicrons and correlates well with actual TG concentrations in lymph (**Figure 8**). BODIPY is exclusively taken up by lymphatics and is not detectable in the mesenteric blood circulation[47] and is metabolized as an 18-carbon fatty acid due to the presence of two extra carbons in the fluorophore[86]. Once the chylomicrons enter the mesenteric lymphatic, an increase in fluorescence intensity is observed (**Figure 12D**). While BODIPY was chosen for this particular application, any fluorophore in the green fluorescent protein (GFP) excitation/emission range can be used to quantify uptake by the mesentery lymphatics.

There has been growing interest in targeting lymphatics with orally delivered drugs or vaccines as such a route would avoid first-pass metabolism by the liver and could also provide access to mesenteric lymph nodes [87,88]. Fluorescently labeling these delivery systems would allow investigators to not only access lymphatic absorption of the drug, but would also provide insight into whether or not the delivery has unwanted consequences on lymphatic function, thus limiting its delivery to the systemic circulation. It could also provide insight into the mechanisms behind the enhancement of lymphatic uptake seen when drugs are delivered to a subject with elevated system levels of triglyceride rich lipoproteins[89]. Understanding the effects of metabolic differences between patients on oral drug absorption is essential for developing proper dosing strategies for these individuals.

Significance in Studying Disease

Malformations of mesentery lymphatics result in various clinical pathologies[23]. Protein-losing enteropathies, for example, are characterized by the progressive loss of protein from bowel due to elevated lymphatic pressure, lymphatic congestion and nonulcerative mucosal disease as well as inflammatory and ulcerative diseases. Primary intestinal lymphangiectasia (PIL) is one important form of protein-losing enteropathy. PIL is a disorder characterized by dilated intestinal lacteals which presumably cause lymph leakage into the small bowel lumen. Comparing VFR and BODIPY fluorescence in this diseased state to a healthy state will provide quantitative data to the extent of leakage, and potentially disease severity. A low-fat diet associated with medium-chain triglyceride supplementation is the cornerstone of PIL medical management. The absence of fat in the diet prevents chyle engorgement of the intestinal lymphatic vessels thereby preventing their rupture with its ensuing lymph loss. Medium-chain triglycerides are absorbed directly into the portal venous circulation and avoid lacteal overloading[25]. Using a long chain fluorescent fatty acid analogue such as BODIPY C_{16} can be used to better understand how the contribution of loading the lacteals contributes to the disease by investigating the active role that the collecting lymphatic vessel plays to clear the extra load. Even before PIL symptoms develop, patients have shown delayed transport of lipid from the intestine, suggesting that lymphatic lipid transport function is compromised at an early stage of the disease[23].

In addition, inflammatory bowl diseases (IBDs) such as Crohn's disease (CD), present themselves with several lymphatic abnormalities[14]. Lymphatic contractile activity was shown to be impaired in an isolated vessel model of gut inflammation, suggesting that lymphatic function might be compromised in inflammatory diseases such as CD[8]. While alleviating the lipid burden on lymphatics is clinically beneficial in many of these intestinal disorders, the exact mechanisms of lymphatic failure and the interplay between the lipid absorption process and lymphatic function is unclear. The imaging system described here has the capability to address many of these issues in a unique fashion. The parameters obtainable in **Table 1** and

Table 2, along with Fourier analysis and further signal processing analysis (**Figure 13**) will pave the way to understanding various disease states and quantitatively elucidating how mesentery lymphatic function changes in response to disease.

2.6. Conclusion

In an effort to better understand the role of lymphatics in lipid related diseases we developed a dual-channel *in situ* optical imaging system capable of quantifying lipid uptake and various parameters describing lymphatic pump function. We have demonstrated that the system has high sensitivity to low levels of an orally administered fluorescent fatty acid analogue and the ability to process the hundreds of thousands of images that are generated in a given experiment to quantify both flow and vessel contraction. The image processing techniques implemented allow all of this to be done even in the presence of the significant motion artifacts that occur as a consequence of intestinal peristalsis during fat absorption, providing a comprehensive tool to study lipid related diseases in the context of lymphatic transport.

III. ACUTE LIPID EXPOSURE DECREASES RAT MESENTERIC LYMPHATIC PUMP FUNCTION *IN VIVO*

3.1. Abstract

Dietary lipids are transported from the small intestine through collecting lymphatics that act as pumps generating strong contractions to move fluid against adverse pressure gradients. Recent studies have indicated that chronic pathologic lipid loads can adversely affect lymphatic function. However, the acute lymphatic pump response in the mesenteric lymphatics to a postprandial lipid meal has gone relatively unexplored. In this study, we used the rat mesenteric collecting vessel as an in vivo model along with a novel multimodal intravital microscopy technique to quantify the effect of lipoproteins on vessel pump function. Lipid load was continuously monitored using the intensity of a fluorescent fatty-acid analogue, BODIPY C_{16}, which we infused along with a fat emulsion through a duodenal cannula. The vessel contractile behavior was simultaneously quantified using high-speed bright-field video. We demonstrated for the first time that collecting lymphatic vessels functionally respond to an acute lipid load by reducing pump function. High lipid levels decreased contraction frequency by 86 % compared to a 16 % decrease in the saline infused control group (P = 0.019) and contraction amplitude decreased by 76 % compared to 16 % in the control group (P = 0.049). We also showed a strong tonic response by the vessel as indicated by a reduction in the end diastolic diameter of 43 % in the lipid group compared to 9 % in the control group (P = 0.006). These results provide the first evidence that high post-prandial lipid has an immediate negative effect on lymphatic pump function even in the acute setting.

3.2. Introduction

Nearly all dietary lipids enter the venous circulation via the lymphatics [90], which transport chylomicrons from the villi of the small intestine through the lymphatic vessel network to the thoracic duct where lymph is emptied into the blood via the left subclavian vein [8,16,91,92]. There is a rapid increase in triglyceride content in lymph after a lipid-rich meal [21] and how lymphatics respond to functionally handle this increased lipid load remains unclear. Lymph is drained through the intestinal lymphatics in large part through

the intrinsic pumping activity of the collecting vessels and one-way valves, which prevent backflow [10,70]. The collecting lymphatic vessels contain lymphatic smooth muscle cells which cause phasic and tonic contractions [4,5]. The collecting vessels' contractility, along with their unidirectional valves, result in a pumping mechanism that provides an active transport system to move lymph from peripheral tissue into venous circulation. It has been shown that this pumping mechanism can be modulated by a variety of substances including nitric oxide (NO) [93,94], histamine [95], prostaglandins [96,97] and hormones [98], many of which can be mechanically regulated to alter pump function in response to intraluminal pressure [99] and wall shear stress [11].

The lymphatic vasculature has recently been implicated in a variety of lipid related pathologies [8,100,101]. Several recent studies have shown strong correlations between obesity, high levels of circulating lipoproteins and lymphatic dysfunction. Diet-induced obesity in a mouse model showed impaired collecting lymphatic vessel function through decreased contraction frequency and enlargement of the vessels [102], decreased interstitial fluid flow, and decreased lymphatic transport to and between local lymph nodes [103]. Similar results have been shown in isolated mesenteric lymphatic vessels taken from a rat metabolic syndrome model where there was a decrease in contraction frequency and fractional pump flow [53]. In addition, vessels taken from a mouse model of type 2 diabetes showed compromised lymphatic barrier function and increased lymph leakage [104]. In humans, lymphatics present with a reduced ability to remove macromolecules from the interstitial space in obese subjects [105]. Obesity has also been associated with an increased risk in developing post-operative lymphedema [106,107]. On the other hand, an increase in lymphatic transport of lipids was observed in genetically diabetic obese rats, although this response was likely due to an increase in triglyceride synthesis as lymph flow remains unaltered in this diabetic model [108]. While lymphatic dysfunction seems to be directly correlated with obesity due in part to the chronic inflammatory environment associated with large adipose tissue beds [109], it remains unclear whether acute high levels of circulating lipoproteins in lymph could have a direct effect on lymphatic function as they do in the blood vasculature [110]. Chronic levels of

increased circulating lipoproteins, such as in hypercholesterolemia in adult ApoE$^{-/-}$ mice, resulted in a degeneration of lymphatic vessels that lead to decreased lymphatic drainage [57]. On the other hand, an older study conducted in rats, showed that mesenteric lymphatic vessels, in fact, increased their contractile frequency after being given an infusion of olive oil into the stomach [22]. However, in a recent clinical study, lymph lipid and lipoprotein concentrations in peripheral lymphatics were inversely correlated with lymph flow rate [111] but it was not clear whether that was due to decreased lymphatic pump function or other factors affecting lymph formation.

While obesity and high levels of lipoproteins are suggested to be a driving force for lymphatic dysfunction, several recent studies have shed light on a complementary relationship whereby lymphatic dysfunction can drive obesity and other lipid-related pathologies. For example lymphedema, a disease clinically characterized by irreversible swelling and compromised lymphatic function, was also associated with adipose tissue expansion [112,113] and chronic inflammation [109]. In addition, lymphatic vascular defects promoted by Prox-1 caused adult-onset obesity due to mesenteric lymph leakage [24]. Furthermore, impaired lymphatics were shown to exacerbate the atherosclerotic pathology using a mouse model of atherosclerosis crossed with different transgenic mouse strains with lymphatic insufficiency through unknown mechanisms affecting lipoprotein metabolism, increasing the levels of circulating lipid, and causing an increase in atherogenesis [114].

There has been a growing interest lately in the role that lymphatics play in the development and progression of lipid related diseases, and in quantitatively describing the evidently strong interplay between lipids and lymphatic vessel structural and functional behavior [8,100]. Although recent studies provide significant evidence that lymphatic function and the local lipid environment are highly influenced by one another, it is less clear how the main collecting lymphatics that drain the lipid-rich lymph of the intestine functionally respond to the rapid increase in lipid load that occurs in response to a lipid-rich meal. Given the regional heterogeneity of lymphatic pump performance [11], knowledge of the contractile response to lipid exposure in the lymphatic tissue bed that

encounters the largest potential lipid load will provide a relative framework for understanding the global lymphatic response to pathological lipid levels. While it is well established that circulating lipoproteins interact with the vascular endothelium to elicit endothelium mediated vascular responses that have been attributed to vascular disease [115,116], it is not known if such interactions also occur within the lymphatic endothelium and whether they cause measurable changes in the pump function of the vessel which could result in pathologically low lymph transport capacity. Previously, we reported the development of an intravital imaging system capable of simultaneously tracking lymphatic pump function and lipid load in vivo in the rat mesentery [117]. In this study we utilized this system to quantify the phasic and tonic contractile response of mesenteric prenodal lymphatics as they transitioned from a state of fasting to a post-prandial lipid load. We hypothesized that as lipid concentration in the mesenteric vessel increases post-prandially, the vessel will functionally respond to acute lipid exposure in a manner that is similar to pathological non-mesenteric vessels and exhibit a decrease in intrinsic lymphatic pump function.

3.3. Methods

Animal Model and Ethical Approval

Male Sprague-Dawley (SD) rats weighing 180-280 g (Charles River, Wilmington, MA) were chosen to facilitate comparative studies of lymphatic contractility to previous studies performed on the same strain. Both lipid (n = 8) and saline (n = 6) groups were provided with the same standard chow diet. Rats were fasted for 48 hours before each experiment while water was available ad libitum. One sugar cube was provided per rat the day after fasting began. All experiments were carried out under general Isoflurane anesthesia and animals were continuously monitored for signs of distress. Internal body temperature was maintained at 37-38 °C using a feedback controlled setup. Following the experimental procedure rats were sacrificed with a cut in the diaphragm while still under anesthesia. All animal procedures were performed in accordance with the Georgia Institute of Technology Internal Animal Care and Use Committee (IACUC) and complied with the National Institutes of Health Guide for the Care and Use of Laboratory Animals.

Surgical Protocol

After shaving a surgical area around the abdominal cavity, a 2 cm incision was made at the midline starting 1 cm below the Xiphoid process. The stomach was located and gently moved to the outside of the abdomen to expose the duodenum. A small incision was then made in the duodenum using a surgical scalpel and a small silicone tube was inserted into the incision and fixed to the outside of the duodenum using topical tissue adhesive (GLUture, Abbott, Worcester, MA). The stomach and duodenum were then placed back into the abdominal cavity. A single surgical suture was used to reduce the opening of the abdominal incision to around 1 cm. A segment of the small intestine distal to the duodenum was exteriorized and stabilized in a groove between two acrylic plates thus exposing the mesentery over an imaging window covered with a glass slide. An albumin physiological salt solution (APSS; in mM: 145.0 NaCl, 4.7 KCl, 2.0 $CaCl_2$, 1.2 $MgSO_4$, 1.2 NaH_2 PO4 , 5.0 glucose, 2.0 sodium pyruvate, 0.02 EDTA, 3.0 MOPS, and 1 g/L BSA) (all reagents from Sigma, St. Louis, MO) with pH adjusted to 7.4 ± 0.1 at 38 ˚C was temperature controlled to 36-39 ˚C and flowed at a rate of 21 mL/min to bathe the mesentery. A total of 1 L of APSS was recirculated for each rat throughout the experiment. The APSS bath recapitulated the oncotic extracellular environment found around the mesentery. The temperature of the rat was monitored and recorded with a rectal thermometer (Kent Scientific, Torrington, Connecticut). Internal body temperature was maintained at 37-38 °C using a feedback control mechanism by continuously monitoring the rat with a rectal probe and automatically adjusting a circulating water bath which flowed warmed water through tubing integrated within the custom designed surgical board. A lymphatic vessel was then located and placed over the imaging window. The vessel was given 10 minutes to equilibrate under the given conditions then imaging began.

A lipid solution containing Intralipid-20% fat emulsion (30% of total volume, Sigma), oleic acid (0.89 mg/mL, Sigma), saline (0.9% NaCl, 70% of total volume) and BODIPY C_{16} (40 µg/mL) (Life Technologies, Grand Island, NY) was infused through the duodenal cannula at a flow rate of 5 mL/hr. The infusion was stopped when the solution

reached the part of the small intestine that was being imaged (evident by the intestinal segment turning white and a noticeable distension). For the saline control group, saline was infused at the same flow rate as the lipid solution and infusion stopped when the intestine appeared relatively distended. The color of the intestine remained the same due to the fact that saline, unlike the lipid emulsion, was clear and not white. Image acquisition was carried out for an average of 90 minutes for both groups.

In Vivo Imaging and Processing of Mesenteric Lymphatic Vessel Function

A dual-channel optical imaging system and customized image processing algorithms were used to acquire both high-speed video and fluorescence intensity to simultaneously track lymphatic contraction and lymph lipid levels as described previously [117]. The high-speed video was captured at a frame rate of 250 fps and the fluorescence images at 0.2 fps (i.e. 1 frame every 5 s). Following acquisition, videos were digitally stabilized and vessel diameter tracings were obtained. Mean fluorescence intensity was also quantified post image stabilization.

Statistics

Eight rats were used for the lipid infused group and six for the saline controls. For each rat a single vessel was imaged. All data followed a Gaussian distribution. The Pearson correlation coefficient was used as a correlation index. A one-way ANOVA followed by correction for multiple comparisons using a Tukey test was used for all analysis. When comparing the percent changes between the saline and lipid groups multiple unpaired t-tests were run and the Holm-Sidak method was used to correct for multiple comparisons. For all tests, statistical significance was defined as $p \leq 0.05$ and graphically represented as 'ns' for $p > 0.05$, '*' for $p \leq 0.05$, '**' for $p \leq 0.01$ and '***' for $p \leq 0.001$. All statistical analyses were performed with Graphpad Prism v6 (GraphPad Software, La Jolla, CA).

3.4. Results

Imaging Vessel Contractile Behavior in Response to Lipid Load

By imaging the fluorescence emission of BODIPY C_{16} in a mesenteric vessel (**Figure 14A**), we were able to track the lipid uptake dynamics of a vessel after lipid arrival in the corresponding intestinal segment drained by that vessel (**Figure 14B**). Previously, we

demonstrated that the kinetics of BODIPY C_{16} into lymph closely follows that of triglyceride (TG), making it a suitable reporter for tracking lymph TG levels over time [117]. Lipid is first detected in the vessel within 15 minutes of appearing in the intestinal segment. This detection was followed by a rapid rise in lymph lipid level that peaked between 60 to 80 minutes post arrival of the lipid in the intestinal loop section being imaged. The high-speed bright-field video provided a clear view of the mesenteric vessel walls and was used to quantify diameter changes over time (**Figure 14C**), allowing us to extract and quantify various parameters of vessel pump function including contraction frequency (**Figure 14D**), contraction amplitude, average diameter and end diastolic diameter. Calculating the Pearson correlation coefficient between the relative lipid concentration over a 1-minute interval and the respective pump function parameter over that same time interval suggested that increases in lipid load resulted in a decrease in the contractile activity of the lymphatic vessel (correlations ranged between -0.27 to -0.30 (**Figure 14E**)). To analyze this in more detail, we utilized the BODIPY fluorescence intensity signal and segmented the experimental data into three discrete groups: 1) no lipid, 2) low lipid and 3) high lipid (See **Figure 14F**) and calculated vessel pump functional parameters for each of these loads.

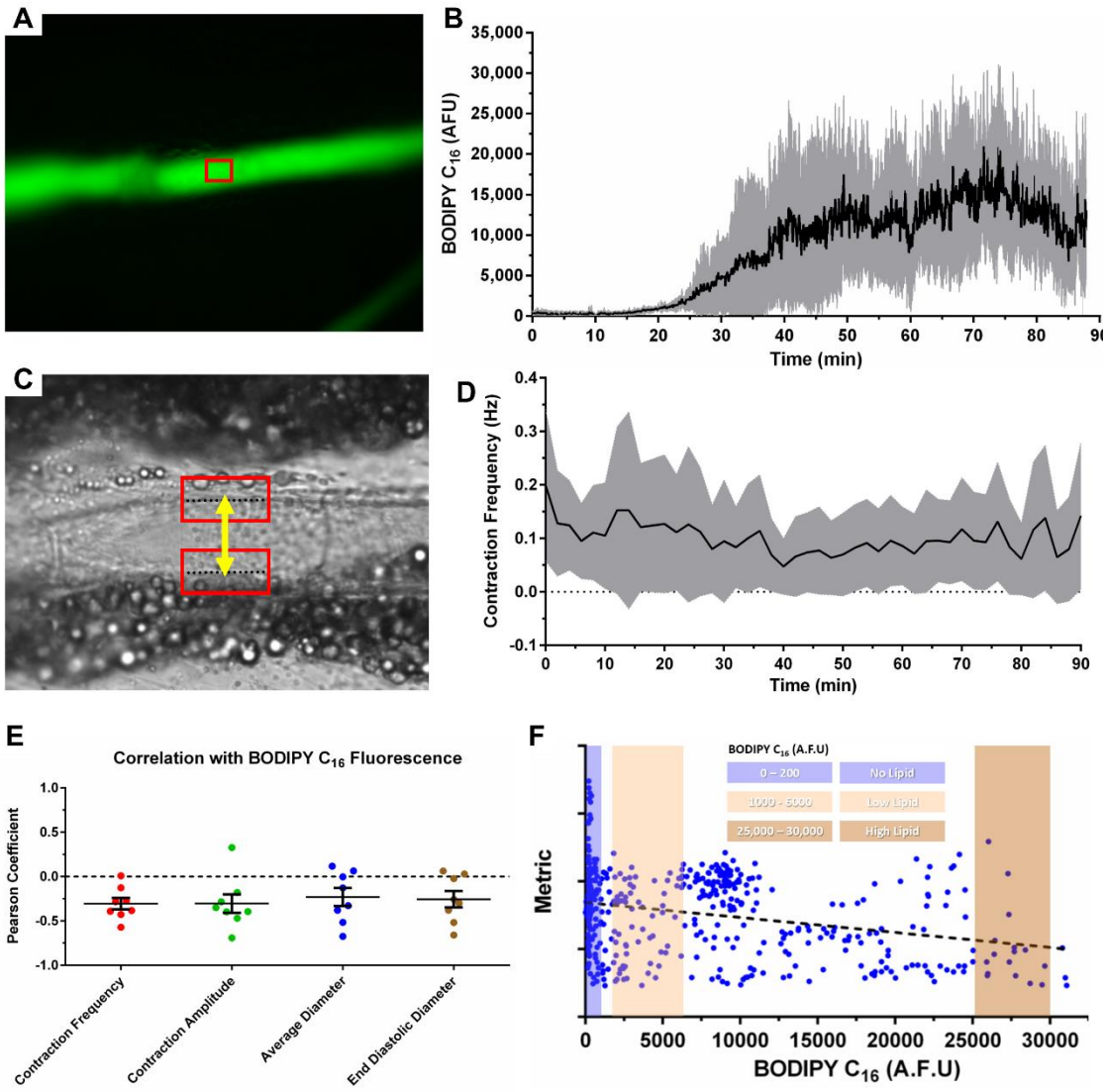

Figure 14: Simultaneous high-speed video and fluorescence acquisition provides the ability to assess the effect of a lipid load on lymphatic pump function. A) Fluorescent image of a rat mesenteric prenodal collecting lymphatic vessel. BODIPY C_{16} is used as a fluorescent indicator for triglyceride concentration within the vessel. The red window indicates a typical region in which fluorescence intensity was quantified following image stabilized to remove motion artifacts. **B)** BODIOPY C_{16} fluorescence intensity in the vessel over time following duodenal infusion of a fat emulsion along with BODIPY C_{16}. **C)** A single bright-field frame from a video sequence of 1-minute duration taken at 250 fps. The lymphatic vessel wall can be clearly seen and is typically surrounded by adipocytes. The red boxes represent a region of interest around each wall that was tracked using cross-correlation. The distance measurement provided diameter tracings which was used to quantify various functional parameters such as contraction frequency **(D)**. **E)** The Pearson correlation coefficient calculated for each metric as a function of BODIPY C_{16} fluorescence. Negative correlations were observed for all four metrics. **F)** A representative distribution for a certain metric (average diameter in this case) as a function of BODIPY fluorescence. Three discrete segments were chose to represent cases where there was no lipid in the vessel, low lipid and high lipid. n = 8, error bands and bars represent SD.

Contraction Frequency and Amplitude (Phasic Response) Decrease in Response to Lipid

Utilizing the obtained diameter tracings, we quantified two key parameters describing the phasic response of the lymphatic vessel; contraction frequency and contraction amplitude and showed that they both decrease with an increase in lipid load. Contraction frequency decreased as a function of BODIPY concentration (**Figure 15A**). The points where contraction frequency is zero represented video segments in which the vessel did not physically contract within the one minute video segment being quantified. The contraction amplitude exhibited a similar decrease (**Figure 15B**). As described earlier we further divided the lipid load into 1) no load, 2) low lipid and 3) high lipid. Contraction frequency was inversely related to lipid load and decreased from an average of 10.2 cpm when no lipid was present in the vessel to 1.8 cpm with a high lipid load ($P < 0.0001$), with several vessels exhibiting no contraction at that load. Even low lipid loads caused a significant decrease in contraction frequency compared to no lipid ($P = 0.0094$). There was no difference between the contraction frequency of vessels prior to lipid uptake compared to vessels draining from the intestines that were infused with saline ($P = 0.7564$) (**Figure 15C)**. Contraction amplitude averaged around 10 µm in saline infused animals and in lipid-infused animals when the levels of lipid were low, while in vessels with high lipid loads the contraction amplitude significantly decreased 5-fold to 2 µm ($P < 0.0001$). Taken together these results suggest a reduction in the phasic contractility of rat mesenteric lymphatics when exposed to high levels of lipid after a lipid-rich meal.

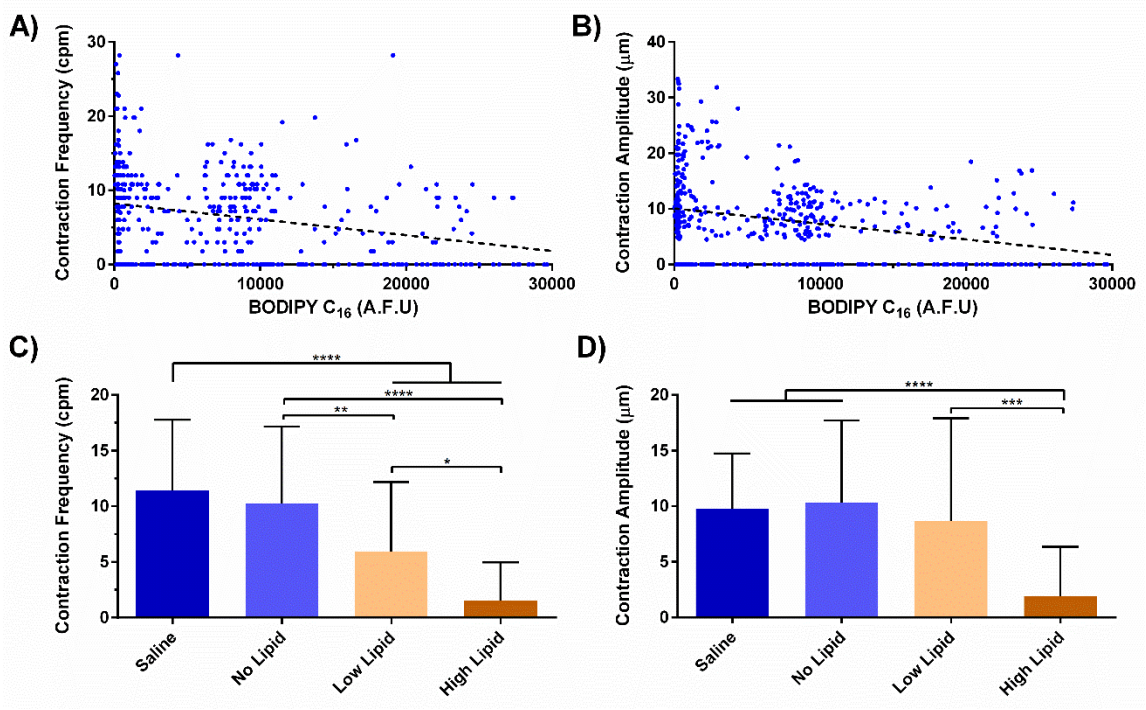

Figure 15: Mesenteric lymphatic vessels exhibit a decrease in their phasic response as evident by a decrease in both contraction frequency and amplitude. **A)** Contraction frequency decreased as a function of BODIPY C_{16} fluorescence. **B)** Contraction amplitude also decreased. **C)** Contraction frequency exhibited a lipid load dependent effect where it decreased from 10. cpm when no lipid was present to 1.8 cpm with the highest lipid load ($P < 0.0001$). **D)** Contraction amplitude also showed a similar dependency on lipid load where it decreased from 10 µm under no lipid load to 2 µm ($P = 0.6013$) under the high load. n = 8, error bars represent SD.

Average and End Diastolic Response (Tonic Response) also Decrease in Response to Lipid

In addition to a phasic contractile response, lymphatics are also known to exhibit a tonic contractile response with different underlying molecular mechanisms regulating the two [118]. To track changes in vessel tone over time, we quantified two parameters that are most reflective of the tonic response that has been reported in isolated, perfused lymphatic vessels: average diameter and end diastolic diameter. Both parameters decrease with an increase in lipid load, suggesting a measurable tonic response of the vessel to an infusion of lipid. Average diameter decreased as a function of BODIPY concentration (**Figure 16A**). The end diastolic diameter exhibited a similar decrease (**Figure 16B**). The average diameter decreased from 82 µm to around 50 µm under high lipid versus no lipid ($P < 0.0001$), and to a lower extent, 70 µm, under a low lipid load ($P = 0.0163$). There was no statistical difference between no lipid and the saline control group ($P = 0.4627$). Following a similar trend to the average diameter, the end diastolic diameter

decreased from 86 µm to 73 µm under a low lipid load (P = 0.0174) and to an average of 52 µm under high lipid (P < 0.0001). There was no difference in average end diastolic diameter between the no lipid and saline controls (P = 0.3722).

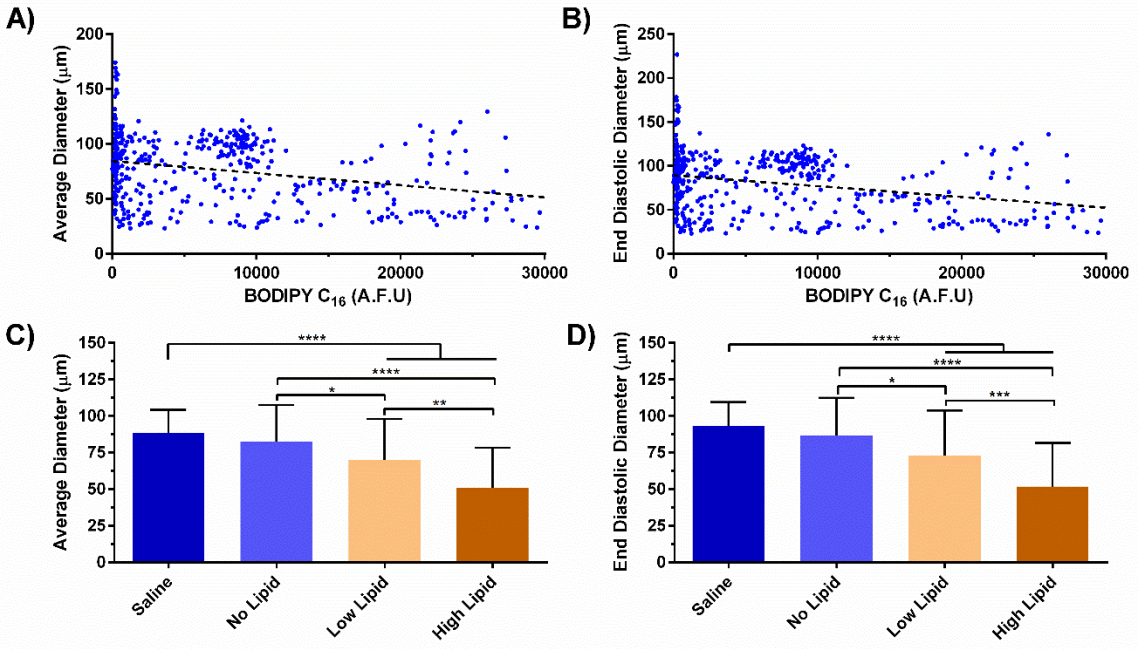

Figure 16: Mesenteric lymphatic vessels exhibit a decrease in their tonic response as evident by a decrease in both average and end diastolic diameters. **A)** Average diameter decreased as a function of BODIPY C_{16} fluorescence. **B)** End diastolic diameter also decreased. **C)** Average diameter exhibited a lipid load dependent effect where it decreased from 82 µm when no lipid was present to 50 µm with the highest lipid load (P < 0.0001). **D)** End diastolic diameter also showed a similar dependency on lipid load where it decreased from 86 µm under no load to 52 µm (P < 0.0001) under the high load. n = 8, error bars represent SD.

Lymphatics Maintain Constant Pump Function throughout Imaging Procedure

Since the rat is maintained under anesthesia and the mesenteric vessels are exposed to imaging for over two hours, there was some concern that loss of contractile activity could occur over time and thus result in the reduction of pump function that was observed during periods of high lipid. In addition to this concern the mesenteric bed becomes stretched due to the significant distention of the intestinal wall as the bolus of food arrives. To account for these effects, we designated a group of control rats which underwent the same procedure except they were given an equal volume infusion of saline instead of lipid. The contraction frequency and amplitude showed a very modest decrease over time in the saline control rats (**Figure 17A-B**), but comparing the phasic response metrics at the same interval in time when we typically see the high lipid load in the lipid

infused rats showed that the percentage decrease for both metrics was significantly higher in the lipid group. Specifically, there was an 86 % decrease in contraction frequency compared to 16 % in controls (P = 0.019) and 76 % decrease in contraction amplitude compared to 16 % in controls (P = 0.049) (**Figure 17E**). The average and end diastolic diameters also showed a slight decrease in the saline control rats (**Figure 17C-D**) but comparing the tonic response metrics at the same interval in time when we typically see the high lipid load in the lipid infused rats showed that the percentage decrease for both metrics was significantly higher in the lipid group. Specifically, there was a 41 % decrease in average diameter compared to 8 % in controls (P = 0.005) and a 43 % decrease in end diastolic diameter compared to 9 % in controls (P = 0.006) (**Figure 17E**). All this suggests that the phasic contractility of the mesenteric lymphatic vessel as well as the tonic response significantly decreased in the presence of intraluminal lipid.

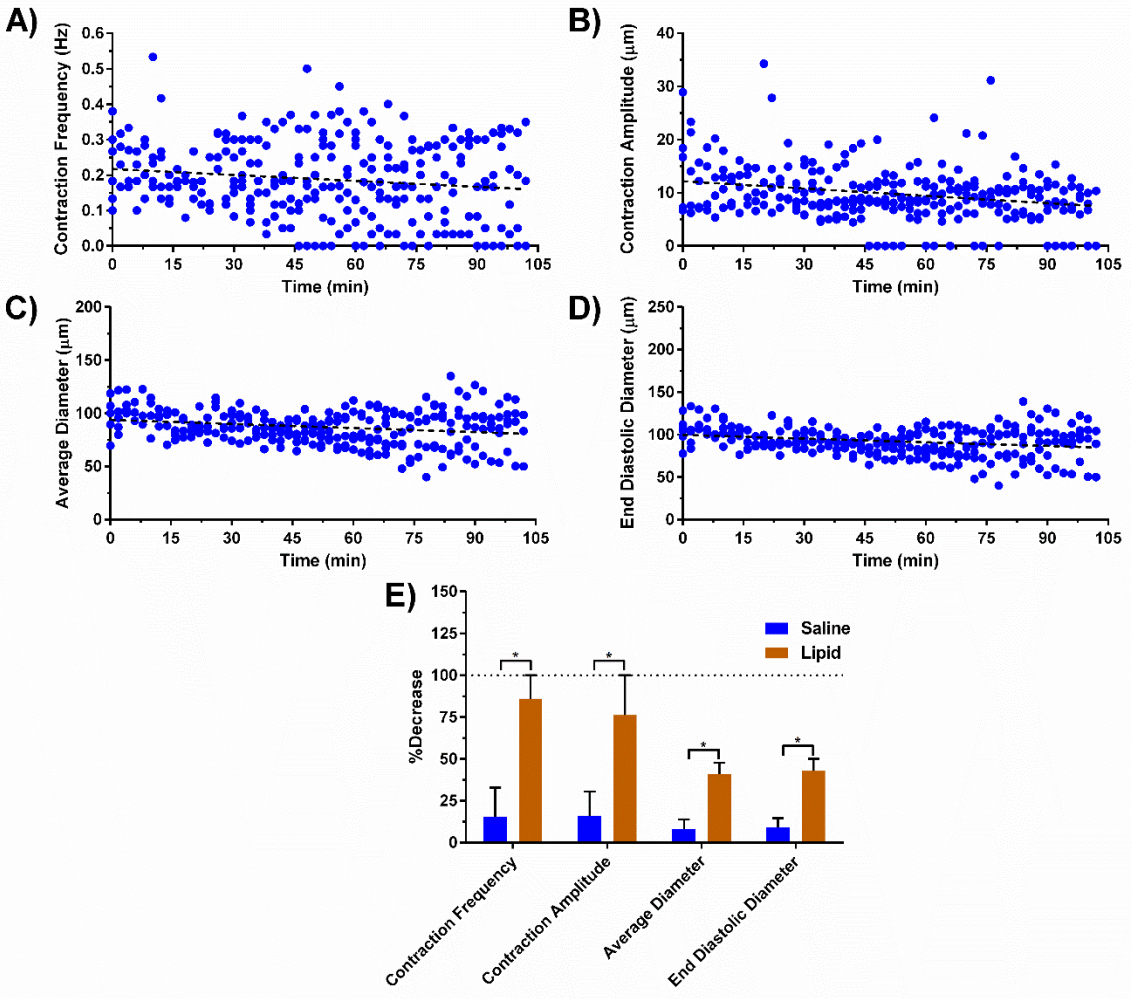

Figure 17: Rats infused with saline only show little decrease in phasic and tonic response. Control rats were infused with saline only instead of the lipid emulsion. Contraction frequency **(A)**, contraction amplitude **(B)**, average diameter **(C)** and end diastolic diameter **(D)** showed minimal decrease over time. E) Contraction frequency showed a much higher percentage decrease in the lipid infused rats than in the controls (86 % vs 16 %, P = 0.019), so did contraction amplitude (76 % vs 16 %, P = 0.049), average diameter (41 % vs 8 %, P = 0.005) and end diastolic diameter (43 % vs 9 %, P = 0.006). n = 6, error bars represent SEM.

3.5. Discussion

While lipid uptake by lymphatics has been extensively studied and reported in literature, most of these studies were carried out by collecting lymph via the mesenteric lymphatic duct. Since our technique allows us to determine when lipid first appears in the intestinal region drained by a given lymphatic, we were able to determine the total time for lipid absorption, packaging of chylomicrons, release into the villi and uptake into the lacteal [119]. Lipid can first be detected in the mesenteric collecting vessel within 10-20 minutes and reaches a maximum concentration around 60-80 minutes. The time-frame previously reported for chylomicrons to first appear in the mesenteric lymphatic duct was

reported to be at around 14-22 minutes and to peak around 2-3 hours [21] (**Figure 18**). Previous studies used fluorescence based TG assays instead of quantifying chylomicron-incorporated fluorescent fatty acids. The assays typically utilize the hydrolysis of TG by lipase to produce free fatty acids and glycerol which is then measured by an enzymatic reaction quantified using a fluorescence colorimetric readout [120]. Despite the fact that TG assays might possibly be more sensitive and are a more direct measurement of TG, they cannot be used for real-time intraluminal TG measurements. We have previously shown that lymph fluorescence of BODIPY C_{16} correlates quite strongly with total lymph TG [117], thus giving us a real-time measurement of the lipid content in the vessel and allowing us to quantify the instantaneous vessel response upon lipid exposure.

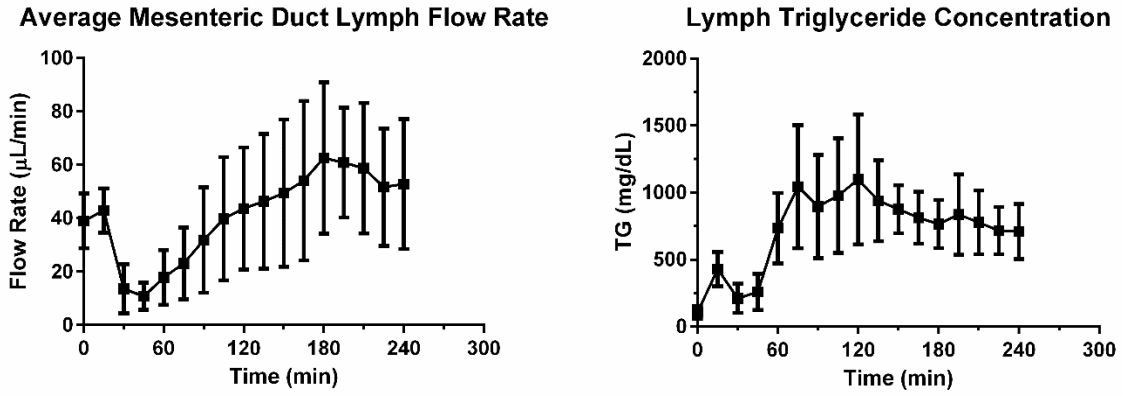

Figure 18: Mesenteric duct lymph flow rate and triglyceride concentration increases after lipid infusion. A) Average flow rate in a rat mesenteric duct as measured using lymph collected from a cannula. Flow rate increases beginning at around 1 hour after the start of duodenal lipid infusion and plateaus at 3 hours. **B)** Triglyceride concentration increases with time and plateaus at around 2 hours. TG concentration was measured using a TG fluorescence assay. n = 7, error bars represent SD.

The vessel responded to the acute exposure to lipid by reducing the phasic contraction frequency and amplitude and through reducing the overall average vessel diameter and the end diastolic diameter. The reduction in phasic contractility appears to agree with similar results reported in mesenteric collecting lymphatic vessels isolated from a rat metabolic syndrome model [53] and in vivo in obese mice [102] but is in disagreement with one in vivo study in which rats infused with olive oil demonstrated a significant increase in collecting lymphatic contraction frequency [22]. This study was limited in its quantitative description of vessel luminal lipid content and thus it is difficult to compare their results with those presented here. It is worth noting that the fatty acid

content for both Intralipid and olive oil is similar (**Table 3**) except that Intralipid has a higher level of the polyunsaturated omega-6 linoleic acid than olive oil whereas olive oil is richer in the monounsaturated omega-9 oleic acid but there is no strong support that these differences would account for the different lymphatic vessel response [121]. The decrease in phasic contractility presented in our study however could be attributable to a variety of factors including oxidative stress due to lipoprotein oxidation, through induced nitric oxide (iNOS) mediated NO [122] or histamine [95] both of which are released by activated lymph resident immune cells that double in density after a lipid meal [22]. However, these factors would not explain the strong tonic response we observed in the lymphatics in response to high lipid, as both NO and histamine are known to increase the diastolic diameter. Lymphatic vessel tone is usually defined as being the percent difference between the passive diameter of the vessel under Ca^{2+}-free conditions at a given pressure and the end diastolic diameter with the presences of Ca^{2+} at the same pressure [53]. While we are unable to directly quantify vessel tone in this manner in vivo, as we have no control over the pressure or the Ca^{2+} concentration, we interpret a reduction in the end diastolic diameter as indicative of a tonic response. A variety of factors have been previously shown to cause vessel constriction in lymphatics, these include elevated downstream pressures [98], increased local vessel pressure [123], inhibition of VEGFR-3 [79], arachidonic acid metabolites which can be secreted by lymphatic vessels [124] as well as certain concentrations of histamine [125].

Table 3: Fatty acid components of olive oil and the commercial lipid emulsion, Intralipid. Fatty acid content is similar in both with Intralipid having more linoleic acid as opposed to olive oil which has a higher percentage of oleic acid.

	Intralipid	***Olive Oil***
Oleic acid (C18:1)	19-30 %	55-83 %
Linoleic acid (C18:2)	44-62 %	3.5-21 %
Palmitic acid (C16:0)	7-14 %	7.5-20 %
Stearic acid (C18:0)	1.4-5.5 %	0.5-5 %
Linolenic acid (C18:3)	4-11 %	0-1.5 %

Quantifying the acute functional response of mesenteric lymphatic vessels during lipid absorption of a high fat meal is crucial in understanding numerous clinical

pathologies where lipids have been implicated in malformations and dysfunctional lymphatic vessels [23]. For example, in some protein-losing enteropathies such as primary intestinal lymphangiectasia (PIL), the blind ended initial lymphatics in the intestinal villi are significantly dilated and cause lymph leakage into the intestinal lumen. A standard procedure in managing the disease is to prescribe a low-fat diet supplemented with medium (MCT) and short chain triglycerides (SCT) which minimizes the lipid load of the lymphatics since they primarily absorb long chain triglycerides (LCT) [25]. The absence of high lipid load prevents the rupture of lacteals and hence reduced lymph leakage. Using a long chain fluorescent fatty acid analogue such as BODIPY C_{16} can be used to better understand how downstream impairment of collecting lymphatic vessel lipid clearance might contribute to the observed overloading of the lacteals. Even before PIL symptoms develop, patients have shown delayed transport of lipid from the intestine, suggesting that lymphatic lipid transport function is compromised at an early stage of the disease[23]. In addition, lymphatic phasic contraction was shown to be hindered in an isolated vessel model of gut inflammation, suggesting that lymphatic function might be compromised in inflammatory bowel diseases such as Crohn's disease [14]. While alleviating the lipid burden on lymphatics is clinically beneficial in many of these intestinal disorders, the exact mechanisms of lymphatic failure and the interplay between the lipid absorption process and lymphatic function in these disease states is still unclear. The results presented here suggest that high concentrations of lipid can directly reduce lymphatic pump function, which would likely exacerbate the condition in a disease physiology where there is already substantial inflammation.

Obesity is one of the few established factors that predisposes patients to developing secondary lymphedema [107,109]. Additionally, several recent studies have demonstrated impaired function of the lymphatics in obesity [102,103,107,109]. LCTs constitute around 90 % of the fat content in a typical Western diet so if lipid content is adversely affecting lymphatic pump function, it is likely to increase the chances of lymphedema since patients who have a reduced lymphatic functional capacity at baseline are at higher risk for developing lymphedema [103]. It has also been shown that reducing the amount of

LCT in diets of lymphedema patients and replacing them with MCT reduced peripheral edema [126]. This edema reduction could be due to reduced formation of lymph, and hence less leakage in the affected limb, or to the fact that lower lipid content in lymph possibly restores lymphatic vessels to their normal functional capacity.

While our in vivo animal model along with the developed imaging tools provide a good platform to study the effect of lipids on lymphatic pump response, there were several limitations that might limit our understanding of the physiological post-prandial response that we might typically see. The procedure is highly invasive, requires anesthetic, and alters the vessel's mechanical environment. Care was taken to minimize these effects by including control rats that underwent all of the same surgical and mechanical perturbations, but received a bolus of saline in the intestine rather than lipid. In addition to this, while we would have liked to measure flow rates in the vessel utilizing our previously published approach [62,117] we were only able to accomplish this in the control rats (**Figure 19**). These measurements were not possible in the lipid infused rats due to the low contrast between lymphocytes and the surrounding lymph. This low contrast was most likely due to the dramatic increase in chylomicron concentration which acted as light scattering agents (note, lymph turns milky white after a high fat meal) [127]. Since we cannot measure lymphatic flow in the local vessel, it makes it difficult to ascertain whether alterations in fluid shear stress during lipid absorption might be partially responsible for the pump function response. However, this seems unlikely, as there are no reports of shear stress in lymphatics decreasing the contractile frequency and causing a reduction in the end diastolic diameter. Typically, elevated fluid shear reduces contraction frequency and dilates the vessel [7,95,128].

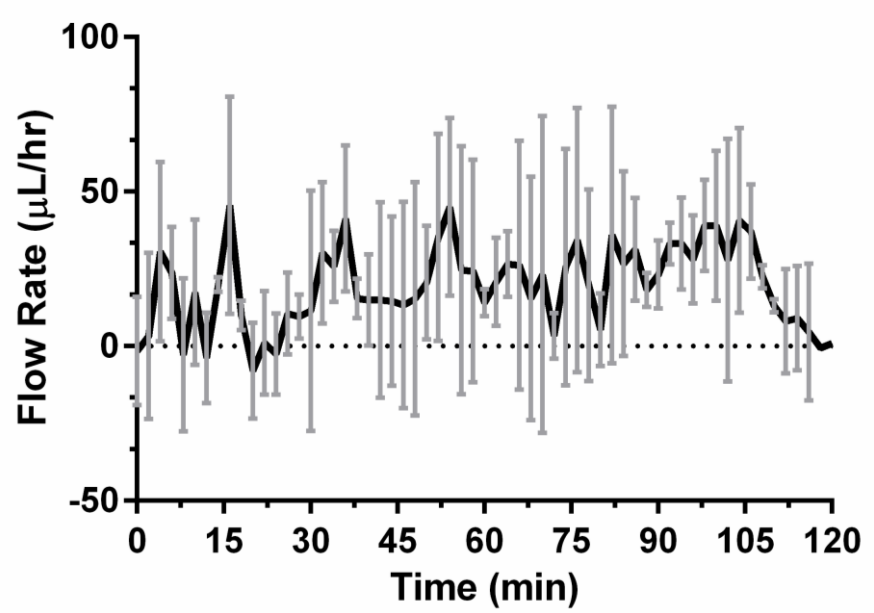

Figure 19: Flow rate in control rats can be measured successfully. Flow rate for the control rats can be measured due to the fact that there is large inherent contrast between lymphocytes and the surrounding lymph. Similar measurements cannot be made however on the lipid infused rats. Flow rate in control rats (infused with saline) seems to not change upon infusion. n = 5, error bars represent SD.

3.6. Conclusion

In conclusion, we report here for the first time the kinetics of lipid uptake from the intestine to the mesenteric collecting lymphatic vessel immediately draining the region in the small intestine where the lipid is being absorbed. We go on to show using a novel multimodal intravital microscopy approach, that in the context of a lipid meal, high lipid loads within a lymphatic vessel alter lymphatic function by reducing phasic contractions and causing an overall tonic constriction in the vessel. In addition, the developed experimental model will allow future researchers to further investigate the detailed mechanisms underlying lipid uptake and transport in both healthy and disease states and can be easily adaptable to other small animal models.

IV. POST-PRANDIAL VISCOSITY OF LYMPH FOLLOWING A HIGH-FAT MEAL

4.1. Abstract

Lipid content of mesenteric lymph increases several folds during lipid absorption after a high-fat meal. It has long been suggested that this also translates into a substantial increase in lymph viscosity and hence an increase in shear stress that the mesenteric vessel is exposed to. Here, we sought to measure lymph viscosity in a rat for both the fasting state and the time-dependent changes following a high-fat meal. Viscosity measurements were conducted using a microrheology technique utilizing the Brownian motion of fluorescent carboxylate-modified polystyrene particles embedded in lymph samples collected from rats at 15 minute intervals for 4 hours. The mean fasting lymph viscosity was found to be 0.70 cP and 0.82 cP when an anti-coagulant was added to the samples. After a high-fat meal the viscosity ranged from 0.70 to 0.78 cP peaking at 1 hour and 0.82 to 1.04 cP in the presence of an anti-coagulant. The average lymph triglyceride (TG) concentration ranged from 107 mg/dL at the start of lymph collection to 709 mg/dL at 4 hours with a peak mean of 1098 mg/dL occurring at 2 hours. While TG and viscosity are positively correlated, other unknown factors present in lymph also appear to have an effect on lymph viscosity, reflecting the dynamic and variable nature of lymph composition. The viscosity of lymph during postprandial lipid absorption and its relationship to lymph TG have been reported for the first time, and suggest that changes in lymph viscosity have a small but important effect on the fluid sheer stress imposed on the lymphatic vessel during lipid absorption.

4.2. Introduction

Lymphatic networks are found in almost all vascularized tissues, excluding the bone marrow and the nervous system [129,130], and function to maintain fluid homeostasis within the interstitium of these organs [127,131], provide a conduit for immune cell trafficking, and transport dietary lipids from the intestinal tract to venous circulation [8,21]. Collecting lymphatic vessels transport lymph through coordinated contractions of individual vessel segments known as lymphangions [132]. These contractions constitute

what is known as the intrinsic lymphatic pump. Lymph flow within these vessels continuously exposes the lymphatic endothelium to wall shear stress (WSS) [70], which has been shown to play a primary role in vessel development and function. Low WSS levels are required for both the formation of structurally sound lymphatic vessels [133–135] and maintenance of lymphatic endothelial cell identity [136]. WSS also actively modulates the pumping response of the vessel, and hence transport, through the differential release of vasoactive substances, such as nitric oxide (NO) [137–139]. This response seems to vary with the physiological region of the vessels whereby the thoracic duct has been shown to be the most sensitive to WSS, drastically reducing its pumping when exposed to flow and thus lowering its resistance to flow and behaving as a passive conduit. Mesenteric vessels, on the other hand, are less sensitive to WSS, maintaining their function as a pump even in the presence of fluid flow [7,11]. The influence of WSS and its effects on the lymphatic vasculature is an emerging field of study.

Lymph viscosity, along with flow rate and vessel diameter, is an important contributing factor to WSS. One of the most dramatic changes in lymph content occurs in the mesenteric lymphatic vessels which transport absorbed lipids from the small intestine to the mesenteric lymphatic duct. These changes are especially dramatic after a high-fat meal when lipid concentration dramatically increases compared to the fasting state. Ingested lipids are broken down by digestive enzymes and absorbed into the epithelial cells (enterocytes) lining the inner lumen of the small intestine. Within the enterocytes, the triglycerides are combined with cholesterol and phospholipids, and then packaged into lipoproteins called chylomicrons. The chylomicrons are then absorbed into the lymphatics through the lacteals, lymphatic capillaries located within the villi of the small intestine [8,16–19,140]. While there are currently both methods to measure the changes in lymph flow rates and vessel diameter [70,117] and to impose arbitrary lymphatic flow waveforms *in vitro* [141], it has been very difficult to estimate the contribution of viscosity changes to WSS resulting from the increase in lymphatic lipid concentration. Most studies estimating WSS in lymphatics refer to a 1917 study to provide an estimate for lymph viscosity, where Burton-Opitz et al. measured the viscosity of dog lymph after feeding a

high-fat meal [76]. They accomplished this by collecting lymph from the thoracic duct and measuring the time required for the passage of lymph through a capillary tube at a given pressure. Unfortunately, this method cannot be used with small lymph volumes, preventing measurements in smaller animal models, regional measurements from various lymph formation sources, and temporal measurements over short drainage intervals. More recently, Bouta et al., reported *in vivo* lymph viscosity in the collecting lymphatic draining the hind-limb by calculating the diffusion coefficient of fluorescently labeled albumin following in vivo multi-photon fluorescence recovery after photobleaching (MP-FRAP) and then utilizing Stokes-Einstein equation to estimate the viscosity [142,143].

The main hindrance in measuring lymph viscosity has been the relatively small sample volumes collected through the various lymph collection techniques [144]. These small volumes make it difficult to obtain complex fluid properties through conventional rheology measurements which typically require sample volumes larger than a millimeter [145]. Moreover, conventional rheometers provide an average measurement of the bulk response, and do not allow for local measurements in inhomogeneous systems [146]. Complex fluids, such as lymph, demonstrate behavior intermediate between solids (completely elastic) and fluids (completely viscous), and accurate methods are thus required to quantify the phenomena associated with their viscoelasticity [147]. As a result of miniaturization, improvements in imaging technology and computing power, a new category of rheology, microrheology, has emerged. Microrheology probes the material response on micrometer length scales and typically requires less than 10 μL of sample [148] with the ability to even probe intracellular rheological properties [149]. Here we utilize a passive microrheology technique which uses the Brownian motion of embedded florescence particles to accurately measure the viscosities of rat lymph during a fasting state as well as the transient changes occurring over a 4-hour period following a high-fat meal. Measurements were carried out for lymph containing and lacking anti-coagulant.

4.3. Methods and Materials

Lymph Collection

Male, Sprague-Dawley rats (weighing approximately 300g) (Harlan Laboratories, Indianapolis, IN) were housed individually and maintained in a temperature and humidity controlled facility, on a 12-h light/dark cycle. Animals had free access to water and standard chow (Harlan Teklad 7012 Mouse/Rat Sterilizable Diet, Harlan Laboratories, Indianapolis, IN) prior to all procedures. All animal procedures were approved by the University of Cincinnati Institutional Animal Care and Use Committee.

Prior to placement of lymph cannulas, the animals were fasted overnight with free access to water. Under Isoflurane anesthesia, a midline incision was made and a cannula (polyvinyl chloride tubing, 0.5 mm inner diameter, 0.8 mm outer diameter, Tyco Electronics, Castle Hill, Australia) was placed in the major mesenteric lymphatic duct as described by Bollman [61]. The lymphatic cannula was secured with cyanoacrylate glue (Krazy Glue, Columbus, OH). A silicone feeding tube (1.02 mm inner diameter, 2.16 mm outer diameter, VWR International, West Chester, PA) was introduced into the stomach and advanced slightly beyond the pylorus into the duodenum. The feeding tube was secured with a purse-string ligature in the stomach. Both the lymph cannula and the duodenal feeding tube were exteriorized through the right flank; the abdomen was then closed in two layers. After surgery, the animals were placed in Bollman restraint cages and allowed to recover overnight (18 h). The animals were kept in a temperature-regulated chamber (24°C) to prevent hypothermia. To compensate for fluid and electrolyte loss due to lymphatic drainage, a 5 % glucose-saline solution was infused into the duodenum at 3 mL/h for 6-7 h, followed by an overnight infusion of saline only at 3 mL/h.

Following overnight recovery, fasting lymph was collected for 1 h prior to a 3 mL duodenal bolus of lipid (2.2 mL Liposyn II and 0.8 mL saline). Thirty minutes following the bolus, a 0.9% saline infusion was provided at 3 mL/h for the remainder of the study period. Lymph samples were continuously collected on ice every 15 minutes for 4 hours. The anti-coagulant containing samples were treated in the same manner except upon

collection a cocktail of 10% by volume of an anti-proteolytic cocktail (0.25 M EDTA, 0.80 mg/mL aprotinin and 80 U/mL heparin) was added to each collection tube.

Triglyceride and Viscosity Measurements

Lymphatic triglyceride concentrations were determined using a commercially available kit (Randox TG, Randox Laboratories Ltd., Crumlin, Northern Ireland, UK). Lymph samples were shipped on ice overnight from Cincinnati, OH to Atlanta, GA for viscosity measurements. Fluorescent carboxylate-modified polystyrene (PS) FluoSpheres® (Molecular Probes,Inc.) with 1.0 µm diameters and 3 % polydispersity were used; Pluronics F-127 ($EO_{100}PO_{70}EO_{100}$, MW ~ 12,600 g/mol) from Sigma Chemicals was used without further purification for surface modification of the PS particles to prevent non-specific interactions between the lymph and the tracer particles [150]. Samples were prepared by combining 1.5 µL of tracer particle suspension with 50 µL of lymph and gently mixing the samples by repeated loading and dispensing of the pipette. The samples were then loaded into ~100 µm thick sample chambers, which were created by placing parafilm spacers between a microscope slide and cover slip, and sealed with vacuum grease to prevent evaporation. The samples were placed on the Peltier-controlled thermal microscope stage (PE100-LI2, Linkam Scientific Instruments Ltd.) that was used for effective temperature control of the sample during measurements; the sample temperature was carefully monitored using a thermocouple (HH11B, Omega) that was attached to the sample chamber.

Viscosity information of the samples was obtained by performing statistical analysis of mobility of colloidal tracer particles via particle tracking video microscopy (PTVM) [151]. The Brownian motion of fluorescent tracer particles in the samples was monitored at 38°C (rat internal body temperature) via an optical microscope (Leica DM-IRB) with a 63× objective, and movies were captured using a CCD camera (Cohu 4920, Poway, CA; 30 frame/s and 640 × 480 pixel resolution). Subsequently the recorded movies were analyzed with software developed using Interactive Data Language (ITT Visual Information Solutions, Boulder, CO). Because Brownian motion leads to small particle displacements on these timescales and is highly sensitive to external vibrational noise, all

experiments were performed on a vibration-isolated optical table. After obtaining video images, we utilized a standard brightness-weighted centroid method to identify the particle trajectories. The method uses four major steps: restoring the image, locating possible particle centers, refining particle positions/eliminating unwanted particles, and linking particle positions into trajectories [148]. A control sample with well-documented viscosity (DI water at 38°C) was used to confirm the accuracy of our protocol.

Through the Einstein-Stokes relation it is possible to relate the mean squared displacement of the particles, that occurs over time τ, and the viscosity of the fluid using the following expression:

$$MSD = \frac{d \cdot k_B \cdot T}{3 \cdot \pi \cdot \eta \cdot a} \cdot \tau \qquad (1)$$

where MSD is the mean squared displacement, d is the dimensionality, k_B is Boltzman's constant, T is the temperature in Kelvin, η is the viscosity, and *a* is the radius of the particle. Therefore, a linear relationship can be proposed using equation (1) with the slope being:

$$slope = \frac{MSD}{\tau} = \frac{d \cdot k_B \cdot T}{3 \cdot \pi \cdot \eta \cdot a} \qquad (2)$$

Solving for the viscosity, η:

$$\eta = \frac{d \cdot k_B \cdot T}{3 \cdot \pi \cdot a \cdot slope} \qquad (3)$$

Statistical Analysis

Statistical differences were determined using a paired Student's t-test. Significance was defined as $p < 0.05$. One value for TG concentration (rat 7, t = 105 min) was treated as an outlier after using an Iterative Grubbs' outlier test and confirming that sudden jumps in TG concentration are due to measurement error. Correlation levels were determined using the Pearson correlation coefficient. Sample size was n = 7 for samples

without an anti-coagulant and n = 4 for those with. All statistical analyses and plots were carried out in GraphPad Prism v6.

4.4. Results

Fasting Lymph

Lymph collected before the start of the duodenal lipid infusion provided typical baseline values for a fasted state. The fasting triglyceride (TG) concentrations ranged from 31 mg/dL to 170 mg/dL with a mean of 108 mg/dL (**Figure 20A**). The fasting viscosity ranged from 0.67 cP to 0.72 cP with a mean of 0.70 cP (**Figure 20B**). Fasting viscosity values were very close to that of distilled water at 38 °C.

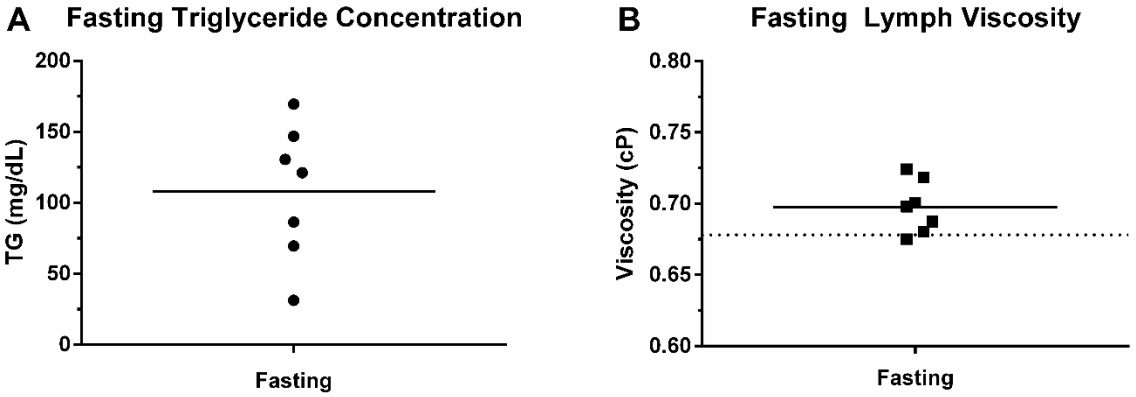

Figure 20: **TG and viscosity values for lymph in a fasting state. A)** Triglyceride concentration for fasting rat lymph. **B)** Dynamic viscosity of fasting rat lymph. Dotted line represents the viscosity of purified water at 38 °C as both reported by literature and measured with our technique. N = 7.

Transient Changes in Viscosity, Triglyceride Concentration and Lymph Flow

In order to determine the transient changes in viscosity following a high-fat meal, triglyceride concentration and lymph flow rate samples were collected at 15 minute intervals for up to 4 hours following the start of duodenal lipid infusion. The average lymph triglyceride concentration ranged from 107 mg/dL at the start of lymph collection to 709 mg/dL at 4 hours with a peak mean of 1098 mg/dL occurring at 2 hours. TG concentration increased relatively steeply up to 2 hours and then started a gradual decline (**Figure 21A, C**). The average lymph viscosity ranged from 0.70 cP at the start of lymph collection to 0.71 cP at 4 hours with a peak mean of 0.78 cP occurring at 1 hour. Viscosity values followed a similar trend to triglyceride concentration where they increased steeply up to 1 hour and then began a gradual decline (**Figure 21B, D**). Neither

TG concentration nor viscosity reached baseline fasting values within the 4-hour data collection interval. The mesenteric duct lymph flow rate varied with different rats (**Figure 22A**). The typical trend showed an initial decrease in flow rate from 39 µL/min to 13.6 µL/min after 30 minutes from the start of lymph collection and then began a gradual increase to a peak of 63 µL/min at around 180 minutes. Flow rate did not return to baseline value within the 4-hour data collection period (**Figure 22B**).

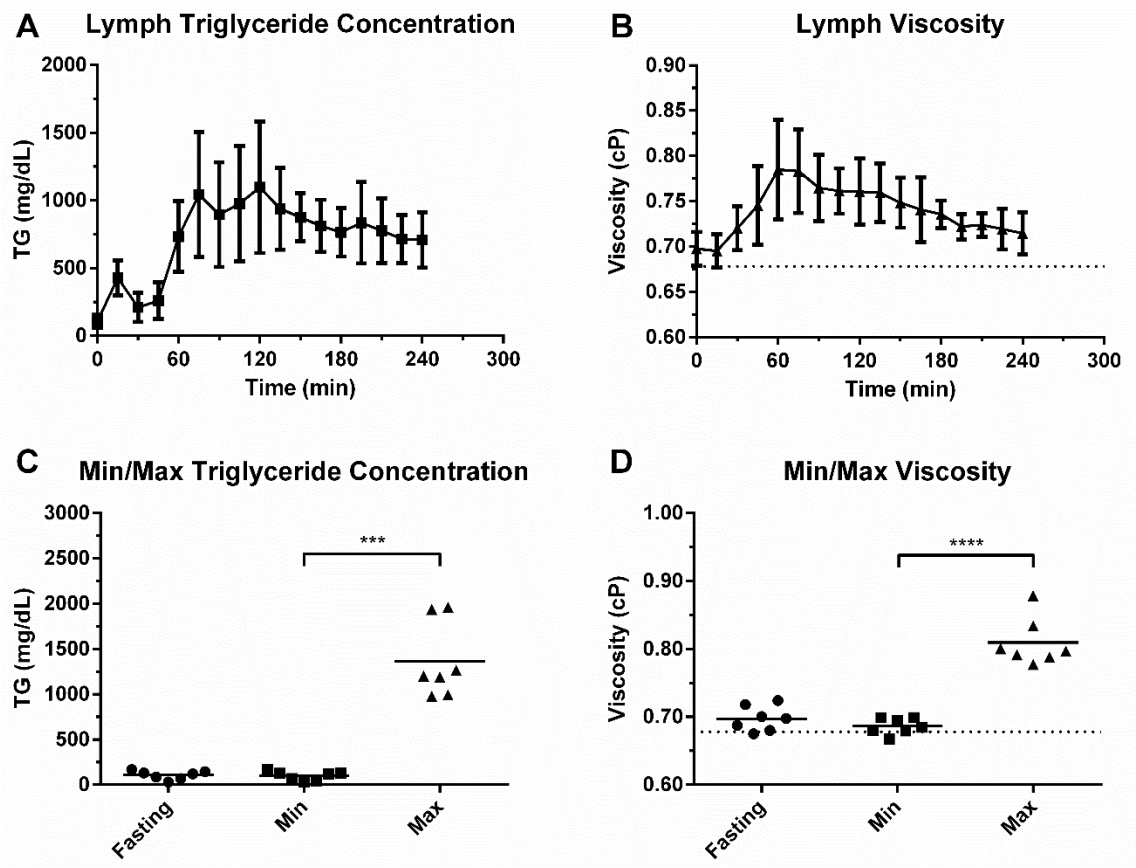

Figure 21: Transient changes in TG concentration and viscosity. A) Triglyceride concentration over a 4-hour period. Peak can be seen at around 1.5-2 hours. **B)** Viscosity over a 4-hour period. Peak occurs at around 1 hour and is earlier than the average peak TG concentration. Dotted line represents the viscosity of water at 38 °C. **C)** Maximum and minimum TG values measured throughout the time-coarse of the experiment. **D)** Maximum and minimum viscosity values measured throughout the experiment. Error bars represent SD. N = 7.

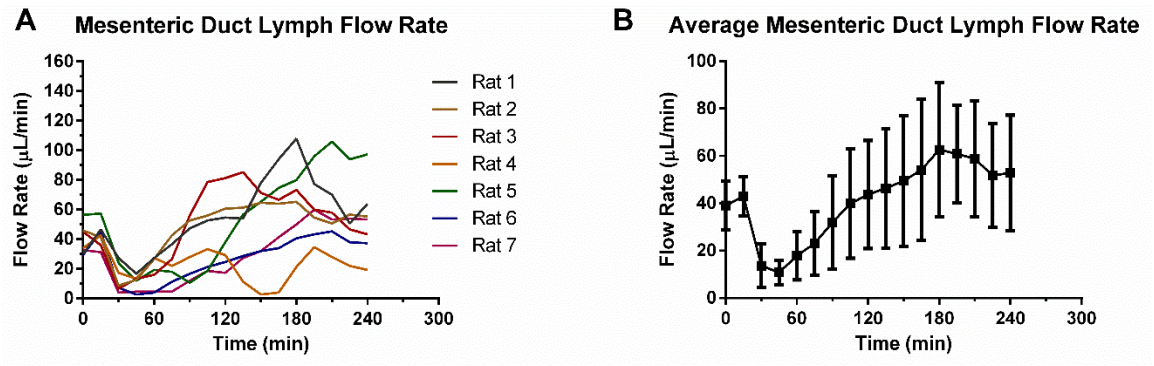

Figure 22: Mesenteric duct lymph flow rates. A) Lymph flow rates for each rat plotted separately showing the inter-variability between animals. **B)** Average mesenteric duct flow rate over a 4-hour period. N = 7, error bars represent SD.

Inter-Animal Variability

There was large inter-animal variability for both measured TG concentrations and viscosities. With one rat (rat 7) experiencing peak triglyceride concentration of 1961 mg/dL which is almost double that of the smallest peak (rat 5) which was 979 mg/dL (**Figure 23A**). The same can be said about viscosity values with one rat showing a peak of 0.88 cP (rat 7) compared to the smallest peak (rat 4) which measured 0.77 cP (**Figure 23B**). While in most cases there was a clear peak for both metrics, this peak was not consistent between rats and generally ranged from 1-2.5 hours depending on the animal.

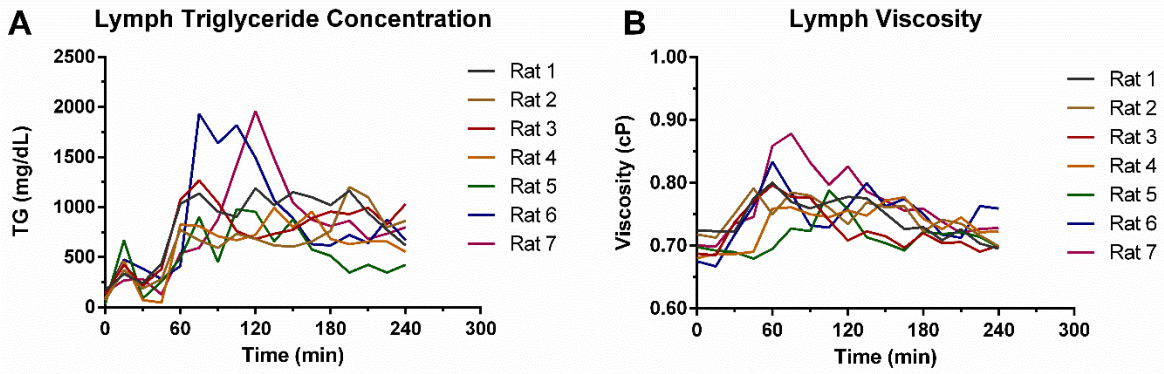

Figure 23: Inter-variability of TG ad viscosity values across animals. A,B) Triglyceride and viscosity values over a 4-hour period for 7 different rats.

Correlation between Triglyceride Concentration and Viscosity

Viscosity correlated positively with triglyceride concentration with a Pearson correlation coefficient of r = 0.38 (**Figure 24A**). The fasting viscosity and triglyceride concentrations showed lower correlation with r = 0.15 (**Figure 24B**). Dividing the readings into a rising segment (0-60 min) and falling segment (60-240 min) the values during the

rising segment seemed to be more correlated (r = 0.48, **Figure 24C**) than the falling segment (r = 0.29, **Figure 24D**). Breaking down the data into individual rats showed a large variability among correlation values, with rat 4 showing a correlation coefficient as high as 0.90 while rat 2 showed a negative correlation coefficient of -0.15 (**Figure 24E**). In **Figure 24F** correlation coefficients were broken down further for the rising segment (0-60 min) and falling segment (60-240 min). The data suggests that during the rising segment lipid concentration was more highly correlated with viscosity than during the falling segment.

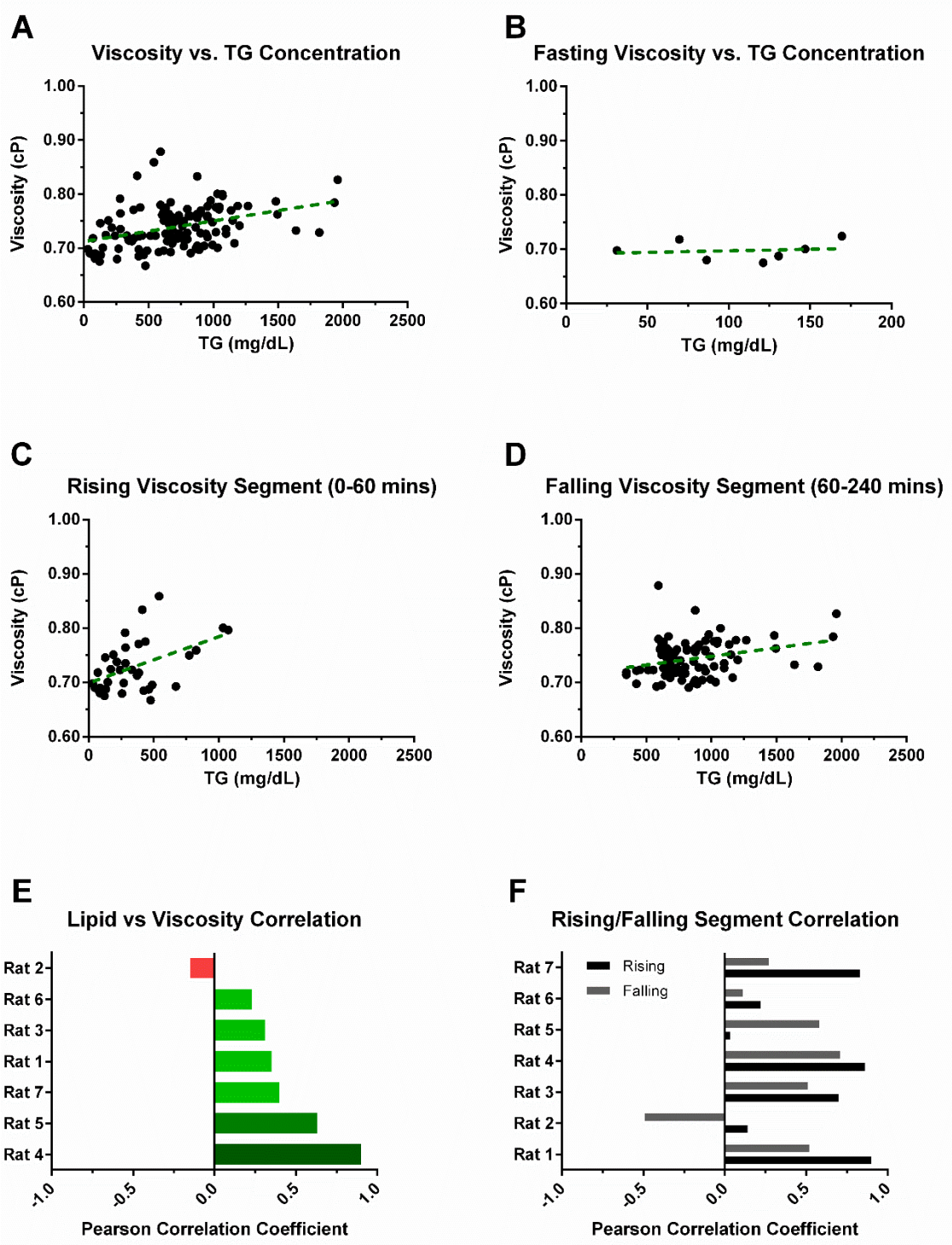

Figure 24: Correlation of lymph viscosity and triglyceride concentration. A-D) Correlation plots of viscosity vs TG for three different segments of the temporal profile. **E,F)** Pearson correlation coefficient demonstrating positive correlation between the TG content of lymph and viscosity values especially during the rising phase of the TG profile.

Viscosity Values are Higher Upon the Addition of an Anti-Coagulant Cocktail

Lymph has been shown to contain small amounts of coagulating factors which tend to promote coagulation upon collection [76,152]. So we sought to quantify the changes in viscosity that might result from a modified procedure. We found that in one of the rats the viscosity peak was as high as 1.32 cP (**Figure 25A**) while the average lymph viscosity peaked at around 1.04 cP (**Figure 25B**) compared to 0.78 cP when no coagulant was present in the samples. The mean fasting and maximum viscosities were 0.83 cP and 1.14 cP respectively (**Figure 25C and D**)

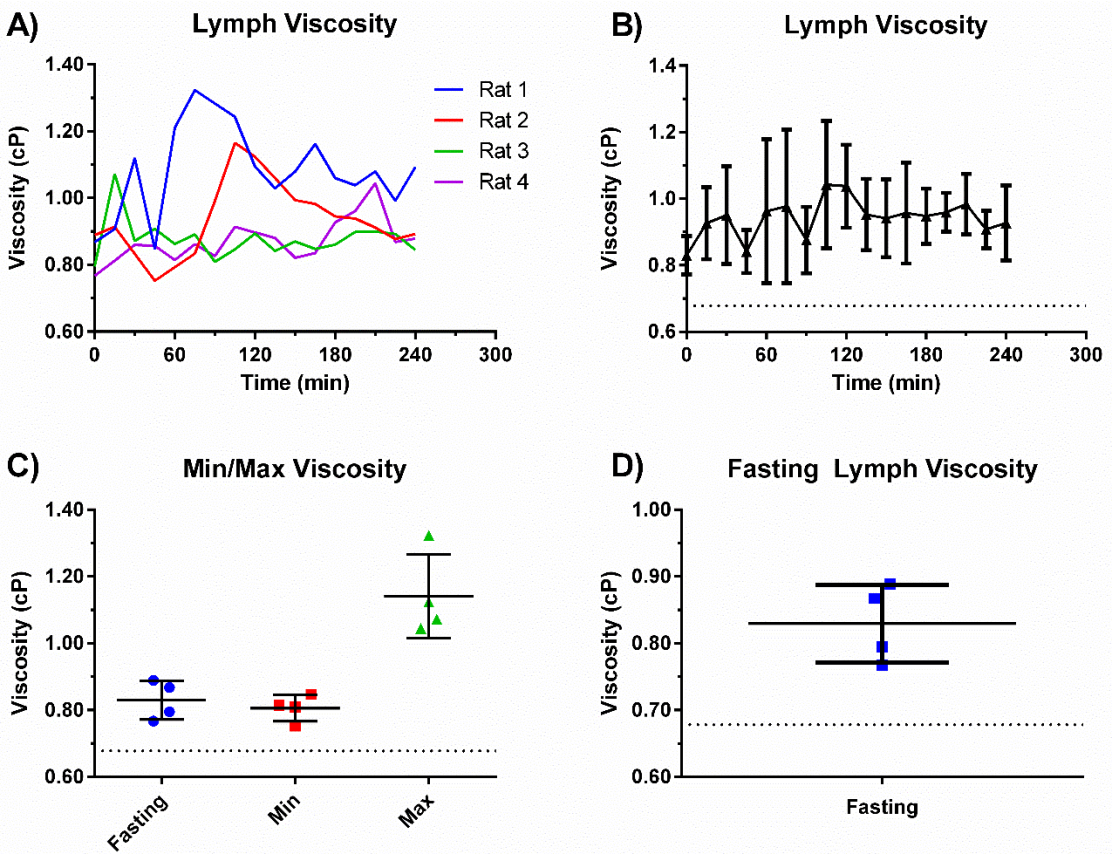

Figure 25: Viscosity with the addition of an anti-coagulant cocktail upon lymph collection. A) Viscosity values over a 4 hour period. **B)** Average viscosity values over the same period for all rats. **C,D)** Fasting, minimum and maximum viscosities in the presence of anti-coagulant. N = 4, error bars represent SD.

4.5. Discussion

Measurements of blood viscosity are prevalent in various health and disease conditions [153–156] but there exist very limited measurements carried out on lymph. In 1917, Burton-Opitz et al. measured the viscosity of lymph from dogs which had been given a moderate amount of fatty meat four hours prior to measurements. Lymph was collected from the thoracic duct and 2-3 mL of lymph was used for each measurement. They

showed that fasting lymph, which they measured 6 hours after the meal, was 1.5x (approx. 1 cP) the viscosity of distilled water at 37°C (approx. 0.69 cP) while peak viscosity during lipid absorption was around 2x (1.38 cP) that of distilled water [76]. The method they utilized during their study involved a conventional Ostwald viscometer in which lymph is directly flowed in a glass capillary under a given pressure and the flow rate is calculated. The kinetic viscosity can be backed out from the resulting measurements [157]. Recently, Bouta et al. were able to devise a method based on multi-photon fluorescence after photobleaching (MP-FRAP) to measure lymph viscosity in a lymphatic vessel afferent to the popliteal lymph node in a mouse arthritic joint [143]. The in vivo viscosity they reported was 1.8 cP which they noted was 1.8x the viscosity of distilled water, which would be correct for water at 20 °C. However, it was unclear at what temperature their calibration was carried out. Nevertheless, MP-FRAP may prove a useful technique for measuring in vivo viscosity when we have optical access to the vessel of interest. The limiting factor of their technique is the reliability of measuring the diffusion coefficient using FRAP. With the utilization of various rat animal models for research into lymphatic biomechanics [54,158,159] we decided in this study to measure both lymph viscosity in a fasting state and the changes in viscosity attributed to lipid absorption over a 4-hour period following a high-fat meal.

Conventional methods for measuring viscosity, including various forms of rheometers, typically require large sample sizes and do not lend themselves for time-course measurements of lymph samples from small animals. While lymph collection methods for small rodents have been used extensively for the past several decades [144,160] it is only recently that techniques capable of investigating the rheological properties at very small scales, known as microrheology, have become available. The availability of new microrheology techniques coupled with the ability to collect mesenteric lymph has made it possible to measure viscosities in a time dependent fashion and be able to correlate them with lipid concentrations. Technological innovations in light scattering and video microscopy, as well as theoretical advances have greatly expanded the power of microrheology. Current techniques can be divided into two main categories: active

methods that involve probe manipulation and passive methods that rely on thermal fluctuations to induce motion of the probes. In this study we used a passive method. Instead of using an external excitation to move the probe particles, the intrinsic Brownian motion of the particles was used [148,161] as described in Methods.

The correlation between lymph viscosity and TG concentration varied significantly between rats from being negatively correlated (r = -0.15) to being highly positively correlated (r = 0.9). In addition, there was a general trend where correlation was higher during the rise in TG concentration (0-60 min) versus the decline. These results are not surprising considering that lymph is a complex fluid composed of various constituents including immune cells, proteins and chylomicrons. The apparent viscosity of lymph is thus due to multiple factors. The TG concentrations calculated do not reflect the number or size of chylomicrons present in the sample. It has been previously shown that sizes of these particles range from 40-1,000 nm [162,163] and that during active lipid absorption their size rather than their number increases in response to increased TG content [164]. Lymphocyte density has also been shown to increase in response to lipid absorption by as much double the fasting values [22]. The fasting viscosity values showed almost no correlation between TG content and viscosity possibly due to the small differences in TG concentration (~150 mg/dL).

Whether the changes in viscosity have a considerable effect on shear mediated responses requires that we investigated the variations in shear stress typically experienced by mesenteric collecting lymphatic vessel. Flow rate after lipid infusion measured in the mesenteric duct increased from 13.6 µl/min to 63 µl/min (almost a 5x change) over a 4-hour period (Fig. 3B). This corresponds to an increase in WSS from 0.64 dynes/cm^2 in a fasting state [70] to around 3.2 dynes/cm^2. Thus the shear stresses, assuming Poiseuille flow, experienced purely because of viscosity changes are almost negligible (a 1.1x change when comparing min to max viscosity). And in more extreme cases such as in edema, we consider a recent study by Rhabar et al. in which rats were infused with saline via an intravenous infusion in order to induce edema. Average WSS in the mesentery lymphatic vessel increased from 0.12 dynes/cm^2 to nearly 1.5 dynes/cm^2 (a

10x change) and the maximum WSS rose from 5 dynes/cm^2 to 40 dynes/cm^2 (an 8x change) during the 25 minute post infusion observations [165]. Moreover, and in referring to Burton-Opitz study, in recent lymphatic literature a value of 1.5 cP for fasting lymph has been continuously used to estimate WSS in lymphatic vessels [63,70,117]. Here we found that the fasting lymph viscosity was approximately 1.3 cP which is very close to what is currently being used, thus showing that current literature estimates of WSS a lymphatic vessel is exposed to, are relatively accurate.

4.6. Conclusion

In summary, the viscosity values presented in this study, for both fasting lymph and the changes seen post-prandially after a high-fat meal, will allow researchers to more accurately elucidate the biomechanics involved in shear mediated lymphatic vessel response.

V. INTRACELLULAR CALCIUM DYNAMICS IN LYMPHATIC ENDOTHELIAL CELLS UNDER OSCILLATORY AND LIPID LOADS

5.1. Abstract

Mesenteric lymphatic vessels are responsible for the absorption and transport of chylomicrons from the intestine to venous circulation. These vessels are exposed to oscillatory shear stress as well as high lipid loads. We have previously shown that pre-nodal collecting lymphatic vessels respond to a high lipid load through a reduction in pumping activity and overall vessel diameter. Many vasoactive substances that are believed to be involved in vessel regulation, such as nitric oxide, utilize intracellular Ca^{2+} as a secondary messenger. Here, we employed intracellular Ca+ measurements using a fluorescence indicator, Fluo-4 AM, as a real-time readout to assess the response of human lymphatic endothelial cells to both oscillatory shear stress and exposure to high lipids, in the form of very low density lipoproteins (VLDL). We found that these cells have a longer response duration when exposed to oscillatory shear stress compared to a ramp profile having the same peak magnitude. We also found that lymphatic endothelial cells exposed to VLDL for 24 hours have a prolonged Ca^{2+} response compared to controls. These results show that lymphatic endothelial cells can sense the type of shear they are exposed to in addition to the fact that VLDL activates calcium mechano-sensitive pathways that are yet to be determined.

5.2. Introduction

The contractile activity of collecting lymphatic vessels has been shown to be regulated biochemically [93–98] and mechanically [132] through both intraluminal pressure [99] and wall shear stress [11,128]. Unlike the blood vasculature, lymph flow in lymphatic vessels is oscillatory in nature [70] due to the contractility of individual lymphatic segments, called lymphangions, and their separation with unidirectional valves [166]. Several studies have implicated the lymphatic endothelium to be the main player in regulating pumping activity due to its direct exposure to mechanical forces, mainly shear stress, and lymph content, such as vasoactive substances. Lymphatic endothelial cells, similar to blood

endothelial cells, increase their endothelial nitric oxide synthase (eNOS) expression in response to shear [54,167]. This translates to nitric oxide (NO) release which acts on lymphatic muscle cells surrounding the endothelium to regulate contractility though alterations in both contraction amplitude, contraction frequency and vessel diameter [82,139]. Intracellular calcium is an important secondary messenger involved in a variety of cell-level responses [168]. Most notably, intracellular calcium leads to activation of eNOS and the subsequent release of NO [169,170]. Thus, imaging intracellular calcium provides a real-time indicator of how endothelial cells respond to a stimulus. While the response to a step shear stress profile has been recently quantified [171], it is not clear how lymphatic endothelial cells respond to an oscillatory shear profile experienced *in vivo*. We have recently shown that isolated rat mesenteric lymphatic vessels synchronize their contractile frequency with that of the oscillatory frequency of the shear waveform imposed on them (*Kornuta et al. 2015, paper in review*). We have also recently shown that pre-nodal collecting mesenteric lymphatic vessels reduce their contraction amplitude, frequency and both average and end diastolic diameter when exposed to high lipid loads in the form of chylomicrons (*Kassis et al. 2015, paper in review*). In this study we sought to quantify the calcium response of lymphatic endothelial cells to two important environments they are exposed to in the mesentery, mainly oscillatory shear stress and high lipid loads. While there are a variety of Ca^{2+} indicators in use, we chose one with a high fluorescence signal in order to detect any small oscillations in free Ca^{2+} that might be dynamically changing. Fluo-4 AM has both a high fluorescence signal when bound to free Ca^{2+} and low photobleaching compared to other dyes [172–174]. While it is difficult to use a non-ratiometric indicator to quantify absolute intracellular calcium concentrations, our main goal in this study was to elucidate the spatio-temporal dynamics of the signal. Hereon, we report the intracellular Ca^{2+} response dynamics of lymphatic endothelial cells to a ramp and sinusoidal shear profile peaking at 4 dyn/cm^2, and both the shear sensitivity and response of these cells when exposed very low density lipoproteins (VLDL) which is close in size and lipid content to chylomicrons.

5.3. Methods and Materials

Lymphatic Endothelial Cell Culture

Human dermal microvascular endothelial neonatal lymphatic cells (HMVEC-dLyNeo, Lonza, New York) were cultured in T25 polystyrene flasks at a seeding density of 5,000 cells/cm^2. Flasks were coated for 1 hr at room temperature with a collagen solution containing type I rat tail collagen (BD Biosciences, San Jose, CA) at a concentration of 50 µg/mL in 0.1% acetic acid (Sigma). The cells were grown in EBM-2 supplemented with the EGM-2 BulletKit (both from Lonza). Cells in the flasks were grown to passage 6 and trypsinized at 60-90% confluency preceding seeding in the flow chambers. Cells used for all experiments were at passage 7 within the flow chambers.

Flow Chamber Set-up and Fluo-4 Dye Loading

In order to impose flow, cells were seeded in a polystyrene based flow chamber measuring 3.8 mm in width and 0.4 mm in height (µ-Slide VI 0.4 ibiTreat, IBIDI, Munich, Germany). The flow chambers were coated with the same collagen solution as above for 1 hr. Cells were then seeded at a density of 20,000 cells/cm^2 and given 48 hours to reach full confluency. Experiments were carried out 48 hours post-seeding. EBM-2 culture media was replenished at 24 hours. For the case of the VLDL treated group, cells were incubated for 24 hours with 10 mg/mL TG content (in EBM-2) from human plasma (Lee Biosolutions, St. Louis, MO). Immediately before the start of an experiment, cells within the flow chambers were rinsed 2x with pre-warmed serum-free DMEM-F12 (Life Technologies, Grand Island, NY). DMEM-F12 with HEPES was used for pH stability at room temperature and CO_2 levels. In addition, due to autofluorescence of phenol red in the green channel the media chosen was phenol red free. All uses of DMEM-F12 in this study was serum free. To image intracellular calcium dynamics, Fluo-4 AM (Life Technologies) with a final concentration of 10 µM in DMEM-F12 as a buffer was incubated with the cells for 30 minutes at 37 °C. Cells were then washed with 2x with DMEM-F12 at room temperature and then incubated in the same media for 20 minutes at room temperature to allow complete de-esterification of the AM esters.

Oscillatory and Ramp Flow Ca^{2+} Measurements

A custom-built LabVIEW virtual instrument was created to control a 12-roller Ismatec REGLO Digital MS-4/12 peristaltic pump (IDEX Health and Science, Glattbrugg, Switzerland) using RS-232 commands sent at a sampling period of 200 ms to the pump in an approach similar to that previously published [141]. The program has the capability of imposing any arbitrary flow waveform. For this study a 0.1 Hz sinusoidal waveform with a peak amplitude of 4 dyn/cm^2 and DC offset of 2 dyn/cm^2 was used for the oscillatory study. For the ramp study, an upward ramp going from 0 to 4 dyn/cm^2 was used. Both stimuli lasted for 1 minute. Imaging was carried out using a Zeiss Axioobserver inverted microscope (Carl Zeiss Microimaging, Jena, Germany) with a 20x objective. A back-illuminated CCD camera (PIXIS 1024B, Princeton Instruments, Trenton, MJ) was used to acquire fluorescent images with 500 ms integration time and at 1 sec intervals. A mercury lamp source set at 20 % intensity (X-Cite, Lumen Dynamics, Ontario, Canada) was used to continuously excite the Fluo-4 dye. Fluorescence intensity was quantified using ImageJ by drawing a small region of interest (ROI) inside the nucleus of each cell. For each field of view 40-45 cells were randomly chosen for quantification (**Figure 26)**. An ROI over an area clear of cells was used to correct for background fluorescence for each image individually. The output metric used (F/F0) represents the fluorescence signal, F, divided by the average fluorescence for all images preceding the stimulus, F0. Images were saved and analyzed as 16 bit TIFFs. All image acquisition was carried out in Micro-Manger [175]. All Ca^{2+} experiments were carried out within a temperature controlled incubator at 27 °C. Fluo-4 showed very high leakage rates out of lymphatic endothelial cells at 37 °C making it extremely difficult to run these studies at physiological temperatures. For the oscillatory studies 60 seconds of baseline was obtained, stimulus was applied for another 60 seconds and then imaging stopped 180 seconds later for a total of 5 minutes. For the lipid studies only 30 seconds of baseline was obtained.

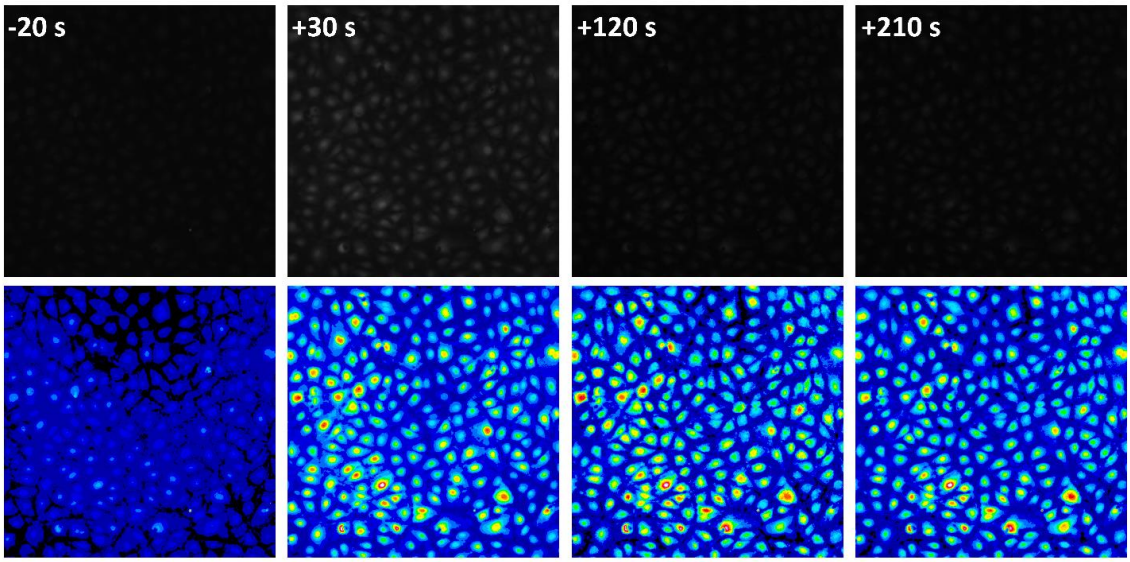

***Figure 26**: Human dermal microvascular endothelial neonatal lymphatic cells (HMVEC-dLyNeo) as seen under a 20x objective and captured with a 1024 x 1024 pixel back-illuminated CCD. Four representative images are shown. 20 seconds before the stimulus, then 30, 120 and 210 seconds subsequently after the stimulus. The top and bottom rows are the same images however the bottom row has been false colored with a 16 color palette. 40-45 cells were randomly chosen within this field of view for quantification. The region of interest was drawn within the nucleus.*

Statistics

Six independent experiments were carried out for each group. For each experiment 40-45 randomly chosen cells within the field of view were quantified to give an average for that experiment. All results are reported as mean ± standard deviation unless otherwise noted. Student t-tests were used to compare both the peak time between each of the two groups and the 120 s post-stimulation. Statistical significance was defined as having $P \geqslant 0.05$. All statistical analyses was carried out using Prims 6 (GraphPad Software Inc, La Jolla, CA).

5.4. Results

Intracellular Ca^{2+} Signaling Under Oscillatory Shear Stress

We quantified intracellular Ca^{2+} signaling in response to an oscillatory shear stress stimulus with a DC offset of 2 dyn/cm^2 and a peak amplitude of 4 dyn/cm^2. The stimulus was applied for 1 minute starting at 60 seconds post image acquisition. There was relatively high variability in the amplitude of the response between experiments. **Figure 27A** and **B** represent two different experiments where in '**A**' the peak was around one third in amplitude of that in '**B**'. The initial response time for the cells was consistent

between experiments and was evident from the rise in the average fluorescence as well as a sudden increase in the standard deviation measured across the cell population within the field of view.

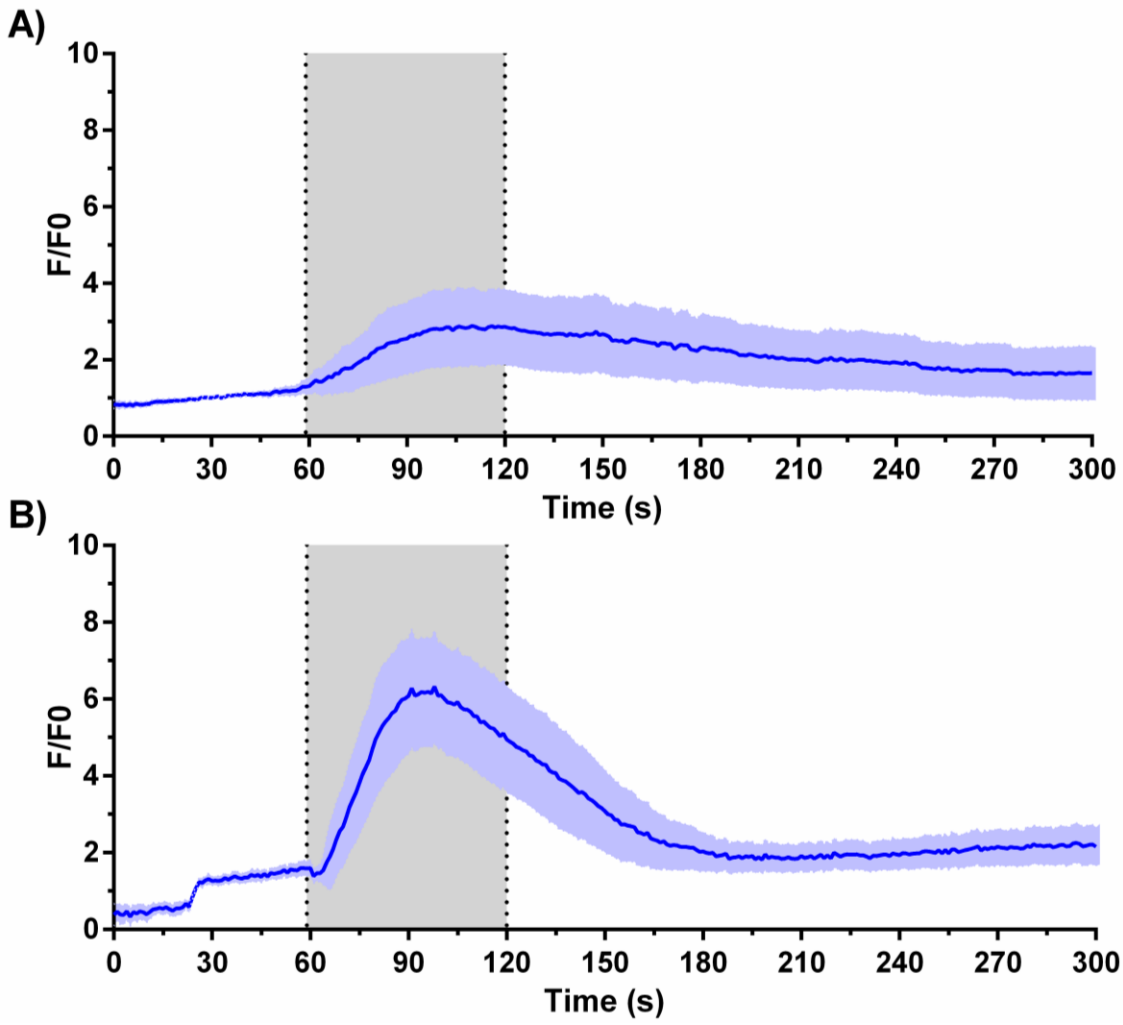

***Figure 27**: Fluo-4 fluorescence intensity for two representative experiments. There was a large variability in the amplitude of the peaks between experiments. The grey area represents when the sinusoidal shear profile was being applied. N = 40-45, error bands represent SD.*

In order to determine whether there was a dynamic oscillatory Ca^{2+} signal in response to the oscillatory shear stress we looked at the fluorescence signal of individual cells. Three different examples are shown in **Figure 28A**. There was a large difference in peak intensity, time to reach the peak and recovery rate between cells within the same experiment. The signal did not follow the sinusoidal input but seemed to initially respond to the input shear without any dynamic changes. Using the mean of all experiments

combined, the response to the sinusoidal stimulus began at 6 seconds post-stimulation and peaked at around 38 seconds post-stimulation (**Figure 28B**). Instead of just relying on average fluorescence intensity we quantified the fraction of cells that were activated. Although cells begin activating immediately after the stimulus, it is only after 40 seconds that all the cell population within the FOV becomes activated (**Figure 28C**). The activated cells remain in their activated state but the average fluorescence intensity (as seen from **B**) starts decreasing after the 38 second peak.

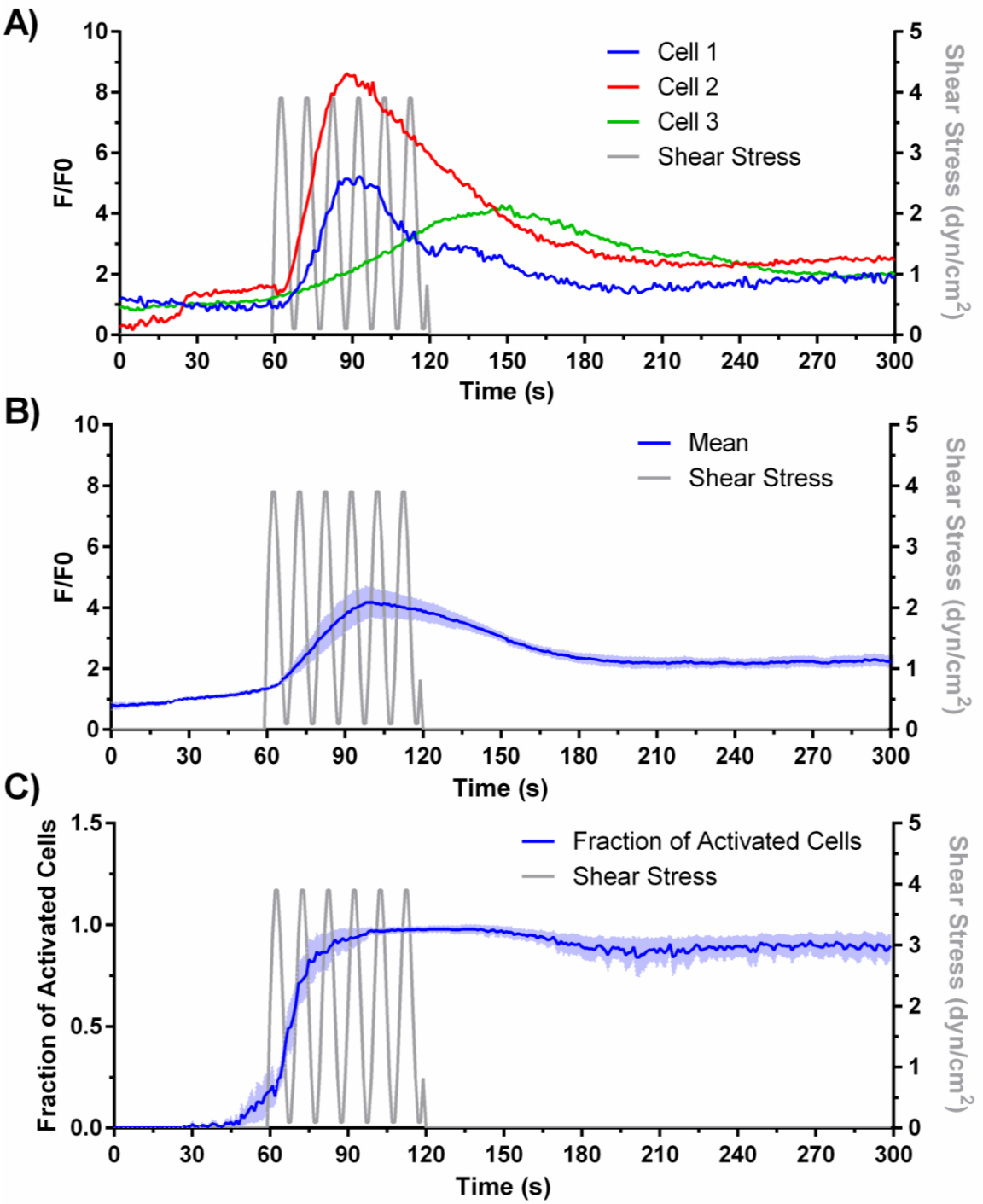

***Figure 28**: Intracellular Ca^{2+} dynamics in response to oscillatory shear. Grey signal represents the oscillatory shear waveform that was applied. A frequency of 0.1 Hz and amplitude of 4 dyn/cm² was used with a DC offset of 2 dyn/cm². The stimulus was applied for 1 minute starting at 60 seconds post-acquisition. A) The fluorescence response for 3 representative cells. Cells did not seem to exhibit a dynamic Ca^{2+} signal. B) The mean response for all experiments combined. C) The fraction of cells activated within the FOV being analyzed. N = 6, error bands represent SEM.*

Oscillatory vs. Ramp Shear Stress Exposure

While the response of lymphatic endothelial cells to a step shear exposure has been quantified previously [171] we wanted to test the hypothesis that these cells are capable of sensing the type of shear profiles they are exposed to. We chose a ramp profile from 0-4 dyn/cm^2 to compare to our sinusoidal stimulus applied earlier. We found that the intracellular Ca^{2+} peaked at the same time for both exposures (**Figure 29A**) but interestingly the recovery rate was significantly lower for the oscillatory stimulus. Quantifying the fraction of activated cells allowed us to distinguish between average intensity and the number of cells that are involved in the response (**Figure 29B**). The response until up to the 115 second time-point appeared to be mainly due to fluorescence intensity indicating a stronger response, but after the 115 second time-point more cells remained activated in the oscillatory condition. We chose a time-point at 150 seconds (120 seconds post-stimulus) when the signal seemed to stabilize and quantified the fluorescence intensity remaining in the cells. We found that the cells exposed to the oscillatory shear exhibited both a longer response and the calcium signal did not return to baseline within the time-frame of our experiment compared to the ramp case ($P = 0.007$), but in both, the peak arrived at the same time ($P = 0.08$) (**Figure 30**). To further support this point we quantified the area under both curves and found that the area for the oscillatory case was almost 1.7x higher than the ramp case (ratio = 411/245).

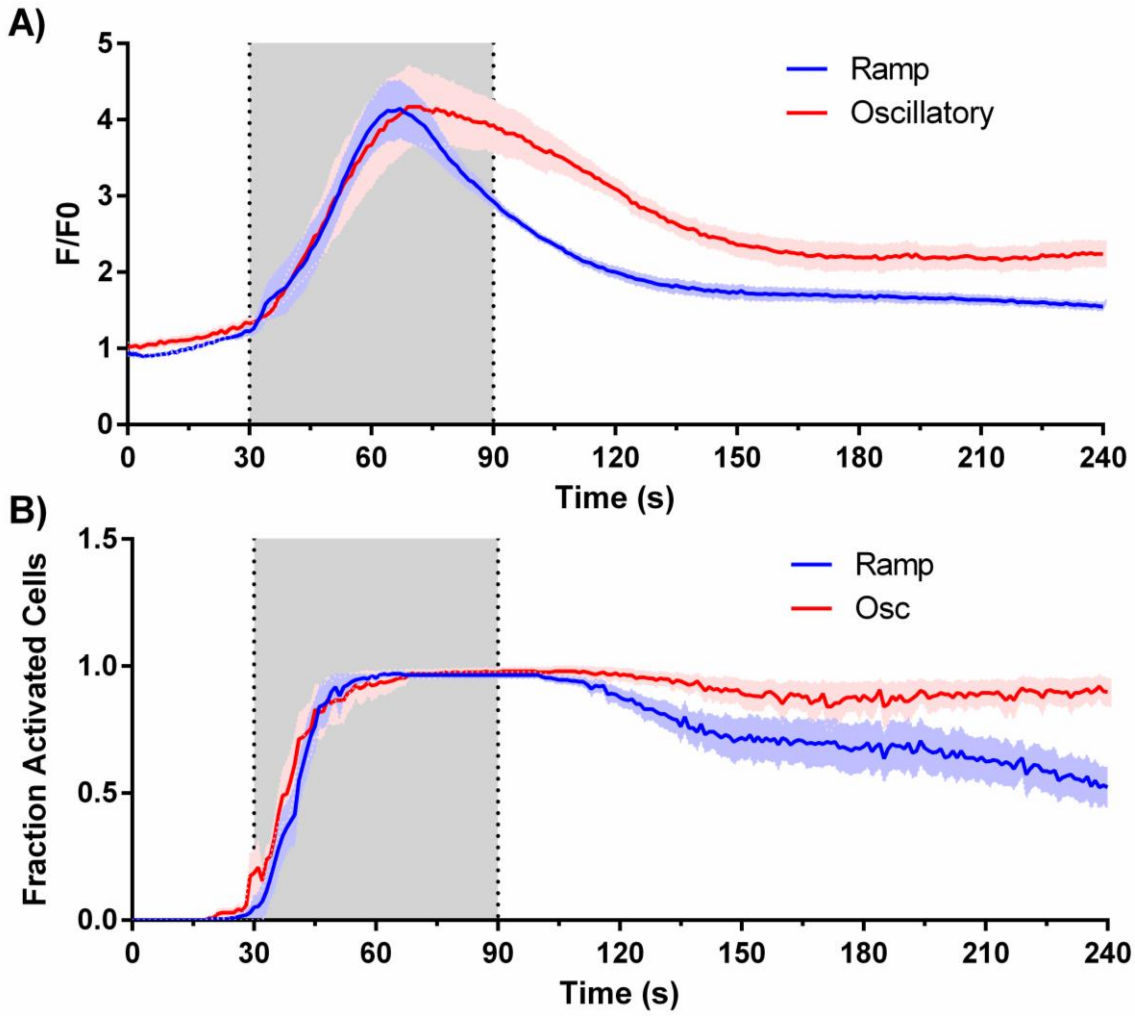

***Figure 29**: Quantifying the intracellular Ca^{2+} response of lymphatic endothelial cells exposed to both a ramp and oscillatory shear profile. A) Both ramp and oscillatory shear stimuli were applied at 30 seconds for a total of 1 minute. With the oscillatory stimulus there seems to be a more persistent Ca^{2+} response. B) The two had the same fluorescence peak both in amplitude and time of occurrence (P = 0.08). C) Quantifying the difference in fluorescence intensity at the 120 s time-point we can see a significant difference (P = 0.007) in terms of intracellular Ca^{2+} concentration remaining in the oscillatory case compared to the ramp profile. N = 6, error band represents SEM, error bars represent SD.*

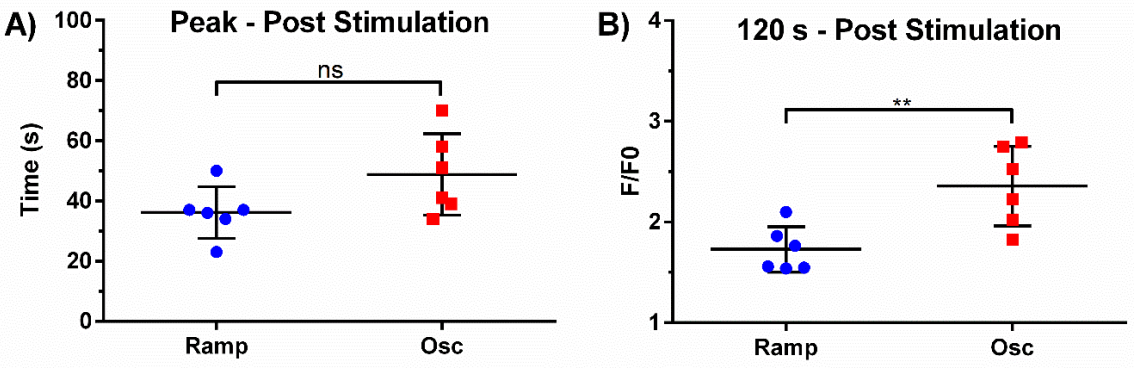

Figure 30: A) The peak fluorescence time was the same for both ramp and oscillatory conditions. B) In the oscillatory case, the fluorescence signal was significantly higher at 120 s post stimulation than the ramp group. This seems mostly due to a higher number of cells that have remained in their 'activated' state.

Shear Sensitivity of VLDL Conditioned Cells

In order to test whether exposure to lipoproteins affected the cells' ability to sense shear we incubated lymphatic endothelial cells with VLDL at 10 mg/mL triglyceride concentration (typical elevated levels occurring in a rat mesenteric lymph after a high fat meal) for 24 hours. To find out what shear stress level activated the mechano-transduction pathway we used a ramp profile going from 0 to 4 dyn/cm^2 over a 1 minute period and quantified fluo-4 fluorescence for both control and VLDL treated conditions (**Figure 31A**). There appeared to be a prolonged response mostly due to higher average intensity per cell before the 120 second mark and due to a higher number of cells remaining in their 'activated' state after that (**Figure 31B**). Looking more closely at the time-frame when we start seeing an increase in fluorescence (**Figure 31C**) there was no difference between both conditions. We calculated the moving standard deviation and defined a standard deviation of 0.25 as indicating a response. With this we were able to determine that for both conditions a shear stress value of 0.11 dyn/cm^2 elicited a response (**Figure 31D**).

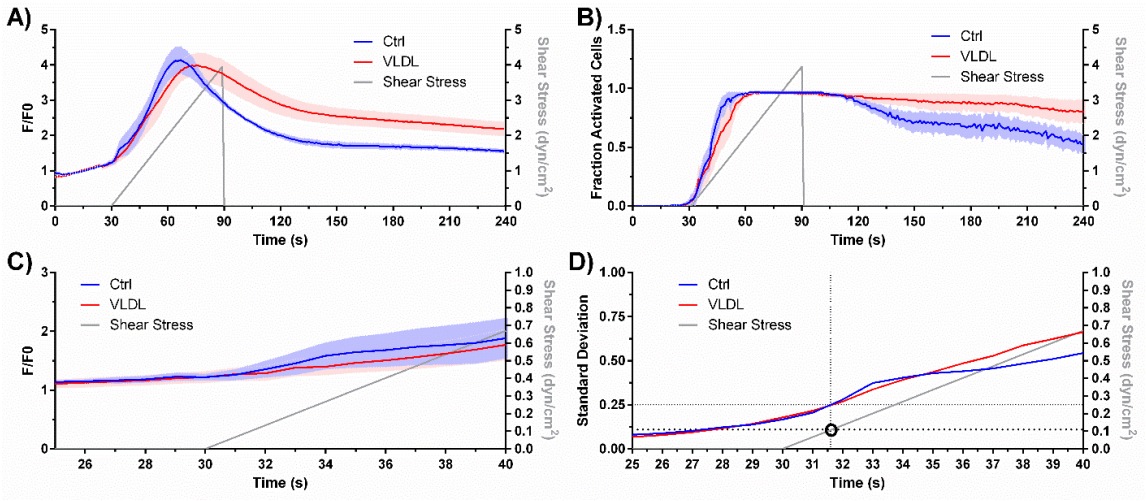

***Figure 31**: Determining the shear sensitivity of lymphatic endothelial cells pre-incubated with VLDL. A) Both VLDL incubated cells and controls were exposed to a ramp shear stress profile going from 0-4 dyn/cm² for 1 minute. B) Fraction of 'activated' cells. While there was a differential response in terms of how fast intracellular calcium was cleared there did not appear to be a difference in the initial shear stress exposure required to elicit a response (C). To further clarify this the standard deviation was calculated over time and a value of 0.25 was defined as being responsive. Shear sensitivity was calculated to be around 0.11 dyn/cm² for both groups (D). N = 6, error bands represent SEM in (A) and (B), and SD in (C).*

The fluorescence peak and time of occurrence for the VLDL treated group was the same for that of the control (P = 0.259) (**Figure 32A**). The VLDL treated group however has a longer response and slower clearance rate as evident by the fact that the area under the curve for the VLDL group was 1.57x greater than the control (ratio = 386/246). At 120 s post-stimulation there was a significant difference in the remaining intracellular calcium signal (P = 0.0093) (**Figure 32B**).

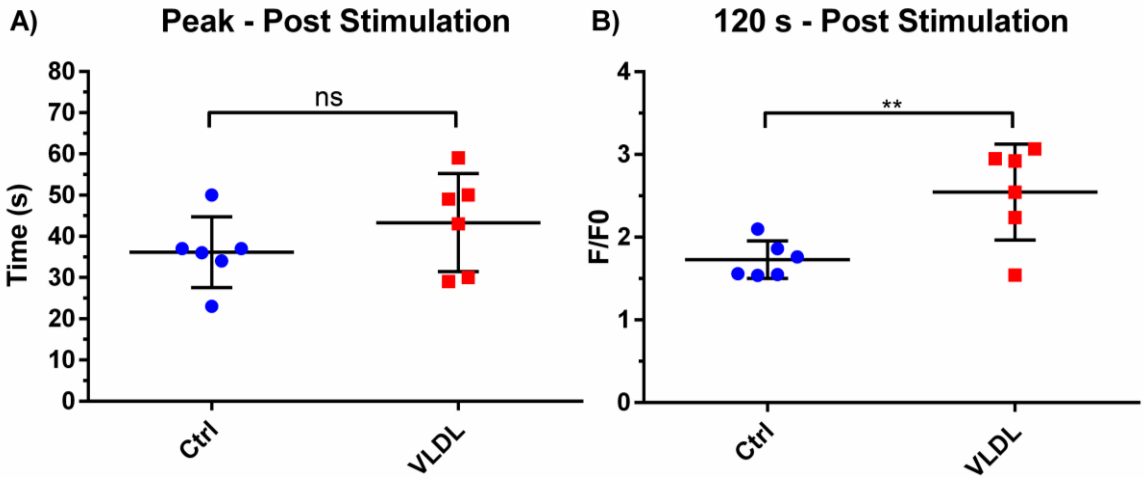

***Figure 32**: Quantifying the effect of VLDL pre-incubation on peak response and clearance dynamics. A) The peak fluorescence in both amplitude and time of occurrence for VLDL incubated cells was the same as control. B) The fluorescence signal for the VLDL treated group was significantly higher at 120 s post-stimulation compared to controls. This could likely indicate an increased Ca^{2+} concentration compared to control. N = 6, error bars represent SD.*

5.5. Discussion and Conclusion

Our preliminary findings presented here demonstrate that lymphatic endothelial cells (LECs) respond to the local environment that they are exposed to in mesenteric lymphatic vessels. LECs appear to have the capacity to sense the type of shear stress profile they are exposed to even when both the average and peak magnitudes were the same in both the ramp and oscillatory flow cases. This is not very surprising considering oscillatory flow induced higher intracellular calcium flickers than other types of flow profiles in osteoblasts [176] and blood vascular cells were shown to be able to sense the direction of flow and align accordingly [177] but in our study the net direction and average magnitude were always the same but the instantaneous magnitude dynamically changed. While we initially hypothesized that the Ca^{2+} signal would follow the shear profile this did not turn out to be the case. It seemed that when a given cell was exposed to shear it

'switch on' and was blind to further changes in the shear magnitude and direction. The cells exposed to oscillatory flow seemed to have a stronger intracellular Ca^{2+} signal indicating a more pronounced response that lasted longer than cells exposed to a ramp profile.

Recent work by Jafarnejad et al. 2015 [171] demonstrated the intracellular calcium response due to a step shear profile and showed that the peak occurred on the order of 1.5 minutes while with our cells the peak typically occurred within 40 seconds and the calcium signal started decreasing while the shear stimulus was still occurring. One main difference could be attributable to the cell line used. Whereby the origin of both our cells and the line Jafarnejad used were dermal lymphatics we obtained our line from Lonza while the other study used cells from PromoCell. In addition, the other study used Fura-2 measurements which are ratiometric in nature permitting more reliable calcium concentration calculations and less prone to erroneous readings due to photobleaching. Fluo-4 photobleaches to around half of its initial fluorescence intensity within 5 minutes when exposed to high light intensity (lower bleaching rate than fura-2) [178] . Due to the sensitivity of the back-illuminated camera we used, the decrease in the fluorescence signal is not due to photobleaching but actual decrease in Ca^{2+} binding.

While we showed interesting preliminary results on the temporal dynamics of intracellular calcium in response to both different shear profiles and incubation with VLDL, work is still in progress to clarify the molecular basis for these comparisons including the extent to which both local cell calcium stores and extracellular calcium influx play a role. Although eNOS has been shown to be shear mediated [179,180] it is difficult to conclude at this point that the intracellular calcium increase upon shear stimulation is due to the eNOS pathway. Further work quantifying mRNA expression post-stimulation might be required to determine if eNOS is in fact upregulated in the case of VLDL incubation.

VI. AN INTEGRATED IN VITRO IMAGING PLATFORM FOR CHARACTERIZING FILARIAL PARASITE BEHAVIOR WITHIN A MULTICELLULAR MICROENVIRONMENT

6.1. Abstract

Lymphatic Filariasis, a Neglected Tropical Disease, is caused by thread-like parasitic worms, including *B. malayi,* which migrate to the human lymphatic system following transmission. The parasites reside in collecting lymphatic vessels and lymph nodes for years, often resulting in lymphedema, elephantiasis or hydrocele. The mechanisms driving worm migration and retention within the lymphatics are currently unknown. We have developed an integrated *in vitro* imaging platform capable of quantifying *B. malayi* migration and behavior in a multicellular microenvironment relevant to the initial site of worm injection by incorporating the worm in a Polydimethylsiloxane (PDMS) microchannel in the presence of human dermal lymphatic endothelial cells (LECs) and human dermal fibroblasts (HDFs). The platform utilizes a motorized controllable microscope with CO_2 and temperature regulation to allow for worm tracking experiments with high resolution over large length and time scales. Using post-acquisition algorithms, we quantified four parameters: 1) speed, 2) thrashing intensity, 3) percentage of time spent in a given cell region and 4) persistence ratio. We demonstrated the utility of our system by quantifying these parameters for L3 *B. malayi* in the presence of LECs and HDFs. Speed and thrashing increased in the presence of both cell types and were altered within minutes upon exposure to the anthelmintic drug, tetramisole. The worms displayed no targeted migration towards either cell type for the time course of this study (3 hours). When cells were not present in the chamber, worm thrashing correlated directly with worm speed. However, this correlation was lost in the presence of cells. The described platform provides the ability to further study *B. malayi* migration and behavior.

6.2. Introduction

Lymphatic Filariasis (LF) is the single largest world-wide source of secondary lymphedema [26] and is caused by adult parasitic nematodes that target and dwell in the lymphatic system. An estimated 120 million people in 73 countries are currently infected, and a further 1.4 billion live in areas where filariasis is endemic [27]. Of the 120 million people harboring the parasites, 90% have *Wuchereria bancrofti*, while *Brugia malayi* and *Brugia timori* infections account for the other 10% [28]. All three parasites use mosquitoes as transmission vectors [29]. Infection is initiated when the host-seeking mosquito deposits an infective third-stage larva (L3) on the skin of the host during the process of obtaining a blood meal. The infective larvae then penetrate the skin at the site of the bite, presumably guided by chemoattractants [30], and migrate to the lymphatic vessels and lymph nodes of the host where after 6-12 months they mature into adult worms. The adult worms may reside within the lymphatic system for years before the host shows any clinical manifestations such as lymphedema, hydrocele, elephantiasis, chyluria and compromised immunity [31–37]. Following mating in the lymphatics, the parasites release live progeny called microfilariae, which circulate in the bloodstream. These microfilariae can then be ingested by a mosquito during a blood meal, where they undergo development to form L2 and finally L3 larvae. Hence, the life cycle continues [32].

In the year 2000, the World Health Organization (WHO) launched the Global Alliance to Eliminate Lymphatic Filariasis (GAELF). The GAELF has been one of the most rapidly expanding global health programs in the history of public health with the goal of eliminating LF by 2020 through annual mass drug administration (MDA) [27,29,38,39]. While killing the adult worms is considered one of the best strategies, the drugs used in MDA are only effective at killing microfilaria, and not the adult worms [40–45]. Thus, breaking the cycle of transmission has proven to be difficult. Additionally, these treatment strategies provide no relief for the estimated 120 million people already infected. As we move from controlling the disease to eliminating it, an understanding of the mechanisms by which L3 filarial parasites target and migrate towards lymphatics and how they behave in the

presence of the lymphatic environment will be crucial in developing treatment strategies targeting the migration process as well as the lymphatic-inhabiting adult worms.

In vitro experiments suggest *B. malayi* induce local lymphatic remodeling via up-regulation of matrix metalloproteases (MMPs) [13] and actively secrete proteins to modulate immune function and evade detection [35]. Experiments with L3 *B. pahangi,* nonhuman filarial parasites, suggest sera isolated from mammals preferentially spur chemotaxis, possibly guiding worm penetration into the host at the bite site [30]. Additionally, experiments with intradermally injected *B. pahangi* exhibit differential gene expression compared to intraperitoneal injection [181]. These experiments suggest filarial parasites actively sense and respond to the local cellular microenvironment. Nematodes respond to a variety of different stimuli. Chemotaxis mediated by movement toward or away from chemical gradients, plays an important role in food- and mate-finding, and other aspects of nematode interactions. In very few cases have attractive substances been isolated and identified [182]. There is currently no high throughput *in vitro* imaging platform that allows researchers to quantify the complex interactions between these parasites and their multicellular host environment. Understanding how filarial worms interact with the multicellular microenvironment may reveal how they target and migrate towards the lymphatic system, and why they reside in it. This will provide invaluable insight for the anti-parasitic drug community and aid in the development of drugs that target the migration process and adult worms which will greatly aid in MDA elimination efforts. Additionally, it could lead to insight as to how worms utilize the unique environment of the lymphatic to enhance drug resistance and immune evasion.

Assays have been developed in recent years that quantify worm migration, development, behavior and viability [183–196]. Existing worm trackers either use the centroid position [192,197–199] of the worm or a ‘‘skeleton’’ of the worm’s shape [185,186,189,200–202] to track its location. Centroid-based trackers define worm position as the geometric center of the segmented worm in each video frame. They can follow multiple worms at low magnification or, with the aid of a motorized x-y stage and feedback control, they can follow single worms over multiple hours [197,198]. The throughput of such trackers can be

increased by operating several setups in parallel [203]. Centroid-based trackers provide limited information about the details of worm behavior such as thrashing. Skeleton-based trackers, by contrast, generally operate at high magnification and derive a skeleton of each worm from segmented images. These skeletons provide extensive information about behavior. Existing assays rely on motorized x-y motorized stages, read only single wells at a time, are low-throughput, and do not offer quantitative regional based tracking. While many of these systems have extensive uses, there is no current integrated platform that is capable of quantifying migration and regional cell-proximity based behavior of multiple worms in a multicellular microenvironment at high magnification.

Here, we describe a scalable platform that can track multiple worms in parallel, and extract key parameters describing migration and regional based behavior using a novel co-culture system which exposes a single L3 *B. malayi* worm to both lymphatic and dermal layer cell types. The application can process multiple worms simultaneously without user intervention, allowing for long-term experiments in a CO_2 and temperature controlled environment. This system can be used to assay large parasites such as filarial parasites and study their targeted migration towards a variety of desired cell types. Our system is scalable for a variety of multi-well devices providing the ability to alter the worm environment for high-throughput drug screening. In its current 7-lane configuration, we characterized the behavior and tracked the migration patterns of L3 *B. malayi* in the presence of cell types specific to the human interstitium by quantifying four key parameters; 1) speed, 2) thrashing, 3) percentage of time spent in a cell region, and 4) persistence ratio. Furthermore, we validated the platform's sensitivity to worm behavior by quantifying the effect of the common anthelmintic drug levamisole (in the form of tetramisole) [204,205] on L3 *B. malayi*.

6.3. Methods

Brugia malayi Culture

Freshly isolated L3 *B. malayi* parasites were obtained from the National Institutes of Health Filarial Research Reagent Resource (FR3) [206] at the University of Georgia (Athens, GA). Worms were rinsed in 5 successive washings with Endothelial Basal Medium

(EBM) (Lonza, New York) supplemented with 20% FBS (Atlanta Biologicals Lawrenceville, GA), 1% Glutamax, 1% Penicillin-Streptomycin-Amphotericin (Gibco, New York), 25 mg/mL cyclic-AMP and 1 mg/mL hydrocortisone acetate (both from Sigma, St. Louis, MO). The worms were then maintained in 10 mL of EBM at 37 °C in a 5% CO_2 incubator for at least 18 hours prior to experimentation.

Cell Culture

Lymphatic endothelial cells (LECs) were obtained through isolation from human neonatal foreskins via immunomagnetic separation using the LEC marker podoplanin as described previously [207]. The LECs were expanded in T75 flasks that had been previously coated for 1 h with a collagen solution containing type I rat tail collagen (BD Biosciences, San Jose, CA) at a concentration of 50 µg/mL in 0.1% acetic acid (Sigma). The cells were grown in EBM (Lonza, New York) supplemented with 20% FBS (Atlanta Biologicals), 1% Glutamax, 1% Pencillin-Streptomycin-Amphotericin (Gibco), 25 mg/mL cyclic-AMP, and 1 mg/mL hydrocortisone acetate (both from Sigma). LECs were split at 80-90% confluence and were used in experiments either at passage 8 or 9. Human dermal fibroblasts (HDFs) were cultured in Dulbecco's Modified Eagle Medium (DMEM) (Lonza) supplemented with 10% FBS and 1% Pencillin-Streptomyacin-Amphotericin. HDFs were split at 80-90% confluence and were used in experiments at passage 14.

Decision Chamber

The mold for the decision chamber was designed in Autodesk Inventor 2013 and milled in 6061 aluminum (**Figure 33A**). To construct a device, poly(dimethylsiloxane) (PDMS) with a 10:1 ratio of base to curing agent (Sylgard 184, Dow Corning) was poured in the mold, degassed for 20 minutes using a vacuum chamber, and then cured at 60 °C for a minimum of 8 hours. The mold featured seven equidistant linear lanes, which allowed for the culture of two different cell types in each lane. Each cell region (referred to as ‘well’ throughout) started with a 200 µm down step which allowed for additional fluid retention in the region during the cell seeding process but did not significantly impede worm movement. In addition, only the ‘well’ region was adherent to cells due to a collagen coating. Regions outside of the well (PDMS surface) did not allow cell adhesion

and thus prohibited cell migration. The device dimensions were chosen to provide the worm, which is placed in the center, with equal access to the cell types being evaluated in tandem (**Figure 33B** and **C**). The dimensions of each lane were 30 x 3 mm. Each cell region occupied 22.5 mm^2 (25% of the total lane area). Full schematics and CAD files of the mold are available upon request.

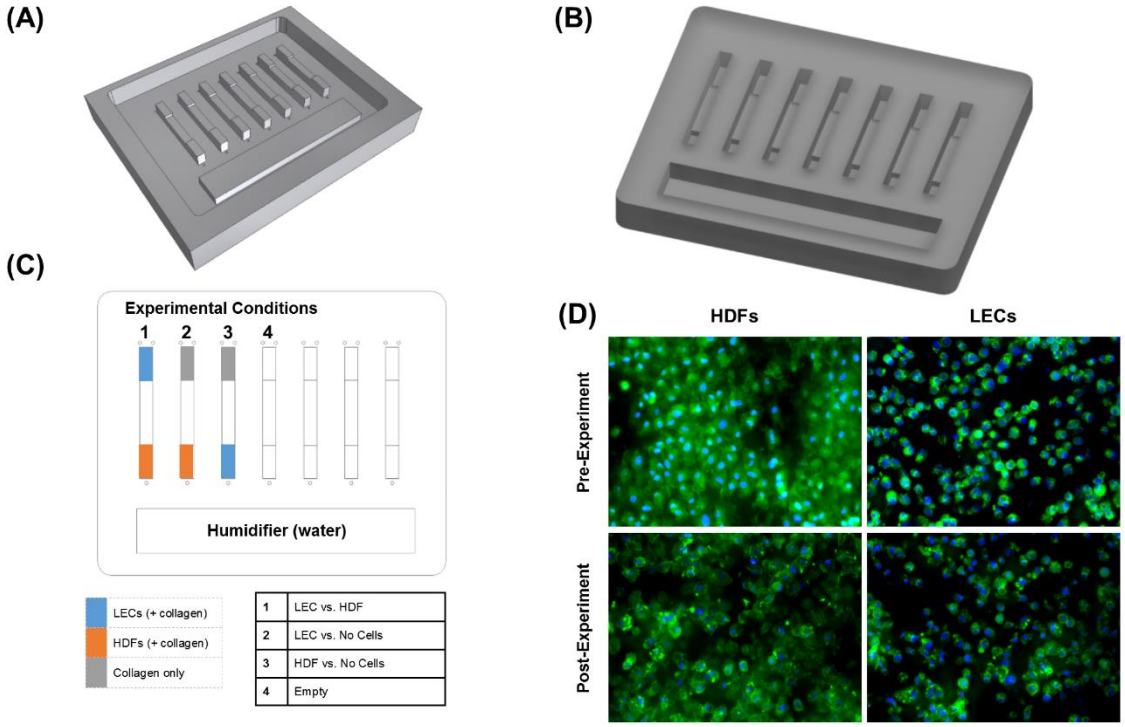

Figure 33: A worm-cell coculture device for studying nematode migration and behavior in a multicellular microenvironment. (A) *A rendering of the aluminum mold used to cast the PDMS device* ***(B)*** *A rendering of the PDMS-based coculture device consisting of seven parallel lanes.* ***(C)*** *A top-view schematic showing the various regions discussed in this study. Each cell region occupies approximately 25% of the total lane area. The 'humidifier' is filled with water in order to limit media evaporation, flow lanes are included in the device for future flow-related experiments but were not utilized in the current study.* ***(D)*** *LECs and HDFs cultured in the device before and after a 3-hour exposure time to the worm (blue = nucleus, green = Actin). Spreading of the cells was less pronounced than what would be seen on polystyrene plates due to the surface roughness of the machine PDMS mold. The presence of the worms in the device did not seem to affect cell viability.*

User Interface

A graphical user interface (GUI) was created in LabVIEW 2013 (National Instruments, Austin, TX). The GUI allows the user to select the number of lanes to track, the duration to track each worm for during an imaging cycle and the total experiment time. After setting the initial parameters, user interaction was no longer required. The

developed LabVIEW virtual instrument was also used to interface the microscope control dynamic link library (dll) with the rest of the imaging program.

Microscope Control

The Zeiss MTB2004 64 bit SDK along with Visual Studio 2010 (Microsoft, Redmond, WA) were used to create a C# dynamic link library (dll) allowing full control of a Zeiss AxioObserver Z1 inverted microscope (Carl Zeiss, Jena, Germany) along with a motorized x-y stage. The dll was accessed using a LabVIEW virtual instrument. The developed library allowed for full control of all microscope features including; filter-wheel, objectives, light intensity, incubation temperature and CO_2 levels, and x-y-z position.

Image Acquisition

Video frames required for centroid location and post-acquisition analysis were captured with a Guppy Pro CCD camera (Allied Vision Technologies, Newburyport, MA) at 15 frames/second (fps) with a resolution of 640 x 480 pixels. The program ran on a Lenovo Intel dual-core CPU with 4 Gb of RAM (Lenovo, Morrisville, NC) running Windows 7 64 bit. For the set of experiments carried out in this study a 2.5x microscope objective was used with a 0.5x C-mount camera adapter giving a total effective magnification of 12.5x (accounting for the 10x microscope phototube).

Tracking Algorithm

Video was acquired at 15 fps. Frames were stored as individual 8-bit compressed TIFFs. Each two consecutive frames were subtracted to obtain a difference image representing motion-based segmentation of the worm. The resulting image was then binarized using a clustering based thresholding approach using the included blocksets in the Vision Development Module 2013 (National Instruments). Small particles were then filtered out and a binary image convex hull function was applied. The centroid location of the resulting segment was then calculated and taken as being a close approximation to the worm centroid. The motorized stage was then moved in the x-y plane to align the calculated centroid with the static center of the camera field of view (FOV) thus moving the worm to the center of the FOV. This process is repeated every two seconds, while video of the worm is acquired, and the x-y position of the stage (representing the worm

location) is stored along with the corresponding time-stamp. The program then moves the stage to the next lane in which the center is pre-determined and repeats until all the lanes have been covered. When the program returns to a previously imaged lane, it moves to the last known location of the worm. If the worm was not found, it begins a scanning process from either the top or bottom of the lane until the worm is found. The scanning process alternates the direction of scanning to negate the effect of stage movement on worm displacement. Video is only stored when the worm is in the FOV. **Figure 34A** provides a block diagram representing pseudo-code for the worm tracking implementation. Full code is available upon request.

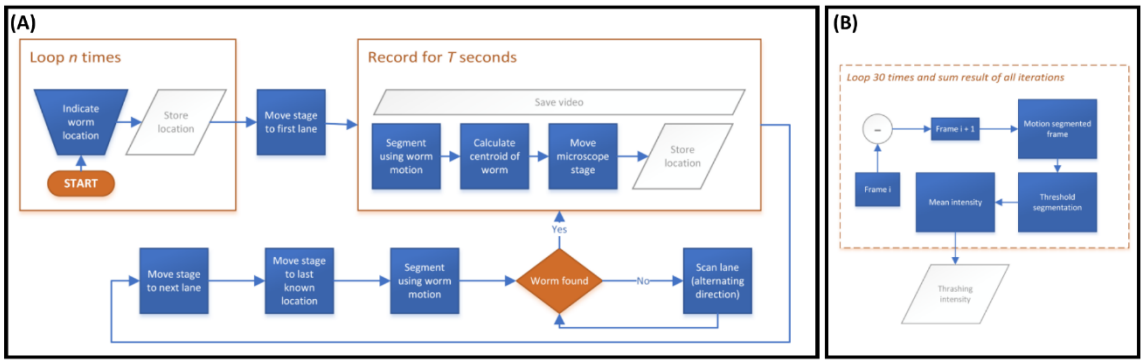

Figure 34: Block diagram of the worm tracking and thrashing algorithms. (A) *The procedural steps involved in the worm tracking algorithm. Initial worm location in each lane is determined manually. The program then starts the process of acquiring video and cycles through all the lanes by moving to the last known worm location. If the worm is not found, then a linear scanning process initiates in order to find the worm. The scanning process alternates the start position, hence the direction of movement, in order to negate the effect of the microscope stage movement on worm displacement.* ***(B)*** *The thrashing algorithm takes two consecutive images and subtracts them to remove both background and all static features. The resulting image represents degree of worm movement during the time period separating the two frames (~66 ms for a frame rate of 15 fps). The segment is then thresholded and the mean intensity of the resulting image calculated. The mean intensity is summed for the entire length of an imaging cycle (2 seconds) and the resulting values are normalized to obtain the 'thrashing index' metric.*

Experimental Procedure

The PDMS decision chamber was rinsed with 70% ethanol followed by deionized water and left in the oven at 60 °C to dry for 30 minutes. The chamber was then UV treated in a UV cleaner for 30 minutes to increase surface hydrophilicity. The cell regions of the lanes were treated with 50 µg/mL of Type I Rat Collagen (BD biosciences) in sterile 0.1% acetic acid for 1 hour at room temperature. Either human dermal fibroblasts or lymphatic endothelial cells were seeded in the well at a density of 20,000 cells/well in 100 µL of EBM, and allowed to adhere for 30 minutes at 37 °C. Regional selection for cell

seeding was randomized to remove any bias inherent to the chambers that might preferentially direct worm taxis. The chamber was then centrally flooded with EBM and cultured for 2 hours at 37 °C. Thirty minutes prior to an experiment, the EBM was replaced with fresh EBM. Single worms were then introduced into the center regions via pipette. Worms were individually centered in the field of view and location was recorded within the user interface software. After all worms had been centered and located, the tracking system was initiated and worms were tracked for 3 hours. A halogen light source was used to illuminate the worm being imaged. The worm was only exposed to the light source when being tracked and was in complete darkness during all other time of the experiment (hence better mimicking *in vivo* light conditions). We used the device with four experimental conditions using two cell types as shown in **Figure 33C**. Tetramisole experiments followed the same procedure, except tetramisole (Sigma) was added to a lane to yield concentrations of 1.2 mM or 2.4 mM.

Post-Acquisition Analysis

Tracking the centroid and recording video for each worm within the device allowed us to extract various metrics describing worm motility both in the context of the entire lane as well as specific regions. '*Speed*' was calculated for each section of the device, to compare worm speed in different environments, and over the entire tracking period. Thrashing measurements were carried out by subtracting two subsequent frames with an interval of 66 ms apart to obtain a difference image. The resulting image was then binarized using a metric based thresholding approach. The mean intensity of the entire image was then calculated and summed for a complete cycle (30 frames total) to obtain the '*thrashing index*' metric (**Figure 34B**). In addition to the two motility metrics, the '*percentage of time spent*' in any given region was calculated. The '*persistence ratio*' was calculated by subtracting the final location of the worm at the end of the experiment from the location at the start and dividing by the total displacement of the worm during the entire 3-hour experiment. To determine the extent that the persistence ratio might change over time, the persistence ratio was also calculated over a 10 minute non-overlapping sliding window. Algorithms for determining the speed, time spent and

persistence ratio were written in MATLAB 2013 while LabVIEW 2013 was using for the trashing metric.

Statistical Analysis

A Kruskal-Wallis nonparametric test followed by Dunn's test to correct for multiple comparisons was used for statistical analysis of the *percentage of time spent* in each cell region. All other statistical tests were performed with a one-way ANOVA followed by a Tukey test to correct for multiple comparisons. All statistical analyses were performed in GraphPad Prism 6. $P \leqslant 0.05$ was considered statistically significant. Graphical P value designation was as follows: ($P \leqslant 0.05$) = *, ($P \leqslant 0.01$) = **, ($P \leqslant 0.001$) = *** and ($P \leqslant 0.0001$) = ****. All data is presented as mean ± standard deviation. Sample number is indicated in each figure caption where applicable.

6.4. Results

A scalable PDMS-based coculture choice chamber

The choice chamber allowed for co-culture of two cell types along with the L3 *B. malayi* thus creating a multicellular microenvironment for the worm. The aluminum mold used for the casts allows for repeated manufacturing of devices for a large number of experiments (**Figure 33A**). Microgrooves resulting from machining the mold had the advantage of providing a relatively rough surface, thus increasing friction, to potentially facilitate worm movement. Made of PDMS, the chamber was both biocompatible and optically clear allowing for both transmission and reflective imaging using an inverted microscope. The linear parallel lane configuration is also scalable to include more lanes per device if needed. The humidifying chamber, filled with sterile water or PBS, limited evaporation of the media (**Figure 33B**). Cells remained intact at the conclusion of the experiment with minimal signs of cytoskeletal remodeling as can be seen by the green actin stain of a representative image of the LECs and HDFs (**Figure 33D**).

An automated imaging platform for quantifying speed, thrashing and migratory behavior

We developed an *in vitro* imaging platform that was used to study the migration behavior of nematodes in a multicellular microenvironment. The tracking algorithm

provided the capability of imaging multiple worms under high magnification by imaging one worm at a time and then moving on to the next. If the worm was lost, then a search process was initiated to find the worm. A two-second video sequence was recorded along with the location of the worm during each cycle (**Figure 34A**). The system was built around a fully controllable environment in terms of both atmospheric CO_2 levels and temperature, which made it ideal for long-term experiments requiring prolonged monitoring and quantification. With our current 7-lane configuration and 2-second imaging window for each worm it took approximately 120 seconds for a full cycle (in which 7 worms were tracked and imaged) with the main time spent on the search algorithm to find the worm if it had left the FOV of the last known location. To demonstrate the sensitivity of the two metrics for detecting changes in worm behavior, we exposed L3 *B. malayi* to tetramisole, a known anthelminthic, and showed that both speed and thrashing intensity decreased as a function of tetramisole concentration (**Figure 35**). At a concentration of 1.2 mM there was a 33% reduction in worm speed and a 37% reduction in thrashing. These values were increased to 70% for speed and 72% for thrashing when the concentration was increased to 2.4 mM. This change in speed was observed within 10 minutes of treatment with the tetramisole.

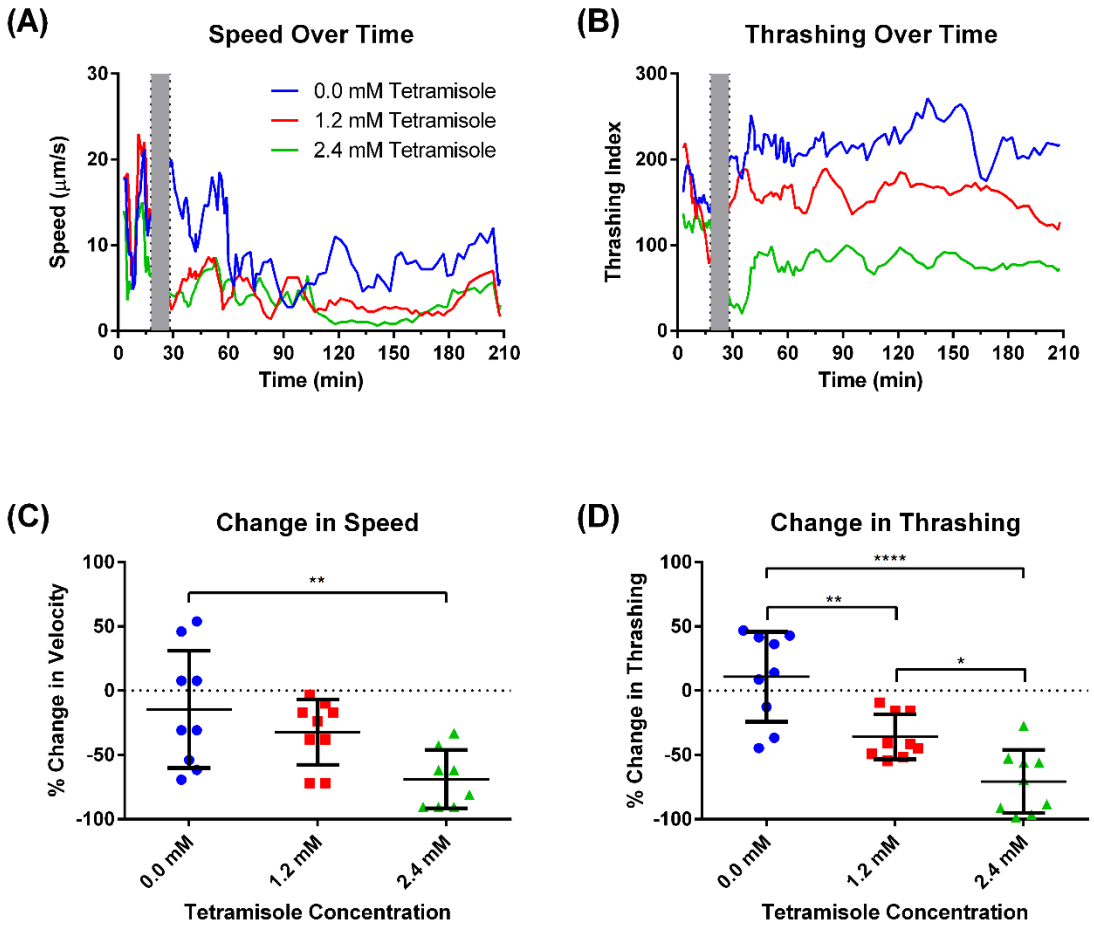

Figure 35: Tetramisole reduces both worm speed and thrashing. *Representative speed* ***(A)*** *and thrashing* ***(B)*** *over a 3-hour experimental period for three worms under different concentrations of tetramisole (0.0, 1.2 and 2.4 mM) as measured with our platform. Tetramisole is a known paralytic agent that affects nematode thrashing. The gray interval represents a 10-minute gap when the drug was added and imaging session restarted. Our platform can detect changes in both worm speed* ***(C)*** *and thrashing* ***(D)*** *after drug administration. While both speed and thrashing decreased as tetramisole concentration was increased, the thrashing metric was more sensitive to the changes in tetramisole concentration. N = 9, error bars represent standard deviation. Sample videos provided in supplemental materials.*

L3 B. malayi motility is altered in the presence of cells

The location data along with the video sequences allowed us to extract both the speed and thrashing intensity for each worm over time demonstrating that the L3 *B. malayi* maintained relatively constant motility throughout the experiment with a speed of around 10-15 μm/s (**Figure 36**). Worm speed was highest in the presence of LECs followed by HDFs (15 μm/s and 12 μm/s respectively). No difference in speed was found when both cell types were present versus no cells at all (**Figure 37A**). Thrashing was highest in the presence of LECs followed by HDFs and then when the two cell types were both present (**Figure 37B**). While the overall presence of cells within the device enhanced

worm motility, there was no difference in speed or thrashing when the worm was in physical contact with the cells, i.e. when the worm was in a given cell region (**Figure 38**). In addition, we found that in the case of a completely empty lane (no cells or collagen) the thrashing intensity correlated with speed to a high degree (Pearson correlation coefficient of 0.81) but the two metrics were no longer correlated when cells were present (Pearson correlation coefficients of 0.006 for HDFs + LECs, -0.049 for LECs alone and 0.12 for HDFs alone, **Figure 39**).

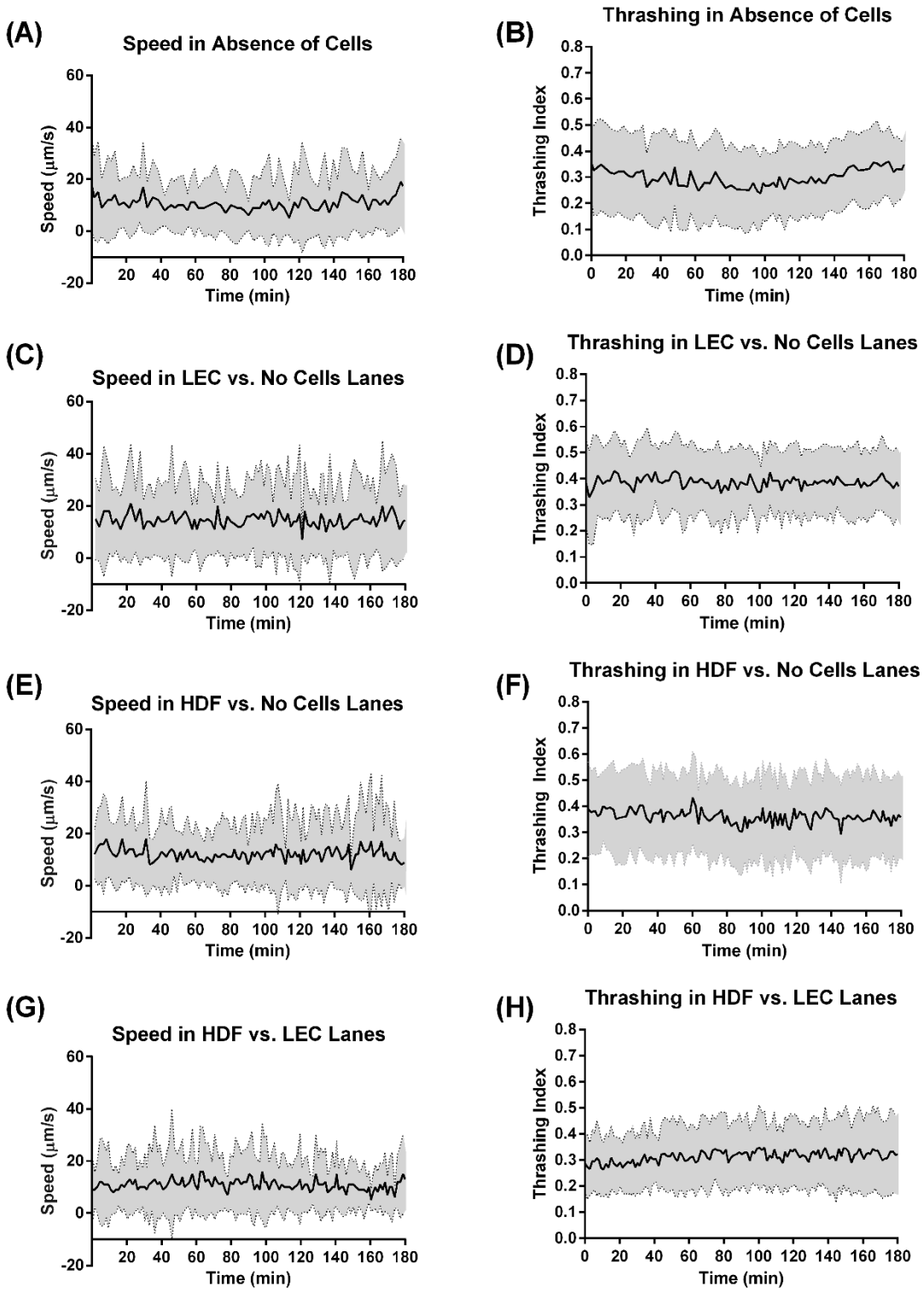

Figure 36: L3 B. malayi speed and thrashing, over a 3-hour experimental session, remain constant. (A-H) *Speed and thrashing plots over a 3-hour period under each lane condition. 1) Absence of cells: no cells (nor collagen coating) present in the lane, 2) LECs vs. no cells: LECs on one well and collagen coating on the other, 3) HDFs vs. no cells: HDFs on one well and collagen coating on the other, and 4) HDFs vs. LECs: HDFs on one well and LECs on another. A relatively flat trend was seen for all cases indicating worms were viable and showed consistent behavior throughout the experimental time-frame. N ⩾ 28, error band represents standard deviation.*

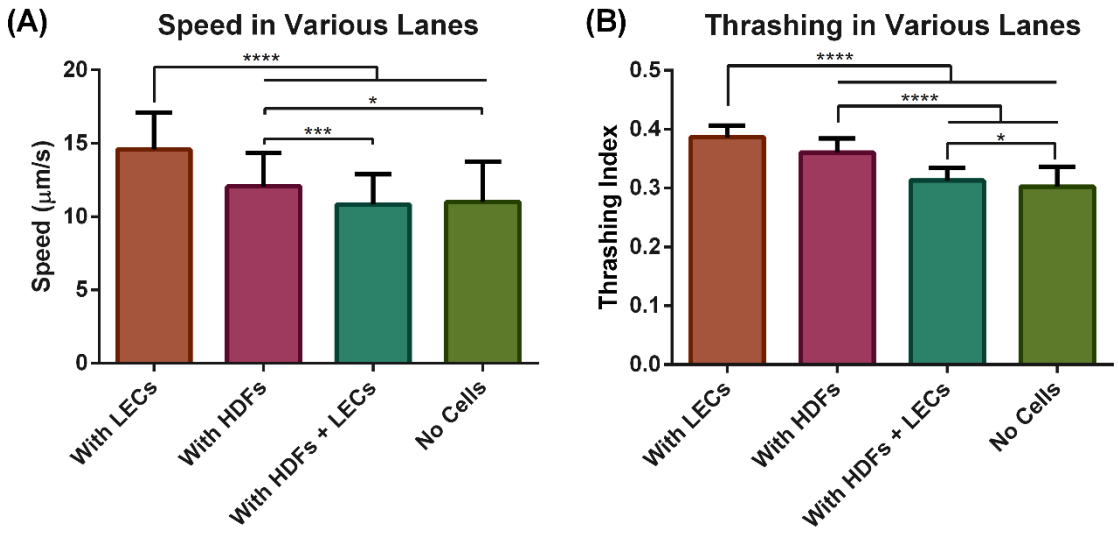

Figure 37: L3 B. malayi exhibit increased speed and thrashing in the presence of cells. *Average speed* ***(A)*** *and trashing* ***(B)*** *of the worms under different conditions: When there are 1) only LECs in the lane 2) only HDFs in the lane 3) both HDFs and LECs in the lane, and 4) no cells in the lane. The worms were most active when in the LEC lane. They were also more active when only one of the cell types was present compared to both being present in the same lane. N ⩾ 28, error bars represent standard deviation.*

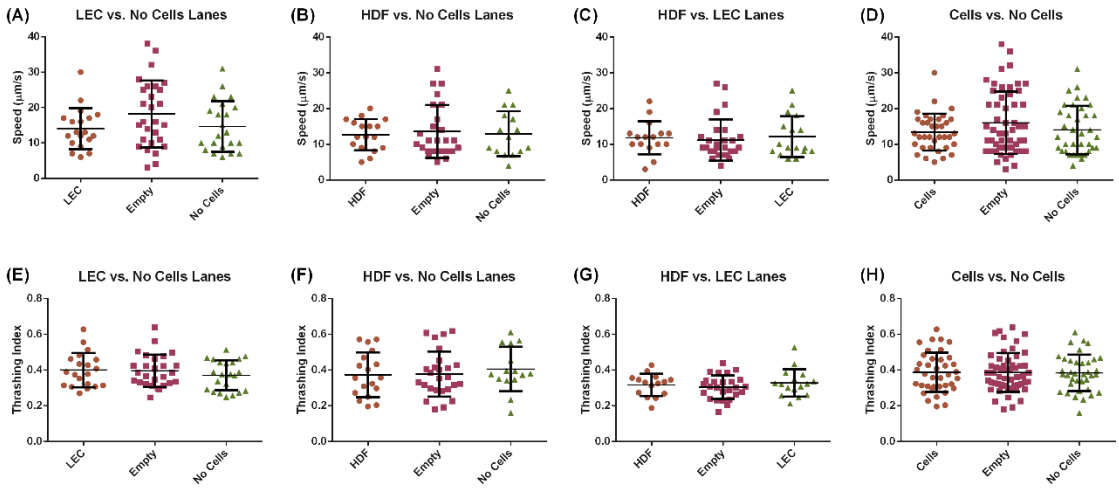

Figure 38: L3 B. malayi speed and thrashing are independent of physical contact with cells. *Speed of worms and thrashing behavior when in physical contact with LECs* ***(A, E),*** *HDFs* ***(B, F)****, HDFs + LECs* ***(C, G)*** *and combined data* ***(D, H)****. No statistical differences were observed. N ⩾ 28, error bars represent standard deviation.*

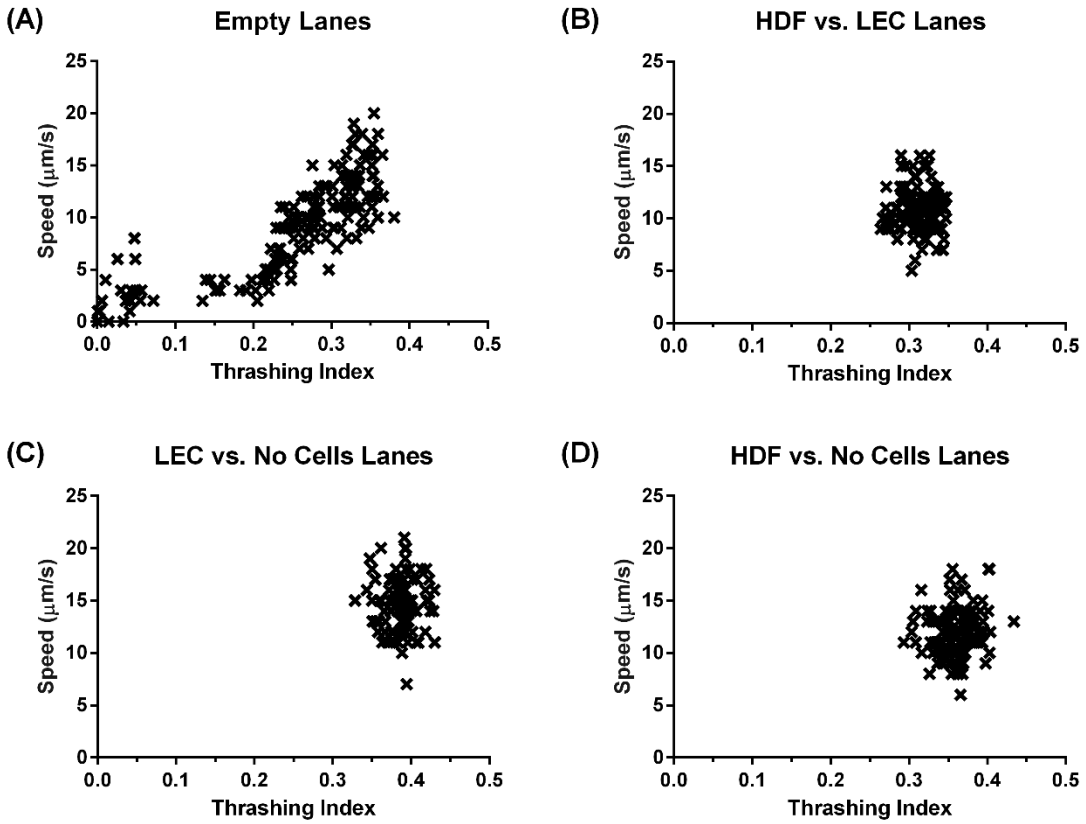

Figure 39: L3 B. malayi speed and thrashing are correlated in an empty lane, but not when cells are present. (A) *In the empty lanes thrashing correlated with speed (Pearson correlation coefficient; r = 0.81).* ***(B-D)*** *There was no correlation when there were cells in the lane (r = 0.006, -0.049 and 0.12 respectively) which covered 25% of the total lane area. N ⩾ 28.*

L3 B. malayi do not show targeted migration towards LECs or HDFs

In order to determine whether L3 *B. malayi* had a preference towards a certain cell type we quantified the percentage of time spent in each cellular region of the device. There was no preference towards a certain cell type as the worms spent equal time in all regions regardless of the culture conditions (**Figure 40**). To quantify the presence of any targeted migration we calculated the persistence ratio and found that the worms had very low persistence regardless of the culture conditions, suggesting that the worms' migration, while rather active, was fairly random (**Figure 41**A-E). This lack of targeted migration is further illustrated by a tracing of a typical worm's velocity, which oscillates back and forth as the worm continuously migrates up and down the lane (**Figure 41**).

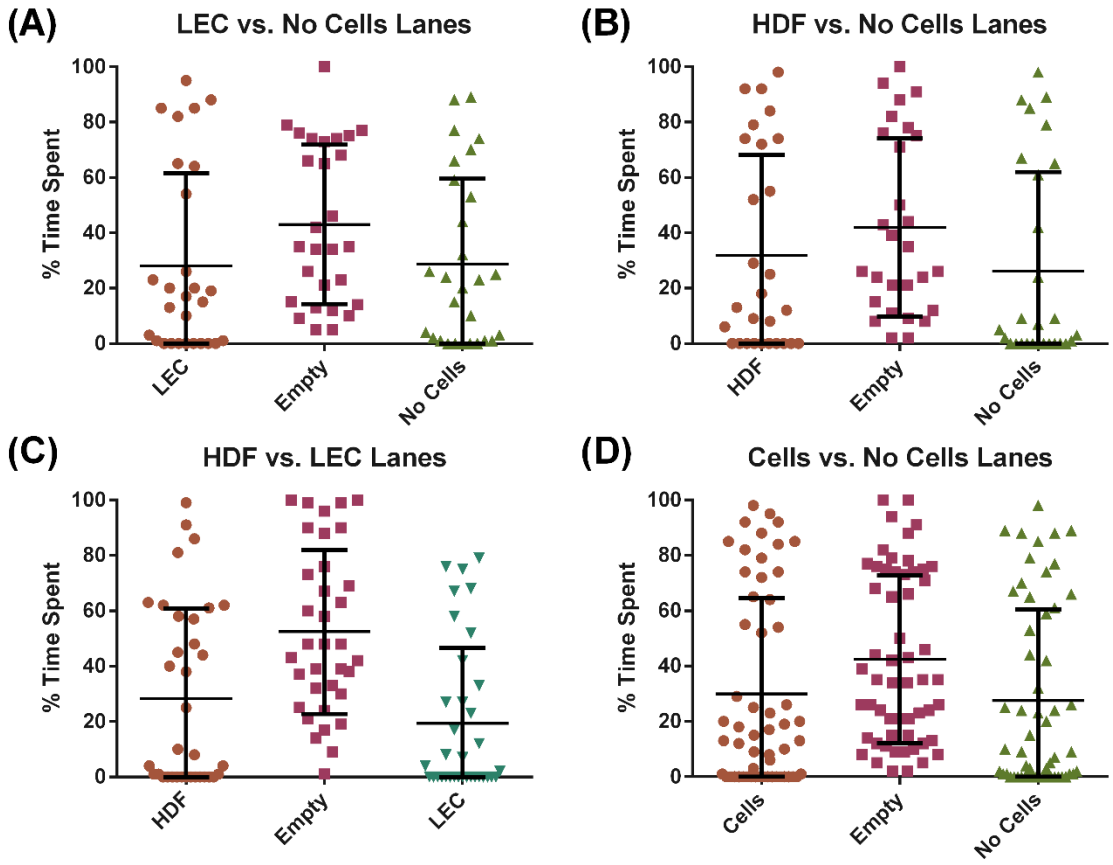

Figure 40: No difference in percentage of time spent by L3 B. malayi in each lane region. (A-D) *Cell (HDF or LEC) and no cell (only collagen coating) areas each cover 25% of the lane, while the empty region is 50% of the area. No statistical differences were observed when accounting for area differences. N ⩾ 28, error bars represent standard deviation.*

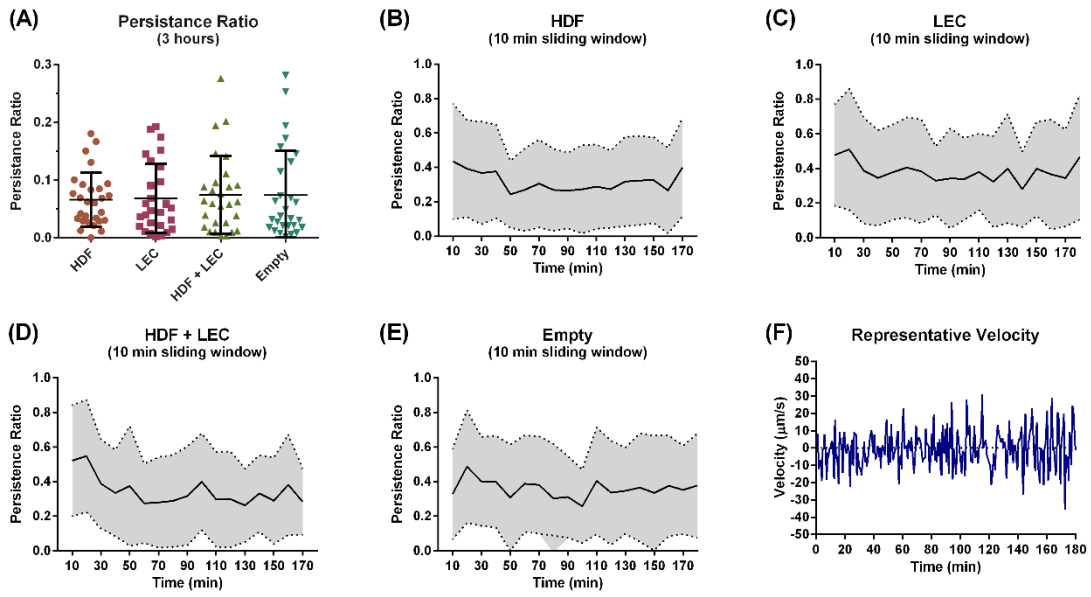

Figure 41: L3 B. malayi do not show targeted migration towards LECs or HDFs. (A) *The persistence ratio calculated over the entire time of the experiment (3 hours).* ***(B-E)*** *The persistence ratio calculating for a 10 minute non-overlapping sliding window.* ***(F)*** *A representative velocity plot for one worm illustrating the randomness in directionality. N ⩾ 28, error bars and bands represent standard deviation.*

6.5. Discussion

We demonstrated a platform for monitoring long-term nematode migration related behavior in a complex multicellular microenvironment that is potentially scalable for high through-put drug screening. The image acquisition system is flexible and surpasses most other published systems in acquisition capability [208]. The platform can be used with any nematode, including *C. elegans*, which are the most widely used model for studying nematode migration and behavior, since both tracking and analysis are independent of worm size and shape. Video is captured using a 640 x 480 pixel resolution camera but is capable of using any NI Vision compatible camera. Experiments were performed at a frame rate of 15 fps while the system is configurable to run at 60 fps without any reduction in resolution. The graphical user interface (GUI) is easy to use and requires minimal user intervention. The set-up is scalable to include any given number of lanes with the only limitation given by the minimum required dimensions of the lanes in order to encompass the given worm size and how much 'blind time' is acceptable between successive imaging cycles. From our experiments with the current device dimensions, the addition of each lane adds an average of 17 seconds of blind time as the

algorithm has an additional lane to scan and image. While the software is only compatible with current Zeiss manufactured microscopes, due to the fact that we utilized the Zeiss microscope SDK, it does provide us with full control of every part of the microscope. Due to the modular design of the control VIs, we can easily add full control of the fluorescent filter wheel, objective, focus, illumination and dual-camera ports for experiments requiring more complex image acquisition workflows. The PDMS-based choice chamber provides a cheap and robust platform for nematode behavioral assays in which their interaction with various cellular environments would be of interest. Although the worms are capable of moving on the surface of the PDMS a three dimensional matrix environment would better recapitulate the migratory environment the worm must traverse to reach the lymphatic [209–211]. This setup would provide the benefit of creating a more defined concentration gradient of any potential chemo-attractants released by cells, however, it is uncertain whether L3 B. *malayi* have the capability of moving through such an environment.

We demonstrated that L3 *B. malayi* exhibited an increase in motility, as defined by speed and thrashing, when cells are cultured with the worm. The worms seemed to be most motile when LECs were present, followed by HDFs and then followed by the two cell types together. Co-culture with specific cell types has been previously shown to enhance worm survival. Falcone et al. showed that by using Jurkat and HDFs as feeder cells, L3 *B. malayi* survival was dramatically increased and allowed L3s to mature into L4s *in vitro* [212]. Thus, the increased motility seen with our system could be resulting from the production of an (or several) important micronutrient or metabolite by the mammalian cells that is enabling increased worm motility. Given the limited information available regarding *B. malayi* sensory receptors we cannot at this time provide any further details regarding what molecules could be responsible for the modified behavior. What is interesting however, is that we have demonstrated that L3 *B. malayi* are capable of 'sensing' their multicellular environment, within minutes after exposure to cells, which suggests a cellular cue could play a role in determining their migration patterns and preference to reside in lymphatics. In addition to this rapid response in motility to cells, we

demonstrated that tetramisole, a paralytic agent commonly used to reduce nematode motility, reduced *B. malayi* motility within minutes of adding the drug to the worms. Thus the kinetics of action of tetramisole on *B. malayi* is comparable to *C. elegans,* which at similar drug concentrations usually show decreased motility within 15 minutes [213,214]. Thrashing is a common metric to quantify the effect of a drug in parasite studies and we have demonstrated that that our system can detect immediate changes in both thrashing and speed under a given drug. Therefore, the system can thus be used as a rapid drug screen for *B. malayi*, while at the same time culturing the worms in a multicellular environment. Additionally, there has been renewed interest in developing new methods of in vitro culture for filariasis nematodes that can support the support the entire life cycle of the worm. Traditional approaches have required worms to be cultured for weeks at a time to determine the culture supplements that result in the lowest worm death. Given that both cells and drugs produced a measureable (yet subtle) difference in worm behavior that could be immediately quantified, this system provides an ideal platform for pre-screening dozens of different culture conditions for optimizing an *in vitro* parasitic host environment including the presence of cell derived chemokines such as CXCL12 which was previously shown to enhance the growth of L4 filariae [215].

For the purpose of this study, we chose three widely used metrics to quantify behavior: speed, thrashing, and persistence ratio. In addition to these metrics, we determined the percentage of time spent at each cell type as a way of assessing whether L3 *B. malayi* had a certain preference for being in physical proximity to a given cell type. Our results indicated that L3 *B. malayi* did not have a preference towards a given cell type nor did they modify their motility (defined by both speed and thrashing) when in physical contact with LECs or HDFs. Interestingly, when cells are not present an increase in worm thrashing directly translates into an increase in worm speed, as suggested by the two parameters' high degree of correlation. The fact that this correlation is lost when cells are present, suggests that not only are the worms increasing their speed, but also that thrashing (as we have determined it) no longer is the driving mechanism determining worm migration. At the very least, the analysis capabilities of our platform provide the

ability to discriminate between very subtle changes in behavior that otherwise would not be apparent with traditional approaches. We then attempted to determine whether *B. malayi* exhibited directional guidance to lymphatic endothelial cells and found that they had no preference towards either cell type tested (LECs and HDFs). While chemotaxis through a gradient of CCL21 released by lymphatic endothelial cells has been shown to promote dendritic cell migration to lymphatic vessels [209,216,217], there are no known chemotactic molecule-receptor pairs identified for filarial parasites, much less ones that involve a lymphatic chemokine. Such chemotaxis of the larvae to serum, as shown previously, would support the hypothesis that chemotaxis can drive targeted migration [30,218,219]. However using our platform, chemotaxis does not seem to be the main contributor to migration towards lymphatics. This phenomenon could be due to the fact that stable chemokine gradients are not formed in our device due to the high diffusion coefficient of relevant chemokines in cell culture media. Other factors in the *in vivo* environment not captured in the current iteration of the device might play a large contribution to migration including the contents of lymph, the presence of immune cells, and interstitial flow (which is always directed towards the nearest draining lymphatic and has been implicated in lymphatic-targeting for other cell types [211,220,221]). In addition, worm movement within the dermis might be random until the worm encounters a point of entry into the lymphatics (i.e. collecting lymphatic vessels) which are large enough to encompass the worm and fragile enough to be penetrated given their thin walls.

6.6. Conclusion

The described platform provides a tool for parasitologists to explore mechanisms that drive L3 filarial worms to target lymphatic vessels, to screen for the efficacy of potential new drug compounds, and to engineer *in vitro* environments that provide a more viable host for long-term worm culture. While in its current form our study provides valuable insight by quantifying L3 *B. malayi* behavior both in the presence and absence of dermal specific cells, the *in vitro* platform needs to be further expanded to better capture key biophysical and biochemical aspects that are essential to the host environment including flow and concentration gradients. *In vivo* flow conditions can be replicated by

flowing media through the channels with the appropriate wall shear stress values. A stable diffusion gradient will be somewhat challenging without the incorporation of a 3D matrix but one possibility would be depositing an immobilized 2D gradient on the surface of PDMS [222] to test a given chemokine in question. While MDA has proven successful to an extent, the main limiting factor, second to non-compliance [223], is that the drugs used do not kill adult worms. Hence, it is crucial that as we move from control to elimination that we find new strategies to disrupt the transmission cycle. This shift requires understanding L3 *B. malayi* migration and the effects of drugs in an environment that mimics *in vivo* conditions with the goal of creating an environment close enough to the human host to ultimately culture *Wuchereria bancrofti*, the primary filarial species that is responsible for 90% of infections.

VII. CONCLUSION

In this scholarly work, we presented several novel engineering tools to study lymphatic pump function in the context of lipid uptake and for elucidating the behavior of the lymphatic specific filarial parasite known as *B. malayi*. Specifically, we developed an *in situ* imaging platform capable of simultaneous brightfield high-speed video acquisition and fluorescence imaging. Using custom-built image processing algorithms, the system allowed us to quantify the response of a rat mesenteric lymphatic vessel pump function to a post-prandial load. Utilizing the system we showed that contraction frequency and amplitude as well as average and end diastolic diameters decrease with an increase in lipid load. In order to clarify the contribution of viscosity to the post-prandial changes after a high-fat meal we utilized a microrheology approach to quantify the viscosity of lymph. To further elucidate the response of the lymphatic endothelium to the stimuli seen in the mesenteric vessels, mainly oscillatory shear and high lipid load, we utilized intracellular Ca^{2+} as a real-time output metric to quantify the response of lymphatic endothelial cells to these local stimuli *in vitro*. The animal model, imaging system and lymph characterization techniques developed pave the way for future studies exploring the role of mesenteric lymphatics in lipid absorption and transport, intestinal immune cell trafficking and in drug delivery targeting the lymphatics to avoid first pass metabolism.

With respect to our filariasis related work we developed an *in vitro* platform to quantify the migratory patterns of *B. malayi* and showed that within the limitations of the platform these parasites do not intentionally migrate towards lymphatic endothelial cells but once there they have a certain preference as indicated by their increased motility.

7.1. Contributions

This work can be summarized as having the following overall contributions:

- An imaging platform capable of acquiring both high-speed video and fluorescence images simultaneously.
- An image processing algorithm suitable for stabilizing high speed videos from the mesentery with large motion artifacts due to gut motility and respiration.
- A set of image processing algorithms to quantify lymphatic contraction, flow rates and lipid load.
- A rat animal model for the study of collecting vessel lymphatic lipid uptake.
- Establishing the use of BODIPY C_{16} as a real-time fluorescent lipid indicator.
- The insight that mesenteric lymphatic vessels reduce their contraction frequency, amplitude and both average and end diastolic diameters once exposed to high lipid loads.
- Post-prandial lymph viscosity values during absorption of a high-fat meal.
- The first evidence that intracellular Ca^{2+} in lymphatic endothelial cells varies with the type of shear stress waveform the cells exposed to and first evidence that mechano-regulation carried out by these cells is affected in the presence of VLDL.
- An *in vitro* platform for co-culture of filarial parasites with two other cell types.
- An automated worm tracking platform for long term tracking.
- Image processing algorithms for quantifying worm displacement and thrashing behavior.
- A low-cost imaging set-up for high-throughput screening of macrofilaricidal compounds on adult parasites.

7.2. Future Work

The major contribution of this thesis has been to provide a comprehensive toolset to study the role of lymphatics in lipid transport. While many new insights have been gained through the various studies presented in this work, many more questions remain. The imaging system developed paves the way for numerous studies investigating a range of questions ranging from characterizing the biomechanics of mesenteric collecting vessels to quantifying the uptake of various lipid based drug delivery vehicles targeting lymphatics. As a first step however, we see this system being adapted and scaled down to accommodate mouse animal models. This will open up a range of possibilities by using genetically modified mouse models to better understand the molecular mechanisms governing lymphatic pump function especially in the context of lipid absorption. On the software side, the amount of data collected from such experiments is very large and processing it is not currently very efficient. All the image processing algorithms need to be adapted for large-scale parallel processing utilizing high performance computing clusters. This should minimize analysis time from several days for each animal to as low as a couple of minutes. While we showed that collecting lymphatic vessels exhibited a decrease in pumping in response to a high lipid load, there remains many unknowns on the exact mechanisms regulating this. Further work needs to be carried out to clarify the exact mechanisms involved. We suggest taking an *in vitro* approach by investigating the role of lymphatic endothelial cells in mechano-regulation, by measuring the various effects that mechanical and lipid stimuli have on these cells especially on their signaling pathways and more importantly on their vasoactive substance release.

In addition to the above, there remains much work to be done to understand the behavior of filarial parasites. This includes developing more physiologically relevant i*n vitro* platforms that both mimic the lymphatic environment and provide real-time measuring capabilities. Depending on the complexity of such platforms, they can provide further insight into both the lymphatic pathophysiology that these parasites cause as well as developing ways to safely eliminate them within the human host.

APPENDIX A – MATLAB CODE

```
% This script conditions the velocity data for further
analysis. The signal
% is cleaned and smoothed.
% x is the time axis in seconds
% y is the velocity value in mm/sec
% Output is the background subtracted and smoothed signal
% Last updated 08/05/13 by Timothy Kassis

function [yyy] = ProcessVelocity(x,y)
%% Condition the waveform
% Remove values below or above a threshold
indices = find(abs(y)>3000);
y(indices) = NaN;

% Create a mask of where there are values for later use
ymsk = ones(length(y),1);
indices2 = find(isnan(y));
indices3 = find(~isnan(y));
ymsk(indices2) = NaN;
ymsk(indices3) = 1;

% Smooth the signal and apply mask
if all(isnan(y));
    yy = zeros(length(y),1);
    yyy = zeros(length(y),1);
else
yy = smooth(x,y,76,'rloess');
yyy = yy.*ymsk;
end

%% Output results and plots
[xx,ind] = sort(x);

subplot(2,1,1)
plot(xx,y(ind),'b.',xx,yy(ind),'r-')
legend('Original Data','Smoothed Data Using
''rloess''','Location','NW')
xlabel('Time (sec)')
ylabel('Velocity (um/s)')

subplot(2,1,2)
plot(xx,yyy(ind),'r-')
legend('Masked','Location','NW')
xlabel('Time (sec)')
ylabel('Velocity (um/s)')
```

```
% This function conditions the lipid data for further analysis.
% t is the time axis in seconds
% y is the intensity value (assuming taken every 5 seconds)
% Output is an array representing intensity values in minute
increments
% Last updated 09/12/14 by Timothy Kassis

function [ysmooth] = ProcessLipid(t,y)
%% Condition the waveform
ynew = ones((round(length(y)/12)),1).*NaN;
tnew = transpose(0:60:((length(ynew)*60)-1));
% Take highest 6 images in each rolling minute
j=2;
for i = 0:12:length(y)-12
    if i==0
        suby = y(1:12);
        sortedsuby = sort(suby,'descend');
        maxvalues = sortedsuby(1:6);
        ysample = nanmean(maxvalues);
        ynew(1,1) = ysample;
    else
        suby = y(i:i+12);
        sortedsuby = sort(suby,'descend');
        maxvalues = sortedsuby(1:6);
        ysample = nanmean(maxvalues);
        ynew(j,1) = ysample;

    end
    j=j+1;
end

ysmooth = smooth(ynew,7,'rlowess');

%% Output results and plots
[tt,ind] = sort(t);
[ttnew,ind2] = sort(tnew);

plot(tt,y(ind),'b*', ttnew,ysmooth(ind2),'k-', 'Linewidth', 2)
legend('Raw', 'Filtered Smoothed with
''rlowess''','Location','NW')
xlabel('Time (sec)')
ylabel('Fluorescence Intensity (AFU)')
```

```
% This script conditions the diameter data for further
analysis. The signal
% is cleaned and smoothed.
% Last updated 11/07/14 by Timothy Kassis
```

```
function yy = ProcessDiameter(t,y)
% Remove zero values
indices = y==0;
y(indices) = NaN;

% Remove values below or above a threshold
ymean = nanmean(y);
indices2 = y>(ymean+50) | y<(ymean-50);
y(indices2) = NaN;

% Smooth the signal
yy = smooth(t,y,100,'rlowess');
yy(1) = yy(2); % Replace the first value to avoid a NaN

% Output plots
[tt,ind] = sort(t);
plot(tt,y(ind),'b.',tt,yy(ind),'r-', 'LineWidth',2)
title('Diameter Tracing','FontSize',16);
legend('Original Data','Smoothed Data Using
''rlowess''','Location','NW')
xlabel('Time (sec)', 'FontSize',14)
ylabel('Diameter (um)', 'FontSize',14)
```

```
function [maxtab, mintab]=peakdet(v, delta, x)
%PEAKDET Detect peaks in a vector
%        [MAXTAB, MINTAB] = PEAKDET(V, DELTA) finds the local
%        maxima and minima ("peaks") in the vector V.
%        MAXTAB and MINTAB consists of two columns. Column 1
%        contains indices in V, and column 2 the found values.
%
%        With [MAXTAB, MINTAB] = PEAKDET(V, DELTA, X) the
indices
%        in MAXTAB and MINTAB are replaced with the
corresponding
%        X-values.
%
%        A point is considered a maximum peak if it has the
maximal
%        value, and was preceded (to the left) by a value lower
by
%        DELTA.

% Eli Billauer, 3.4.05 (Explicitly not copyrighted).
% This function is released to the public domain; Any use is
allowed.

maxtab = [];
mintab = [];

v = v(:); % Just in case this wasn't a proper vector
```

```
if nargin < 3
  x = (1:length(v))';
else
  x = x(:);
  if length(v)~= length(x)
    error('Input vectors v and x must have same length');
  end
end

if (length(delta(:)))>1
  error('Input argument DELTA must be a scalar');
end

if delta <= 0
  error('Input argument DELTA must be positive');
end

mn = Inf; mx = -Inf;
mnpos = NaN; mxpos = NaN;

lookformax = 1;

for i=1:length(v)
  this = v(i);
  if this > mx, mx = this; mxpos = x(i); end
  if this < mn, mn = this; mnpos = x(i); end

  if lookformax
    if this < mx-delta
      maxtab = [maxtab ; mxpos mx];
      mn = this; mnpos = x(i);
      lookformax = 0;
    end
  else
    if this > mn+delta
      mintab = [mintab ; mnpos mn];
      mx = this; mxpos = x(i);
      lookformax = 1;
    end
  end
end
```

```
% This function calculates contraction related data from the
diameter
% tracing and returns the following:
% 1- AD: Average diameter
% 2- CF: Average contraction frequency
% 3- CA: Average contraction amplitude
% 4- CAp: Average contraction amplitude percentage
```

```
% 5- MCA: Maximum contraction amplitude
% 6- MCAp: Maximum contraction amplitude percentage
% 7- EDD: End diastolic diameter
% 8- ESD: End systolic diameter
% 9- CWV: Average constriction wall velocity
% 10- DWV: Average dilation wall velocity
% 11- LV: Average lymphocyte velocity
% 12- MaxLV: Maximum lymphocyte velocity
% 13- MinLV: Minimum lymphocyte velocity
% 14- VFR: Average volumetric flow rate
% 15- MVFR: Maximum volumetric flow rate
% 16- WSS: Average wall shear stress
% 17- MWSS: Maximum wall shear stress
% 18- FPF: Fractional pump flow
% 19- EF: Ejection fraction
% 20- SV: Stroke volume
% 21- LO: Lymphatic output
% 22- VFRLO: VFR to LO ratio
% By Timothy Kassis last updated 08/05/13

function out = CalPar(t,d,v)

out = zeros(1,22);

% Peak detection
[maxtabout, mintabout]=peakdet(d,2,t);

% Set threshold for peaks
maxmindiff = sortrows([maxtabout; mintabout])
tempdiff = diff(maxmindiff)

for i = 1:length(tempdiff)
    if tempdiff(i) > 10
    maxtab(i) = maxtabout(i);
    mintab(i) = mintabout(i);
    else
    maxtab(i) = [];
    mintab(i) = [];
    end
end

% Calculate parameters
AD = nanmean(d);   % Average diameter
CF = length(maxtab)./max(t); % Average contraction frequency
maxminlist = sortrows([maxtab; mintab]);
temp = diff(maxminlist);
CA = mean(abs(temp));
CA = CA(2);     % Average contraction amplitude
CAp = (CA/AD)*100; % Average contraction amplitude percentage
MCA = max(abs(temp));
MCA = MCA(2);     % Maximum contraction amplitude
```

```
MCAp = (MCA/AD)*100; % Maximum contraction amplitude percentage
EDD = max(maxminlist);  % End diastolic diameter
ESD = min(maxminlist);  % End systolic diameter
wallvel = temp(:,2)./temp(:,1);
syscount = sum(wallvel<0);  % Number of systolic contractions
diascount = sum(wallvel>0);     % Number of diastolic
contractions
CWV = sum((wallvel<0).*wallvel)./syscount;    % Average wall
velocity during systole
DWV = sum((wallvel>0).*wallvel)./diascount;  % Average wall
velocity during diastole
LV = nanmean(v);    % Average lymphocyte velocity
MaxLV = max(v);     % Maximum lymphocyte velocity
MinLV = min(v);     % Minimum lymphocyte velocity
FR = ((pi * v .* (d.^2))/6) * 0.000036; % Flow rate
VFR = nanmean(FR);   % Average volumetric flow rate
MVFR = max(((pi * v .* (d.^2))/6) * 0.000036);    % Maximum
volumetric flow rate
WSS = nanmean((4*1.5*v)./(d/2)); % Wall shear stress
MWSS = max((4*1.5*v)./(d/2));    % Maximum wall shear stress
EF = (EDD(1,2)^2 - ESD(1,2)^2)/EDD(1,2)^2; % Ejection fraction
FPF = EF*CF*60; % Fractional pump flow
SV = pi*((EDD(1,2)/2)^2 - (ESD(1,2)/2)^2)*1000;   % Stroke
volume
LO = SV*CF; % Lymphatic output
VFRLO = VFR/LO; % VFR to LO ratio

% Store parameters
out(1,1) = AD;
out(1,2) = CF;
out(1,3) = CA;
out(1,4) = CAp;
out(1,5) = MCA;
out(1,6) = MCAp;
out(1,7) = EDD(1,2);
out(1,8) = ESD(1,2);
out(1,9) = abs(CWV);
out(1,10) = DWV;
out(1,11) = LV;
out(1,12) = MaxLV;
out(1,13) = MinLV;
out(1,14) = VFR;
out(1,15) = MVFR;
out(1,16) = WSS;
out(1,17) = MWSS;
out(1,18) = FPF;
out(1,19) = EF;
out(1,20) = SV;
out(1,21) = LO;
out(1,22) = VFRLO;
```

```
%% Plot
[tt,ind] = sort(t);

% Diameter tracing and peaks
subplot(3,1,1)
plot(tt,d(ind), 'b-', 'Linewidth', 2);
hold on;
plot(mintab(:,1), mintab(:,2), 'g*');
plot(maxtab(:,1), maxtab(:,2), 'r*');
title('Diameter Tracing');
ylabel('Diameter (um)')
hold off;

% Lymphocyte velocity
subplot(3,1,2)
plot(tt,v(ind),'r-','Linewidth', 2)
title('Lymphocyte Velocity');
ylabel('Velocity (um/s)')

% Flow rate
subplot(3,1,3)
plot(tt,FR(ind),'g-','Linewidth', 2)
title('Volume Flow Rate');
xlabel('Time (sec)')
ylabel('Flow Rate (ul/hr)')
```

```
% This function calculates contraction related data from the
diameter
% tracing and returns the following:
% 1- AD: Average diameter
% 2- CF: Contraction frequency
% 3- CA: Average contraction amplitude
% 4- CAp: Average contraction amplitude percentage
% 5- MCA: Maximum contraction amplitude
% 6- MCAp: Maximum contraction amplitude percentage
% 7- EDD: End diastolic diameter
% 8- ESD: End systolic diameter
% 9- CWV: Average constriction wall velocity
% 10- DWV: Average dilation wall velocity

% By Timothy Kassis last updated 11/07/14

function Diameter_Out = CalDiameter(t,d)

Diameter_Out = zeros(1,10);

% Peak detection
[maxtab, mintab]=peakdet(d,4,t);

% Calculate parameters
```

```
AD = nanmean(d);   % Average diameter
CF = length(mintab)./max(t); % Average contraction frequency
maxminlist = sortrows([maxtab; mintab]);
temp = diff(maxminlist);
CA = mean(abs(temp));
CA = CA(2);     % Average contraction amplitude
CAp = (CA/AD)*100; % Average contraction amplitude percentage
MCA = max(abs(temp));
MCA = MCA(2);     % Maximum contraction amplitude
MCAp = (MCA/AD)*100; % Maximum contraction amplitude percentage
EDD = mean(maxtab); % Average EDD
ESD = mean(mintab); % Average ESD
wallvel = temp(:,2)./temp(:,1);
syscount = sum(wallvel<0);  % Number of systolic contractions
diascount = sum(wallvel>0);     % Number of diastolic
contractions
CWV = sum((wallvel<0).*wallvel)./syscount;    % Average wall
velocity during systole
DWV = sum((wallvel>0).*wallvel)./diascount;  % Average wall
velocity during diastole

% Store parameters
Diameter_Out(1,1) = AD;
Diameter_Out(1,2) = CF;
Diameter_Out(1,3) = CA;
Diameter_Out(1,4) = CAp;
Diameter_Out(1,5) = MCA;
Diameter_Out(1,6) = MCAp;
Diameter_Out(1,7) = EDD(1,2);
Diameter_Out(1,8) = ESD(1,2);
Diameter_Out(1,9) = abs(CWV);
Diameter_Out(1,10) = DWV;


%% Plot
[tt,ind] = sort(t);

% Diameter tracing and peaks
subplot(3,1,1)
plot(tt,d(ind), 'b-', 'Linewidth', 2);
hold on;
plot(mintab(:,1), mintab(:,2), 'g*');
plot(maxtab(:,1), maxtab(:,2), 'r*');
title('Diameter Tracing');
ylabel('Diameter (um)')
hold off;
```

```
% Analyze all diameter data for a particular experiment
% By Timothy Kassis, last updated 11/07/14
```

```
myvars = who('Var*');
Results = cell(length(myvars),11);

Results{1,1} = 'TimePoint';
Results{1,2} = 'AD';
Results{1,3} = 'CF';
Results{1,4} = 'CA';
Results{1,5} = 'CAp';
Results{1,6} = 'MCA';
Results{1,7} = 'MCAp';
Results{1,8} = 'EDD';
Results{1,9} = 'ESD';
Results{1,10} = 'CWV';
Results{1,11} = 'DWV';

u = ones(length(Time),length(myvars)).*NaN;

fprintf('Processing diameter data\n');
for i = 1:length(myvars)
    fprintf('Processing video %d of %d\n',i,length(myvars));
    u(:,i) = ProcessDiameter(Time,eval(myvars{i,1}));
end

%%
for j = 1:length(myvars)
    fprintf('Calculating parameters for video %d of
%d\n',j,length(myvars));
    try              %# Attempt to perform computation
    out = CalDiameter(Time,u(:,j));
      catch   %# Catch the exception
          continue
    end

    Results{j+1,1} = myvars{j,1};
    Results{j+1,2} = out(1,1);
    Results{j+1,3} = out(1,2);
    Results{j+1,4} = out(1,3);
    Results{j+1,5} = out(1,4);
    Results{j+1,6} = out(1,5);
    Results{j+1,7} = out(1,6);
    Results{j+1,8} = out(1,7);
    Results{j+1,9} = out(1,8);
    Results{j+1,10} = out(1,9);
    Results{j+1,11} = out(1,10);
end
```

```
% Analyze all diameter data for a particular experiment
% By Timothy Kassis, last updated 11/07/14

myvars = who('Var*');
```

```
Results = cell(length(myvars),11);

Results{1,1} = 'TimePoint';
Results{1,2} = 'AD';
Results{1,3} = 'CF';
Results{1,4} = 'CA';
Results{1,5} = 'CAp';
Results{1,6} = 'MCA';
Results{1,7} = 'MCAp';
Results{1,8} = 'EDD';
Results{1,9} = 'ESD';
Results{1,10} = 'CWV';
Results{1,11} = 'DWV';

u = ones(length(Time),length(myvars)).*NaN;

fprintf('Processing diameter data\n');
for i = 1:length(myvars)
    fprintf('Processing video %d of %d\n',i,length(myvars));
    u(:,i) = ProcessDiameter(Time,eval(myvars{i,1}));
end

%%
for j = 1:length(myvars)
    fprintf('Calculating parameters for video %d of
%d\n',j,length(myvars));
    try              %# Attempt to perform computation
    out = CalDiameter(Time,u(:,j));
      catch   %# Catch the exception
          continue
    end

    Results{j+1,1} = myvars{j,1};
    Results{j+1,2} = out(1,1);
    Results{j+1,3} = out(1,2);
    Results{j+1,4} = out(1,3);
    Results{j+1,5} = out(1,4);
    Results{j+1,6} = out(1,5);
    Results{j+1,7} = out(1,6);
    Results{j+1,8} = out(1,7);
    Results{j+1,9} = out(1,8);
    Results{j+1,10} = out(1,9);
    Results{j+1,11} = out(1,10);
end
```

```
% This script conditions the velocity data for further
analysis. The signal
% is cleaned and smoothed.
% x is the time axis in seconds
% y is the velocity value in mm/sec
% Output is the background subtracted and smoothed signal
```

```
% Last updated 01/17/15 by Timothy Kassis

function [yyy] = ProcessVelocity2(x,y)
%% Condition the waveform
% Remove values below or above a threshold
indices = find(abs(y)>3000);
y(indices) = NaN;

% Create a mask of where there are values for later use
ymsk = ones(length(y),1);
indices2 = find(isnan(y));
indices3 = find(~isnan(y));
ymsk(indices2) = NaN;
ymsk(indices3) = 1;

% Smooth the signal and apply mask
if all(isnan(y));
    yy = zeros(length(y),1);
    yyy = zeros(length(y),1);
else
yy = smooth(x,y,76,'rloess');
yyy = yy.*ymsk;
end

%% Output results and plots
[xx,ind] = sort(x);

subplot(2,1,1)
plot(xx,y(ind),'b.',xx,yy(ind),'r-')
legend('Original Data','Smoothed Data Using
''rloess'''','Location','NW')
xlabel('Time (sec)')
ylabel('Velocity (um/s)')

subplot(2,1,2)
plot(xx,yyy(ind),'r-')
legend('Masked','Location','NW')
xlabel('Time (sec)')
ylabel('Velocity (um/s)')
```

```
function out = CalVel(t,d,v)

out = zeros(1,3);

LV = nanmean(v);    % Average lymphocyte velocity
FR = ((pi * v .* (d.^2))/6) * 0.000036; % Flow rate
VFR = nanmean(FR);   % Average volumetric flow rate
WSS = nanmean((4*1.5*v)/(d/2)); % Wall shear stress
```

```
out(1,1) = LV;
out(1,2) = VFR;
out(1,3) = WSS;

[tt,ind] = sort(t);

% Lymphocyte velocity
subplot(3,1,2)
plot(tt,v(ind),'r-','Linewidth', 2)
title('Lymphocyte Velocity');
ylabel('Velocity (um/s)')

% Flow rate
subplot(3,1,3)
plot(tt,FR(ind),'g-','Linewidth', 2)
title('Volume Flow Rate');
xlabel('Time (sec)')
ylabel('Flow Rate (ul/hr)')
end
```

```
% Analyze all diameter data for a particular experiment
% By Timothy Kassis, last updated 11/07/14

myvars = who('Var*');
Results = cell(length(myvars),2);

Results{1,1} = 'TimePoint';
Results{1,2} = 'Velocity';

u = ones(length(Time),length(myvars)).*NaN;

fprintf('Processing velocity data\n');
for i = 1:length(myvars)
    fprintf('Processing video %d of %d\n',i,length(myvars));
    u(:,i) = ProcessVelocity2(Time,eval(myvars{i,1}));
end

%%
for j = 1:length(myvars)
    fprintf('Calculating parameters for video %d of
%d\n',j,length(myvars));
    Results{j+1,1} = myvars{j,1};
    Results{j+1,2} = nanmean(u(:,j));
 end
```

```
% Analyze all motion data for a particular experiment
% By Timothy Kassis, last updated 11/29/14
```

```
myvars = who('Var*');
Results = cell(length(myvars),3);

Results{1,1} = 'TimePoint';
Results{1,2} = 'Freq';
Results{1,3} = 'Amp';

u = ones(length(Time),length(myvars)).*NaN;

fprintf('Processing motion data\n');
for i = 1:length(myvars)
    fprintf('Processing video %d of %d\n',i,length(myvars));
    u(:,i) = ProcessMotion(Time,eval(myvars{i,1}));
end

%%
for j = 1:length(myvars)
    fprintf('Calculating parameters for video %d of
%d\n',j,length(myvars));
    try              %# Attempt to perform computation
    out = CalMotion(Time,u(:,j));
    catch   %# Catch the exception
          continue
    end

    Results{j+1,1} = myvars{j,1};
    Results{j+1,2} = out(1,1);
    Results{j+1,3} = out(1,2);
end
```

```
% Analyze all motion data for a particular experiment using the
% MeasurePeristalsisFFT function
% By Timothy Kassis, last updated 01/06/15

myvars = who('Var*');
Results = cell(length(myvars),8);

Results{1,1} = 'TimePoint';
Results{1,2} = 'Power';
Results{1,3} = 'F1';
Results{1,4} = 'A1';
Results{1,5} = 'P1';
Results{1,6} = 'F2';
Results{1,7} = 'A2';
Results{1,8} = 'P2';

%%
for j = 1:length(myvars)
```

```
    fprintf('Calculating parameters for video %d of
%d\n',j,length(myvars));
    try              %# Attempt to perform computation
    [P, F1, A1, P1, F2, A2, P2] =
MeasurePeristalsisFFT(eval(myvars{j,1}),250);
    catch   %# Catch the exception
          continue
    end

    Results{j+1,1} = myvars{j,1};
    Results{j+1,2} = P;
    Results{j+1,3} = F1;
    Results{j+1,4} = A1;
    Results{j+1,5} = P1;
    Results{j+1,6} = F2;
    Results{j+1,7} = A2;
    Results{j+1,8} = P2;
end
```

```
% This function calculates motion related data from the
diameter
% By Timothy Kassis last updated 11/29/14

function Motion_Out = CalMotion(t,d)

Motion_Out = zeros(1,2);

% Peak detection
[maxtab, mintab]=peakdet(d,4,t);

% Calculate parameters
Freq = length(mintab)./max(t); % Average contraction frequency
maxminlist = sortrows([maxtab; mintab]);
temp = diff(maxminlist);
Amp = mean(abs(temp));
Amp = Amp(2);     % Average contraction amplitude

% Store parameters
Motion_Out(1,1) = Freq;
Motion_Out(1,2) = Amp;


%% Plot
[tt,ind] = sort(t);

% Motion tracing and peaks
subplot(3,1,1)
plot(tt,d(ind), 'b-', 'Linewidth', 2);
```

```
hold on;
plot(mintab(:,1), mintab(:,2), 'g*');
plot(maxtab(:,1), maxtab(:,2), 'r*');
title('Motion Tracing');
ylabel('Displacement (Pixel)')
hold off;
```

```
% Script to measure intestinal peristalsis
% Function accepts input signal 'y' and sampling frequency 'Fs'
% By Timothy Kassis, last updated 01/06/15

function [P, F1, A1, P1, F2, A2, P2]  =
MeasurePeristalsisFFT(y,Fs)
%% Plot input signal
% y = VarName85;
% Fs = 250;
t = (0:length(y) - 1)/Fs;
figure(1)
plot(t,y)
xlabel('Time (s)')
ylabel('Amplitude')

%% Subtract the mean to concentrate on motion fluctuations.
Compute and plot the periodogram.
ynorm = y - mean(y);
[pxx,f] = periodogram(ynorm,[],[],Fs);
figure(2)
plot(f,pxx);
set(gca,'xlim',[0 2]) % Set maximum frequency plotted between
0-2 Hz
xlabel('Frequency (Hz)')
ylabel('Magnitude')

%% Determine the highest two frequency magnitudes (presumably
peristalsis and breathing)
[pk,amp] = findpeaks(pxx,'NPeaks',2,'SortStr','descend');
hold on
plot(f(amp),pk,'or')
hold off
f(amp(1))
f(amp(2))

F1 = f(amp(1));
F2 = f(amp(2));
A1 = amp(1);
A2 = amp(2);

%% Calculate signal power
pwrTot = bandpower(ynorm,Fs,[0 (Fs/2 -1)]);
Harmonic = {'F2';'F1'; 'Full Signal'};
```

```
Freqs = [f(amp(2)) f(amp(1)) 0]';
Power = zeros([3 1]);
for k = 1:2
    Power(k) = bandpower(ynorm,Fs,Freqs(k)+[-0.001 0.05]);
end
Power(3) = bandpower(ynorm,Fs,[0 (Fs/2 -1)]);
Percent = Power/pwrTot*100;
inDB = pow2db(Power);
T = table(Freqs,Power,Percent,inDB,'RowNames',Harmonic) % Put
data in table

P = inDB(3);
P1 = inDB(2);
P2 = inDB(1);
```

```
% This script conditions the motion data for further analysis.
The signal
% is cleaned and smoothed. Using only the x values for this
% Last updated 11/29/14 by Timothy Kassis

function yy = ProcessMotion(t,y)
% Remove zero values
indices = y==0;
y(indices) = NaN;

% Remove values below or above a threshold
ymean = nanmean(y);
indices2 = y>(ymean+100) | y<(ymean-100);
y(indices2) = NaN;

% Smooth the signal
yy = smooth(t,y,100,'rlowess');
yy(1) = yy(2); % Replace the first value to avoid a NaN

% Output plots
[tt,ind] = sort(t);
plot(tt,y(ind),'b.',tt,yy(ind),'r-', 'LineWidth',2)
title('X Displacement Tracing','FontSize',16);
legend('Original Data','Smoothed Data Using
''rlowess''','Location','NW')
xlabel('Time (sec)', 'FontSize',14)
ylabel('Displacement (pixels)', 'FontSize',14)
```

REFERENCES

1. Leak L V. The structure of lymphatic capillaries in lymph formation. *Fed Proc*. 1976;35:1863–1871.

2. Baluk P, Fuxe J, Hashizume H, et al. Functionally specialized junctions between endothelial cells of lymphatic vessels. *J Exp Med*. 2007;204(10):2349–2362. doi:10.1084/jem.20062596.

3. Trzewik J, Mallipattu SK, Artmann GM, Delano F a, Schmid-Schönbein GW. Evidence for a second valve system in lymphatics: endothelial microvalves. *FASEB J*. 2001;15(10):1711–1717. doi:10.1096/fj.01-0067com.

4. Van Helden DF, Zhao J. Lymphatic vasomotion. *Clin Exp Pharmacol Physiol*. 2000;27:1014–1018. doi:10.1046/j.1440-1681.2000.03368.x.

5. Von Der Weid PY, Zawieja DC. Lymphatic smooth muscle: The motor unit of lymph drainage. *Int J Biochem Cell Biol*. 2004;36(7):1147–1153. doi:10.1016/j.biocel.2003.12.008.

6. Mazzoni MC, Skalak TC, Schmid-Schönbein GW. Structure of lymphatic valves in the spinotrapezius muscle of the rat. *Blood Vessels*. 1987;24(6):304–312. doi:10.1159/000158707.

7. Gashev A a, Davis MJ, Zawieja DC. Inhibition of the active lymph pump by flow in rat mesenteric lymphatics and thoracic duct. *J Physiol*. 2002;540(3):1023–1037. doi:10.1113/jphysiol.2001.016642.

8. Dixon JB. Lymphatic lipid transport: Sewer or subway? *Trends Endocrinol Metab*. 2010;21(8):480–487. doi:10.1016/j.tem.2010.04.003.

9. Gashev A a. Lymphatic vessels: Pressure- and flow-dependent regulatory reactions. *Ann N Y Acad Sci*. 2008;1131:100–109. doi:10.1196/annals.1413.009.

10. Hargens a R, Zweifach BW. Contractile stimuli in collecting lymph vessels. *Am J Physiol*. 1977;233(1):H57–H65.

11. Gashev AA, Davis MJ, Delp MD, Zawieja DC. Regional variations of contractile activity in isolated rat lymphatics. *Microcirculation*. 2004;11(6):477–92. doi:10.1080/10739680490476033.

12. Stanton AWB, Modi S, Mellor RH, Levick JR, Mortimer PS. Recent advances in breast cancer-related lymphedema of the arm: lymphatic pump failure and predisposing factors. *Lymphat Res Biol*. 2009;7(1):29–45. doi:10.1089/lrb.2008.1026.

13. Bennuru S, Nutman TB. Lymphangiogenesis and lymphatic remodeling induced by filarial parasites: Implications for pathogenesis. *PLoS Pathog*. 2009;5(12):e1000688. doi:10.1371/journal.ppat.1000688.

14. Steven Alexander J, Chaitanya GV, Grisham MB, Boktor M. Emerging roles of lymphatics in inflammatory bowel disease. *Ann N Y Acad Sci*. 2010;1207:E75–E85. doi:10.1111/j.1749-6632.2010.05757.x.

15. Liou JC, Matney M, Anz-Meador P, Kessler DJ, Jansen M, Theall JR. The new NASA orbital debris engineering model ORDEM2000. *Eur Sp Agency, (Special Publ ESA SP*. 2001;1(Pt 1):309–313. doi:10.1042/.

16. Tso P, Balint J a. Formation and transport of chylomicrons by enterocytes to the lymphatics. *Am J Physiol*. 1986;250(6 Pt 1):G715–G726.

17. Mansbach CM, Gorelick F. Development and physiological regulation of intestinal lipid absorption. II. Dietary lipid absorption, complex lipid synthesis, and the intracellular packaging and secretion of chylomicrons. *Am J Physiol Gastrointest Liver Physiol*. 2007;293(4):G645–G650. doi:10.1152/ajpgi.00299.2007.

18. Dixon JB. Mechanisms of chylomicron uptake into lacteals. *Ann N Y Acad Sci*. 2010;1207:E52–7. doi:10.1111/j.1749-6632.2010.05716.x.

19. Mahmood Hussain M. A proposed model for the assembly of chylomicrons. *Atherosclerosis*. 2000;148(1):1–15. doi:10.1016/S0021-9150(99)00397-4.

20. Straarup EM, Porsgaard T, Mu H, Hansen CH, Høy CE. Lymphatic transport in rats of interesterified oils containing conjugated linoleic acids. *Lipids*. 2005;40(7):677–684. doi:10.1007/s11745-005-1430-0.

21. Tso P, Pitts V, Granger DN. Role of lymph flow in intestinal chylomicron transport. *Am J Physiol Gastrointest Liver Physiol*. 1985;249(1):21.

22. Miura S, Sekizuka E, Nagata H, et al. Increased lymphocyte transport by lipid absorption in rat mesenteric lymphatics. *Am J*. 1987.

23. Servelle M. Congenital malformation of the lymphatics of the small intestine. *J Cardiovasc Surg (Torino)*. 1991;32(2):159–165.

24. Harvey NL, Srinivasan RS, Dillard ME, et al. Lymphatic vascular defects promoted by Prox1 haploinsufficiency cause adult-onset obesity. *Nat Genet*. 2005;37(10):1072–1081. doi:10.1038/ng1642.

25. Vignes S, Bellanger J. Primary intestinal lymphangiectasia (Waldmann's disease). *Orphanet J Rare Dis*. 2008;3:5. doi:10.1186/1750-1172-3-5.

26. Karpanen T, Alitalo K. Molecular biology and pathology of lymphangiogenesis. *Annu Rev Pathol*. 2008;3:367–397. doi:10.1146/annurev.pathmechdis.3.121806.151515.

27. World Health Organization. Global programme to eliminate lymphatic filariasis: progress report, 2011. *Wkly Epidemiol Rec Relev épidémiologique Hebd*. 2012;(87):345–356.

28. Dennis DT, Dreyer G, Ismail MM, et al. Lymphatic filariasis: The disease and its control. Fifth report of the WHO Expert Committee on Filariasis. *World Heal Organ - Tech Rep Ser*. 1992.

29. Molyneux D. Tropical Lymphedemas—Control and Prevention. *N Engl J Med*. 2012:1169–1171. doi:10.1056/NEJMp1202011.

30. Kusaba T, Fujimaki Y, Vincent AL, Aoki Y. In vitro chemotaxis of Brugia pahangi infective larvae to the sera and hemolymph of mammals and lower animals. *Parasitol Int*. 2008;57(2):179–184. doi:10.1016/j.parint.2007.12.006.

31. Pani SP, Srividya a., Dhanda V. Clinical manifestations of bancroftian filariasis with special reference to lymphoedema grading. *Indian J Med Res*. 1995;102:114–118.

32. Babu S, Nutman TB. Immunopathogenesis of lymphatic filarial disease. *Semin Immunopathol*. 2012;34(6):847–861. doi:10.1007/s00281-012-0346-4.

33. Dreyer G, Norões J, Figueredo-Silva J, Piessens WF. Pathogenesis of lymphatic disease in bancroftian filariasis: A Clinical Perspective. *Parasitol Today*. 2000;16(1997):544–548. doi:10.1016/S0169-4758(00)01778-6.

34. Babu S, Blauvelt CP, Kumaraswami V, Nutman TB. Regulatory networks induced by live parasites impair both Th1 and Th2 pathways in patent lymphatic filariasis: implications for parasite persistence. *J Immunol*. 2006;176(5):3248–3256. doi:176/5/3248 [pii].

35. Hoerauf A, Satoguina J, Saeftel M, Specht S. Immunomodulation by filarial nematodes. *Parasite Immunol*. 2005;27(10-11):417–429. doi:10.1111/j.1365-3024.2005.00792.x.

36. Chakraborty S, Gurusamy M, Zawieja DC, Muthuchamy M. Lymphatic filariasis: Perspectives on lymphatic remodeling and contractile dysfunction in filarial disease pathogenesis. *Microcirculation*. 2013;20:349–364. doi:10.1111/micc.12031.

37. Schroeder JH, Simbi BH, Ford L, et al. Live Brugia malayi Microfilariae Inhibit Transendothelial Migration of Neutrophils and Monocytes. *PLoS Negl Trop Dis*. 2012;6(11):e1914. doi:10.1371/journal.pntd.0001914.

38. Weil GJ, Ramzy RMR. Diagnostic tools for filariasis elimination programs. *Trends Parasitol*. 2007;23(2):78–82. doi:10.1016/j.pt.2006.12.001.

39. Gyapong JO, Twum-Danso N a Y. Editorial: Global elimination of lymphatic filariasis: Fact or fantasy? *Trop Med Int Heal*. 2006;11(2):125–128. doi:10.1111/j.1365-3156.2005.01542.x.

40. Melrose W. Lymphatic filariasis: new insights into an old disease. *Int J Parasitol*. 2002.

41. Ramzy RMR, El Setouhy M, Helmy H, et al. Effect of yearly mass drug administration with diethylcarbamazine and albendazole on bancroftian filariasis in Egypt: A comprehensive assessment. *Lancet*. 2006;367:992–999. doi:10.1016/S0140-6736(06)68426-2.

42. Lakshmi V, Joseph SK, Srivastava S, et al. Antifilarial activity in vitro and in vivo of some flavonoids tested against Brugia malayi. *Acta Trop*. 2010;116(2):127–133. doi:10.1016/j.actatropica.2010.06.006.

43. Pfarr KM, Debrah a. Y, Specht S, Hoerauf a. Filariasis and lymphoedema. *Parasite Immunol*. 2009;31(11):664–672. doi:10.1111/j.1365-3024.2009.01133.x.

44. Ottesen E a., Duke BOL, Karam M, Behbehani K. Strategies and tools for the control/elimination of lymphatic filariasis. *Bull World Health Organ*. 1997;75(6):491–503.

45. Rao RU, Huang Y, Fischer K, Fischer PU, Weil GJ. Brugia malayi: Effects of nitazoxanide and tizoxanide on adult worms and microfilariae of filarial nematodes. *Exp Parasitol*. 2009;121(1):38–45. doi:10.1016/j.exppara.2008.09.020.

46. Addiss DG, Louis-Charles J, Roberts J, et al. Feasibility and effectiveness of basic lymphedema management in Leogane, Haiti, an area endemic for bancroftian filariasis. *PLoS Negl Trop Dis*. 2010;4(4):e668. doi:10.1371/journal.pntd.0000668.

47. Dixon JB, Raghunathan S, Swartz MA. A tissue-engineered model of the intestinal lacteal for evaluating lipid transport by lymphatics. *Biotechnol Bioeng*. 2009;103(6):1224–1235. doi:10.1002/bit.22337.

48. Olszewski W, Machowski Z, Sokolowski J, Nielubowicz J. Experimental lymphedema in dogs. *J Cardiovasc Surg (Torino)*. 1968;9(2):178–183.

49. Hayashi a, Johnston MG, Nelson W, Hamilton S, McHale NG. Increased intrinsic pumping of intestinal lymphatics following hemorrhage in anesthetized sheep. *Circ Res*. 1987;60(2):265–272. doi:10.1161/01.RES.60.2.265.

50. McHale NG, Adair TH. Reflex modulation of lymphatic pumping in sheep. *Circ Res*. 1989;64(6):1165–1171. doi:10.1161/01.RES.64.6.1165.

51. Naito T, Ozawa Y, Tomoyasu M, et al. New method for evaluation of lung lymph flow rate with intact lymphatics in anaesthetized sheep. *Acta Physiol*. 2006;188(2):139–149. doi:10.1111/j.1748-1716.2006.01608.x.

52. Muthuchamy M, Gashev A, Boswell N, Dawson N, Zawieja D. Molecular and functional analyses of the contractile apparatus in lymphatic muscle. *FASEB J*. 2003;17(1):920–922. doi:10.1096/fj.02-0626fje.

53. Zawieja SD, Wang W, Wu X, Nepiyushchikh Z V., Zawieja DC, Muthuchamy M. Impairments in the intrinsic contractility of mesenteric collecting lymphatics in a rat model of metabolic syndrome. *AJP Hear Circ Physiol*. 2012;302(3):H643–H653. doi:10.1152/ajpheart.00606.2011.

54. Bohlen HG, Wang W, Gashev A, Gasheva O, Zawieja D. Phasic contractions of rat mesenteric lymphatics increase basal and phasic nitric oxide generation in vivo. *Am J Physiol Heart Circ Physiol*. 2009;297(4):H1319–H1328. doi:10.1152/ajpheart.00039.2009.

55. Lynch PM, Delano F a, Schmid-Schönbein GW. The primary valves in the initial lymphatics during inflammation. *Lymphat Res Biol*. 2007;5(1):3–10. doi:10.1089/lrb.2007.5102.

56. Karlsen T V, Karkkainen MJ, Alitalo K, Wiig H. Transcapillary fluid balance consequences of missing initial lymphatics studied in a mouse model of primary lymphoedema. *J Physiol*. 2006;574(Pt 2):583–596. doi:10.1113/jphysiol.2006.108308.

57. Lim HY, Rutkowski JM, Helft J, et al. Hypercholesterolemic mice exhibit lymphatic vessel dysfunction and degeneration. *Am J Pathol*. 2009;175(3):1328–1337. doi:10.2353/ajpath.2009.080963.

58. Karpanen T, Schulte-Merker S. Zebrafish Provides a Novel Model for Lymphatic Vascular Research. In: *Methods in Cell Biology*.Vol 105.; 2011:223–238. doi:10.1016/B978-0-12-381320-6.00009-6.

59. Yaniv K, Isogai S, Castranova D, Dye L, Hitomi J, Weinstein BM. Live imaging of lymphatic development in the zebrafish. *Nat Med*. 2006;12(6):711–716. doi:10.1038/nm1427.

60. Edwards G a, Porter CJ, Caliph SM, Khoo SM, Charman WN. Animal models for the study of intestinal lymphatic drug transport. *Adv Drug Deliv Rev*. 2001;50(1-2):45–60.

61. Bollman JL, Cain JC, Grindlay JH. Techniques for the collection of lymph from the liver, small intestine, or thoracic duct of the rat. *J Lab Clin Med*. 1948;33(10):1349–1352.

62. Dixon JB, Gashev A a., Zawieja DC, Moore JE, Coté GL. Image correlation algorithm for measuring lymphocyte velocity and diameter changes in contracting microlymphatics. *Ann Biomed Eng*. 2007;35(3):387–396. doi:10.1007/s10439-006-9225-2.

63. Akl TTJ, Nagai T, Coté GL, Gashev a. a. Mesenteric lymph flow in adult and aged rats. *Am J …*. 2011;76504(5):1828–1840. doi:10.1152/ajpheart.00538.2011.

64. Dixon JB, Zawieja DC, Gashev A a, Coté GL. Measuring microlymphatic flow using fast video microscopy. *J Biomed Opt*. 2005;10(6):064016. doi:10.1117/1.2135791.

65. Otis JP, Farber S a. Imaging vertebrate digestive function and lipid metabolism in vivo. *Drug Discov Today Dis Model*. 2013;10(xx):6–11. doi:10.1016/j.ddmod.2012.02.008.

66. Lewis HE. *Textbook of Medical Physiology*.; 1971.

67. Zitová B, Flusser J. Image registration methods: A survey. *Image Vis Comput*. 2003;21(11):977–1000. doi:10.1016/S0262-8856(03)00137-9.

68. Briers JD. Laser Doppler, speckle and related techniques for blood perfusion mapping and imaging. *Physiol Meas*. 2001;22(4):R35–R66. doi:10.1088/0967-3334/22/4/201.

69. Rossow MJ, Mantulin WW, Gratton E. Scanning laser image correlation for measurement of flow. *J Biomed Opt*. 2012;15(2):026003. doi:10.1117/1.3365946.

70. Dixon JB, Greiner ST, Gashev A a, Cote GL, Moore JE, Zawieja DC. Lymph flow, shear stress, and lymphocyte velocity in rat mesenteric prenodal lymphatics. *Microcirculation*. 2006;13(7):597–610. doi:10.1080/10739680600893909.

71. Rozenberg G. *Microscopic Haematology: A Practical Guide for the Haematology Laboratory*.; 2002.

72. Yang L, Li X, Ji Y, et al. Effect of ezetimibe on incretin secretion in response to the intestinal absorption of a mixed meal. *Am J Physiol Gastrointest Liver Physiol*. 2010;299(5):G1003–G1011. doi:10.1152/ajpgi.00294.2010.

73. Zawieja DC, Davis KL, Schuster R, Hinds WM, Granger HJ. Distribution, propagation, and coordination of contractile activity in lymphatics. *Am J Physiol*. 1993;264(4):H1283–H1291.

74. Nagai T, Bridenbaugh E a., Gashev A a. Aging-associated alterations in contractility of rat mesenteric lymphatic vessels. *Microcirculation*. 2011;18(6):463–473. doi:10.1111/j.1549-8719.2011.00107.x.

75. Rahbar E, Moore JE. A model of a radially expanding and contracting lymphangion. *J Biomech*. 2011;44(6):1001–1007. doi:10.1016/j.jbiomech.2011.02.018.

76. Burton-Opitz R, Nemser R. The Viscosity of Lymph. *Am J Physiol*. 1917;45(1):25–29.

77. Miller NE, Michel CC, Nanjee MN, et al. Secretion of adipokines by human adipose tissue in vivo: partitioning between capillary and lymphatic transport. *AJP Endocrinol Metab*. 2011;301(4):E659–E667. doi:10.1152/ajpendo.00058.2011.

78. Lakowicz JR. *Principles of Fluorescence Spectroscopy Principles of Fluorescence Spectroscopy*.; 2006. doi:10.1007/978-0-387-46312-4.

79. Breslin JW, Gaudreault N, Watson KD, Reynoso R, Yuan SY, Wu MH. Vascular endothelial growth factor-C stimulates the lymphatic pump by a VEGF receptor-3-dependent

mechanism. *Am J Physiol Hear Circ Physiol*. 2007;293(1):H709–18. doi:10.1152/ajpheart.00102.2007.

80. Akl TJ, Nepiyushchikh Z V, Gashev A a, Zawieja DC, Cot GL. Measuring contraction propagation and localizing pacemaker cells using high speed video microscopy. *J Biomed Opt*. 2011;16(2):026016. doi:10.1117/1.3544512.

81. Zhang F, Niu G, Lu G, Chen X. Preclinical lymphatic imaging. *Mol Imaging Biol*. 2011;13(4):599–612. doi:10.1007/s11307-010-0421-y.

82. Weiler M, Kassis T, Dixon JB. Sensitivity analysis of near-infrared functional lymphatic imaging. *J Biomed Opt*. 2012;17(6):066019. doi:10.1117/1.JBO.17.6.066019.

83. Schmid-Schönbein GW. Microlymphatics and lymph flow. *Physiol Rev*. 1990;70(4):987–1028.

84. Gashev A a. Basic mechanisms controlling lymph transport in the mesenteric lymphatic net. *Ann N Y Acad Sci*. 2010;1207:E21–8. doi:10.1111/j.1749-6632.2010.05708.x.

85. Thumser AE, Storch J. Characterization of a BODIPY-labeled fluorescent fatty acid analogue. Binding to fatty acid-binding proteins, intracellular localization, and metabolism. *Mol Cell Biochem*. 2007;299(1-2):67–73. doi:10.1007/s11010-005-9041-2.

86. Carten JD, Bradford MK, Farber SA. Visualizing digestive organ morphology and function using differential fatty acid metabolism in live zebrafish. *Dev Biol*. 2011;360(2):276–285. doi:10.1016/j.ydbio.2011.09.010.

87. Trevaskis NL, Charman WN, Porter CJH. Lipid-based delivery systems and intestinal lymphatic drug transport: A mechanistic update. *Adv Drug Deliv Rev*. 2008;60(6):702–716. doi:10.1016/j.addr.2007.09.007.

88. Yáñez J a., Wang SWJ, Knemeyer IW, Wirth M a., Alton KB. Intestinal lymphatic transport for drug delivery. *Adv Drug Deliv Rev*. 2011;63(10-11):923–942. doi:10.1016/j.addr.2011.05.019.

89. Trevaskis NL, Charman WN, Porter CJH. Acute hypertriglyceridemia promotes intestinal lymphatic lipid and drug transport: A positive feedback mechanism in lipid and drug absorption. *Mol Pharm*. 2011;8(4):1132–1139. doi:10.1021/mp100462d.

90. Phan CT, Tso P. Intestinal lipid absorption and transport. *Front Biosci*. 2001;6(5):D299–D319. doi:10.2741/Phan.

91. Physiol AJ, Metab E, Iqbal J, Hussain MM. Jahangir Iqbal and M. Mahmood Hussain. *Rev Lit Arts Am*. 2009;296(6):1183–1194. doi:10.1152/ajpendo.90899.2008.

92. Randolph G, Miller N. Lymphatic transport of high-density lipoproteins and chylomicrons. *J Clin Invest*. 2014;124(3):929–935. doi:10.1172/JCI71610.the.

93. Scallan JP, Davis MJ. Genetic removal of basal nitric oxide enhances contractile activity in isolated murine collecting lymphatic vessels. *J Physiol*. 2013;591(Pt 8):2139–2156. doi:10.1113/jphysiol.2012.250662.

94. Ribera J, Pauta M, Melgar-Lesmes P, et al. Increased nitric oxide production in lymphatic endothelial cells causes impairment of lymphatic drainage in cirrhotic rats. *Gut*. 2012. doi:10.1136/gutjnl-2011-300703.

95. Nizamutdinova IT, Maejima D, Nagai T, et al. Involvement of histamine in endothelium-dependent relaxation of mesenteric lymphatic vessels. *Microcirculation*. 2014;21(7):640–8. doi:10.1111/micc.12143.

96. Mizuno R, Koller a, Kaley G. Regulation of the vasomotor activity of lymph microvessels by nitric oxide and prostaglandins. *Am J Physiol*. 1998;274(3 Pt 2):R790–R796.

97. Takahashi N, Kawai Y, Ohhashi T. Effects of vasoconstrictive and vasodilative agents on lymphatic smooth muscles in isolated canine thoracic ducts. *J Pharmacol Exp Ther*. 1990;254:165–170.

98. Scallan JP, Wolpers JH, Davis MJ. Constriction of isolated collecting lymphatic vessels in response to acute increases in downstream pressure. *J Physiol*. 2013;591(Pt 2):443–59. doi:10.1113/jphysiol.2012.237909.

99. Davis MJ, Scallan JP, Wolpers JH, Muthuchamy M, Gashev a. a., Zawieja DC. Intrinsic increase in lymphangion muscle contractility in response to elevated afterload. *AJP Hear Circ Physiol*. 2012;303(7):H795–H808. doi:10.1152/ajpheart.01097.2011.

100. Ying L, Pin Y, Veronique A. Lipid Biology and Lymphatic Function: A Dynamic Interplay with Important Physiological and Pathological Consequences. *J Clin Cell Immunol*. 2014. doi:10.4172/2155-9899.1000261.

101. Harvey NL. The link between lymphatic function and adipose biology. *Ann N Y Acad Sci*. 2008;1131:82–88. doi:10.1196/annals.1413.007.

102. Blum KS, Karaman S, Proulx ST, et al. Chronic high-fat diet impairs collecting lymphatic vessel function in mice. *PLoS One*. 2014;9(4):e94713. doi:10.1371/journal.pone.0094713.

103. Weitman ES, Aschen SZ, Farias-Eisner G, et al. Obesity impairs lymphatic fluid transport and dendritic cell migration to lymph nodes. *PLoS One*. 2013;8(8):e70703. doi:10.1371/journal.pone.0070703.

104. Scallan JP, Hill MA, Davis MJ. Lymphatic Vascular Integrity is Disrupted in Type 2 Diabetes Due to Impaired Nitric Oxide Signaling. *Cardiovasc Res*. 2015.

105. Arngrim N, Simonsen L, Holst JJ, Bülow J. Reduced adipose tissue lymphatic drainage of macromolecules in obese subjects: a possible link between obesity and local tissue inflammation? *Int J Obes*. 2012;(February):1–3. doi:10.1038/ijo.2012.98.

106. Helyer LK, Varnic M, Le LW, Leong W, McCready D. Obesity is a risk factor for developing postoperative lymphedema in breast cancer patients. *Breast J*. 2010;16(1):48–54. doi:10.1111/j.1524-4741.2009.00855.x.

107. Greene AK, Grant FD, Slavin SA, Maclellan RA. Obesity-Induced Lymphedema: Clinical and Lymphoscintigraphic Features. *Plast Reconstr Surg*. 2015:1. doi:10.1097/PRS.0000000000001271.

108. Hayashi H, Sato Y, Kanai S, Ichikawa M, Funakoshi A, Miyasaka K. Increased lymphatic lipid transport in genetically diabetic obese rats. *Am J Physiol Gastrointest Liver Physiol*. 2002;282(1):G69–G76.

109. Savetsky IL, Torrisi JS, Cuzzone D a, et al. Obesity increases inflammation and impairs lymphatic function in a mouse model of lymphedema. *Am J Physiol Heart Circ Physiol*. 2014;307(2):H165–72. doi:10.1152/ajpheart.00244.2014.

110. Giannattasio C, Zoppo a., Gentile G, et al. Acute effect of high-fat meal on endothelial function in moderately dyslipidemic subjects. *Arterioscler Thromb Vasc Biol*. 2005;25(2):406–410. doi:10.1161/01.ATV.0000152231.93590.17.

111. Cooke CJ, Nanjee MN, Stepanova IP, Olszewski WL, Miller NE. Variations in lipid and apolipoprotein concentrations in human leg lymph: Effects of posture and physical exercise. *Atherosclerosis*. 2004;173(1):39–45. doi:10.1016/j.atherosclerosis.2003.07.004.

112. Brorson H, Ohlin K, Olsson G, Karlsson MK. Breast cancer-related chronic arm lymphedema is associated with excess adipose and muscle tissue. *Lymphat Res Biol*. 2009;7(1):3–10. doi:10.1089/lrb.2008.1022.

113. Rutkowski JM, Markhus CE, Gyenge CC, Alitalo K, Wiig H, Swartz M a. Dermal collagen and lipid deposition correlate with tissue swelling and hydraulic conductivity in murine primary lymphedema. *Am J Pathol*. 2010;176(3):1122–1129. doi:10.2353/ajpath.2010.090733.

114. Vuorio T, Nurmi H, Moulton K, et al. Lymphatic vessel insufficiency in hypercholesterolemic mice alters lipoprotein levels and promotes atherogenesis. *Arterioscler Thromb Vasc Biol*. 2014;34:1162–1170. doi:10.1161/ATVBAHA.114.302528.

115. Vedernikov YuP, Lankin VZ, Tikhaze a C, Vikhert a M. Lipoproteins as factors in vessel tone and reactivity modulation. *Basic Res Cardiol*. 1988;83(6):590–596. doi:10.1007/BF01906952.

116. Sorensen KE, Celermajer DS, Georgakopoulos D, Hatcher G, Betteridge DJ, Deanfield JE. Impairment of endothelium-dependent dilation is an early event in children with familial hypercholesterolemia and is related to the lipoprotein(a) level. *J Clin Invest*. 1994;93(January):50–55. doi:10.1172/JCI116983.

117. Kassis T, Kohan AB, Weiler MJ, et al. Dual-channel in-situ optical imaging system for quantifying lipid uptake and lymphatic pump function. *J Biomed Opt*. 2012;17(8):086005. doi:10.1117/1.JBO.17.8.086005.

118. Wang W, Nepiyushchikh Z, Zawieja DC, et al. Inhibition of myosin light chain phosphorylation decreases rat mesenteric lymphatic contractile activity. *Am J Physiol Heart Circ Physiol*. 2009;297(2):H726–H734. doi:10.1152/ajpheart.00312.2009.

119. Reed AL, Rowson S a., Dixon JB. Demonstration of ATP-dependent, transcellular transport of lipid across the lymphatic endothelium using an in vitro model of the lacteal. *Pharm Res*. 2013;30:3271–3280. doi:10.1007/s11095-013-1218-x.

120. Bucolo G, David H. Quantitative determination of serum triglycerides by the use of enzymes. *Clin Chem*. 1973;19(5):476–482.

121. Lovegrove J a, Griffin B a. The acute and long-term effects of dietary fatty acids on vascular function in health and disease. *Curr Opin Clin Nutr Metab Care*. 2013;16(2):162–7. doi:10.1097/MCO.0b013e32835c5f29.

122. Liao S, Cheng G, Conner D a., et al. Impaired lymphatic contraction associated with immunosuppression. *Proc Natl Acad Sci*. 2011;108(46):18784–18789. doi:10.1073/pnas.1116152108.

123. Davis MJ, Davis AM, Ku CW, Gashev A a. Myogenic constriction and dilation of isolated lymphatic vessels. *Am J Physiol Heart Circ Physiol*. 2009;296(2):H293–H302. doi:10.1152/ajpheart.01040.2008.

124. Johnston MG, Gordon JL. Regulation of lymphatic contractility by arachidonate metabolites. *Nature*. 1981;293:294–297. doi:10.1038/293294a0.

125. Dobbins DE, Buehn MJ, Dabney JM. Constriction of perfused lymphatics by acetylcholine, bradykinin and histamine. *Microcirc Endothelium Lymphatics*. 1990;6(6):409–425.

126. Soria P, Cuesta a, Romero H, Martínez FJ, Sastre a. Dietary treatment of lymphedema by restriction of long-chain triglycerides. *Angiology*. 1994;45:703–707. doi:10.1177/000331979404500805.

127. Swartz MA. The physiology of the lymphatic system. *Adv Drug Deliv Rev*. 2001;50(1-2):3–20. doi:S0169-409X(01)00150-8 [pii].

128. Kornuta J a., Dixon JB. Ex vivo lymphatic perfusion system for independently controlling pressure gradient and transmural pressure in isolated vessels. *Ann Biomed Eng*. 2014;42(8):1691–1704. doi:10.1007/s10439-014-1024-6.

129. Choi I, Lee S, Hong YK. The new era of the lymphatic system: No longer secondary to the blood vascular system. *Cold Spring Harb Perspect Med*. 2012;2. doi:10.1101/cshperspect.a006445.

130. Kesler CT, Liao S, Munn LL, Padera TP. Lymphatic vessels in health and disease. *Wiley Interdiscip Rev Syst Biol Med*. 2013;5(1):111–124. doi:10.1002/wsbm.1201.

131. Wiig H, Swartz M a. Interstitial Fluid and Lymph Formation and Transport: Physiological Regulation and Roles in Inflammation and Cancer. *Physiol Rev*. 2012;92(3):1005–1060. doi:10.1152/physrev.00037.2011.

132. Zawieja DC. Contractile physiology of lymphatics. *Lymphat Res Biol*. 2009;7(2):87–96. doi:10.1089/lrb.2009.0007.

133. Johnson NC, Dillard ME, Baluk P, et al. Lymphatic endothelial cell identity is reversible and its maintenance requires Prox1 activity. *Genes Dev*. 2008;22(23):3282–3291. doi:10.1101/gad.1727208.

134. Sabine A, Agalarov Y, Maby-ElHajjami H, et al. Mechanotransduction, PROX1, and FOXC2 Cooperate to Control Connexin37 and Calcineurin during Lymphatic-Valve Formation. *Dev Cell*. 2012;22:430–445. doi:10.1016/j.devcel.2011.12.020.

135. Lahdenranta J, Hagendoorn J, Padera TP, et al. Endothelial nitric oxide synthase mediates lymphangiogenesis and lymphatic metastasis. *Cancer Res*. 2009;69(7):2801–2808. doi:10.1158/0008-5472.CAN-08-4051.

136. Chen CY, Bertozzi C, Zou ZY, et al. Blood flow reprograms lymphatic vessels to blood vessels (vol 122, pg 2006, 2012). *J Clin Invest*. 2012;122:2702. doi:Doi 10.1172/Jci65314.

137. Von der Weid PY, Zhao J, Van Helden DF. Nitric oxide decreases pacemaker activity in lymphatic vessels of guinea pig mesentery. *Am J Physiol Heart Circ Physiol*. 2001;280(6):H2707–H2716.

138. Shirasawa Y, Ikomi F, Ohhashi T. Physiological roles of endogenous nitric oxide in lymphatic pump activity of rat mesentery in vivo. *Am J Physiol Gastrointest Liver Physiol*. 2000;278(4):G551–G556.

139. Gasheva OY, Zawieja DC, Gashev A a. Contraction-initiated NO-dependent lymphatic relaxation: a self-regulatory mechanism in rat thoracic duct. *J Physiol*. 2006;575(Pt 3):821–832. doi:10.1113/jphysiol.2006.115212.

140. Mansbach C, Gorelick F. physiological regulation of intestinal lipid absorption. II. Dietary lipid absorption, complex lipid synthesis, and the intracellular packaging and secretion of chylomicrons. *Am J Physiol …*. 2007;38163(4):645–650. doi:10.1152/ajpgi.00299.2007.

141. Kornuta J a., Nipper ME, Brandon Dixon J. Low-cost microcontroller platform for studying lymphatic biomechanics in vitro. *J Biomech*. 2013;46(1):183–186. doi:10.1016/j.jbiomech.2012.09.031.

142. Bouta EM, Wood RW, Perry SW, et al. Measuring intranodal pressure and lymph viscosity to elucidate mechanisms of arthritic flare and therapeutic outcomes. *Ann N Y Acad Sci*. 2011;1240:47–52. doi:10.1111/j.1749-6632.2011.06237.x.

143. Bouta EM, Wood RW, Brown EB, Rahimi H, Ritchlin CT, Schwarz EM. In vivo quantification of lymph viscosity and pressure in lymphatic vessels and draining lymph nodes of arthritic joints in mice. *J Physiol*. 2014;592:1213–23. doi:10.1113/jphysiol.2013.266700.

144. Kohan AB, Howles PN, Tso P. Methods for studying rodent intestinal lipoprotein production and metabolism. *Curr Protoc Mouse Biol*. 2012;2(September):219–230. doi:10.1002/9780470942390.mo120049.

145. Carpen IC, Brady JF. Microrheology of colloidal dispersions by Brownian dynamics simulations. *J Rheol (N Y N Y)*. 2005;49(6):1483. doi:10.1122/1.2085174.

146. Ortega F, Ritacco H, Rubio RG. Interfacial microrheology: Particle tracking and related techniques. *Curr Opin Colloid Interface Sci*. 2010;15(4):237–245. doi:10.1016/j.cocis.2010.03.001.

147. Waigh T a. Microrheology of complex fluids. *Reports Prog Phys*. 2005;68(3):685–742. doi:10.1088/0034-4885/68/3/R04.

148. Breedveld V, Pine DJ. Microrheology as a tool for high-throughput screening. *J Mater Sci*. 2003;38:4461–4470. doi:10.1023/A:1027321232318.

149. Weihs D, Mason TG, Teitell M a. Bio-microrheology: a frontier in microrheology. *Biophys J*. 2006;91(11):4296–4305. doi:10.1529/biophysj.106.081109.

150. Kim AJ, Manoharan VN, Crocker JC. Swelling-based method for preparing stable, functionalized polymer colloids. *J Am Chem Soc*. 2005;127(6):1592–1593. doi:10.1021/ja0450051.

151. Crocker J, Crocker J, Grier D. Methods of Digital Video Microscopy for Colloidal Studies. *J Colloid Interface Sci*. 1996;179(179):298–310. doi:10.1006/jcis.1996.0217.

152. Fantl P, Nelson JF. Coagulation in lymph. *J Physiol*. 1953;122:33–37.

153. Fedosov D a, Pan W, Caswell B, Gompper G, Karniadakis GE. Predicting human blood viscosity in silico. *Proc …*. 2011;108(29):11772–11777. doi:10.1073/pnas.1101210108/-/DCSupplemental.www.pnas.org/cgi/doi/10.1073/pnas.1101210108.

154. Irace C, Scavelli F, Carallo C, Serra R, Gnasso a. Plasma and blood viscosity in metabolic syndrome. *Nutr Metab Cardiovasc Dis*. 2009;19(7):476–480. doi:10.1016/j.numecd.2008.11.005.

155. Parkhurst KL, Lin H-F, DeVan a. E, Barnes JN, Tarumi T, Tanaka H. Contribution of blood viscosity in the assessment of flow-mediated dilation and arterial stiffness. *Vasc Med*. 2012;17(4):231–234. doi:10.1177/1358863X12450095.

156. Zhang J. Effect of plasma viscosity on blood flow behaviors in microvessels. *2011 Def Sci Res Conf Expo, DSR 2011*. 2011:1–4. doi:10.1109/DSR.2011.6026811.

157. Lee DH, Jung JM, Kim SY, Kim KT, Cho YI. Comparison tests for plasma viscosity measurements. *Int Commun Heat Mass Transf*. 2012;39(10):1474–1477. doi:10.1016/j.icheatmasstransfer.2012.10.018.

158. Gasheva OY, Knippa K, Nepiushchikh Z V, Muthuchamy M, Gashev A a. Age-related alterations of active pumping mechanisms in rat thoracic duct. *Microcirculation*. 2007;14(8):827–839. doi:10.1080/10739680701444065.

159. Weiler M, Dixon JB. Differential transport function of lymphatic vessels in the rat tail model and the long-term effects of indocyanine green as assessed with near-infrared imaging. *Front Physiol*. 2013;4 AUG(August):1–10. doi:10.3389/fphys.2013.00215.

160. Milling SWF, Jenkins C, MacPherson G. Collection of lymph-borne dendritic cells in the rat. *Nat Protoc*. 2006;1(5):2263–2270. doi:10.1038/nprot.2006.315.

161. Chung K, Cho JK, Park ES, Breedveld V, Lu H. Three-dimensional in situ temperature measurement in microsystems using brownian motion of nanoparticles. *Anal Chem*. 2009;81(3):991–999. doi:10.1021/ac802031j.

162. Porsgaard T, Kánský J, Mason S, Mu H. Size and number of lymph particles measured by a particle sizer during absorption of structured oils in rats. *Lipids*. 2005;40(3):273–279. doi:10.1007/s11745-005-1382-4.

163. Kohan AB, Wang F, Li X, et al. Apolipoprotein A-IV regulates chylomicron metabolism-mechanism and function. *Am J Physiol Gastrointest Liver Physiol*. 2012;302(6):G628–36. doi:10.1152/ajpgi.00225.2011.

164. Nutting F, Bergstedt S. Fat feeding increases size , but not number , of chylomicrons prod . uced by smal 1 intestine. *Animals*. 1990;259(5):709–719.

165. Rahbar E, Akl T, Coté GL, Moore JE, Zawieja DC. Lymph transport in rat mesenteric lymphatics experiencing edemagenic stress. *Microcirculation*. 2014;21(254):359–367. doi:10.1111/micc.12112.

166. Unthank JL, Bohlen HG. Lymphatic pathways and role of valves in lymph propulsion from small intestine. *Am J Physiol*. 1988;254(3):G389–G398.

167. Gashev A a., Zawieja DC. Hydrodynamic regulation of lymphatic transport and the impact of aging. *Pathophysiology*. 2010;17(4):277–287. doi:10.1016/j.pathophys.2009.09.002.

168. Taylor MS, Francis M. Decoding dynamic Ca(2+) signaling in the vascular endothelium. *Front Physiol*. 2014;5(November):447. doi:10.3389/fphys.2014.00447.

169. Thomas DD, Ridnour L a., Isenberg JS, et al. The chemical biology of nitric oxide: Implications in cellular signaling. *Free Radic Biol Med*. 2008;45(1):18–31. doi:10.1016/j.freeradbiomed.2008.03.020.

170. Bohlen HG. Nitric oxide and the cardiovascular system. *Compr Physiol*. 2015. doi:10.1002/cphy.c140052.

171. Jafarnejad M, Cromer WE, Kaunas RR, Zhang SL, Zawieja DC, Moore JE. Measurement of Shear Stress-Mediated Intracellular Calcium Dynamics in Human Dermal Lymphatic Endothelial Cells. *Am J Physiol - Hear Circ Physiol*. 2015;44(0):ajpheart.00744.2014. doi:10.1152/ajpheart.00744.2014.

172. Paredes RM, Etzler JC, Watts LT, Zheng W, Lechleiter JD. Chemical calcium indicators. *Methods*. 2008;46(3):143–151. doi:10.1016/j.ymeth.2008.09.025.

173. Gee KR, Brown K a, Chen WN, Bishop-Stewart J, Gray D, Johnson I. Chemical and physiological characterization of fluo-4 Ca(2+)-indicator dyes. *Cell Calcium*. 2000;27:97–106. doi:10.1054/ceca.1999.0095.

174. Kojima H, Nakatsubo N, Kikuchi K, et al. Detection and imaging of nitric oxide with novel fluorescent indicators: diaminofluoresceins. *Anal Chem*. 1998;70(13):2446–2453. doi:10.1021/ac9801723.

175. Edelstein AD, Tsuchida M a, Amodaj N, Pinkard H, Vale RD, Stuurman N. Advanced methods of microscope control using μManager software. *J Biol Methods*. 2014;1(2):1–10. doi:10.14440/jbm.2014.36.

176. Roy B, Das T, Mishra D, Maiti TK, Chakraborty S. Oscillatory shear stress induced calcium flickers in osteoblast cells. *Integr Biol*. 2014;6(3):289–299. doi:10.1039/C3IB40174J.

177. Wang C, Baker BM, Chen CS, Schwartz MA. Endothelial cell sensing of flow direction. *Arterioscler Thromb Vasc Biol*. 2013;33(9):2130–2136. doi:10.1161/ATVBAHA.113.301826.

178. Thomas D, Tovey SC, Collins TJ, Bootman MD, Berridge MJ, Lipp P. A comparison of fluorescent Ca2+ indicator properties and their use in measuring elementary and global Ca2+ signals. *Cell Calcium*. 2000;28(4):213–223. doi:10.1054/ceca.2000.0152.

179. Yang B, Rizzo V. Shear stress activates eNOS at the endothelial apical surface through β1 containing integrins and caveolae. *Cell Mol Bioeng*. 2013;6(3):346–354. doi:10.1007/s12195-013-0276-9.

180. Rizzo V, McIntosh DP, Oh P, Schnitzer JE. In situ flow activates endothelial nitric oxide synthase in luminal caveolae of endothelium with rapid caveolin dissociation and

calmodulin association. *J Biol Chem*. 1998;273(52):34724–34729. doi:10.1074/jbc.273.52.34724.

181. Chirgwin SR, Coleman SU, Klei TR. Brugia pahangi: In vivo tissue migration of early L3 alters gene expression. *Exp Parasitol*. 2008;118(1):89–95. doi:10.1016/j.exppara.2007.06.007.

182. Zuckerman BM, Jansson H. Nematode Chemotaxis and Possible Mechanisms of Host/Prey Recognition. *Annu Rev Phytopathol*. 1984;22(29):95–113. doi:10.1146/annurev.py.22.090184.000523.

183. Kotze a. C, Le Jambre LF, O'Grady J. A modified larval migration assay for detection of resistance to macrocyclic lactones in Haemonchus contortus, and drug screening with Trichostrongylidae parasites. *Vet Parasitol*. 2006;137(3-4):294–305. doi:10.1016/j.vetpar.2006.01.017.

184. Carr J a, Parashar A, Gibson R, Robertson AP, Martin RJ, Pandey S. A microfluidic platform for high-sensitivity, real-time drug screening on C. elegans and parasitic nematodes. *Lab Chip*. 2011;11(14):2385–2396. doi:10.1039/c1lc20170k.

185. Cronin C, Mendel J, Mukhtar S. An automated system for measuring parameters of nematode sinusoidal movement. *BMC …*. 2005;6:5. doi:10.1186/1471-2156-6-5.

186. Swierczek N a, Giles AC, Rankin CH, Kerr R a. High-throughput behavioral analysis in C. elegans. *Nat Methods*. 2011;8(7):592–598. doi:10.1038/nmeth.1625.

187. Marcellino C, Gut J, Lim KC, Singh R, McKerrow J, Sakanari J. WormAssay: A novel computer application for whole-plate motion-based screening of macroscopic parasites. *PLoS Negl Trop Dis*. 2012;6(1):e1494. doi:10.1371/journal.pntd.0001494.

188. Dusenbery DB. Using a microcomputer and video camera to simultaneously track 25 animals. *Comput Biol Med*. 1985;15(4):169–175. doi:10.1016/0010-4825(85)90058-7.

189. Feng Z, Cronin CJ, Wittig JH, Sternberg PW, Schafer WR. An imaging system for standardized quantitative analysis of C. elegans behavior. *BMC Bioinformatics*. 2004;5:115. doi:10.1186/1471-2105-5-115.

190. Tsechpenakis G, Bianchi L, Metaxas DN, Driscoll M. A novel computational approach for simultaneous tracking and feature extraction of C. elegans populations in fluid environments. *IEEE Trans Biomed Eng*. 2008;55(5):1539–1549. doi:10.1109/TBME.2008.918582.

191. Stephens GJ, Johnson-Kerner B, Bialek W, Ryu WS. Dimensionality and dynamics in the behavior of C. elegans. *PLoS Comput Biol*. 2008;4(4):e1000028. doi:10.1371/journal.pcbi.1000028.

192. Ramot D, Johnson BE, Berry TL, Carnell L, Goodman MB. The parallel worm tracker: A platform for measuring average speed and drug-induced paralysis in nematodes. *PLoS One*. 2008;3(5):e2208. doi:10.1371/journal.pone.0002208.

193. Sznitman R, Gupta M, Hager GD, Arratia PE, Sznitman J. Multi-environment model estimation for motility analysis of Caenorhabditis elegans. *PLoS One*. 2010;5(7):e11631. doi:10.1371/journal.pone.0011631.

194. Kotze a. C, Clifford S, O'Grady J, Behnke JM, Mccarthy JS. An in vitro larval motility assay to determine anthelmintic sensitivity for human hookworm and Strongyloides species. *Am J Trop Med Hyg*. 2004;71(5):608–616. doi:71/5/608 [pii].

195. Singh R, Pittas M, Heskia I, Xu F, McKerrow J, Caffrey CR. Automated image-based phenotypic screening for high-throughput drug discovery. *Proc - IEEE Symp Comput Med Syst*. 2009. doi:10.1109/CBMS.2009.5255338.

196. Smout MJ, Kotze AC, Mccarthy JS, Loukas A. A novel high throughput assay for anthelmintic drug screening and resistance diagnosis by real-time monitoring of parasite motility. *PLoS Negl Trop Dis*. 2010;4(11):e885. doi:10.1371/journal.pntd.0000885.

197. Pierce-Shimomura JT, Morse TM, Lockery SR. The fundamental role of pirouettes in Caenorhabditis elegans chemotaxis. *J Neurosci*. 1999;19(21):9557–9569.

198. Waggoner LE, Zhou GT, Schafer RW, Schafer WR. Control of alternative behavioral states by serotonin in Caenorhabditis elegans. *Neuron*. 1998;21(1):203–214. doi:10.1016/S0896-6273(00)80527-9.

199. Liewald JF, Brauner M, Stephens GJ, et al. Optogenetic analysis of synaptic function. *Nat Methods*. 2008;5(10):895–902. doi:10.1038/nmeth.1252.

200. Tsibidis GD, Tavernarakis N. Nemo: a computational tool for analyzing nematode locomotion. *BMC Neurosci*. 2007;8:86. doi:10.1186/1471-2202-8-86.

201. Stirman JN, Crane MM, Husson SJ, et al. Real-time multimodal optical control of neurons and muscles in freely behaving Caenorhabditis elegans. *Nat Methods*. 2011;8(2):153–158. doi:10.1038/nmeth.1555.

202. Leifer AM, Fang-Yen C, Gershow M, Alkema MJ, Samuel ADT. Optogenetic manipulation of neural activity in freely moving Caenorhabditis elegans. *Nat Methods*. 2011;8(2):147–152. doi:10.1038/nmeth.1554.

203. Shtonda BB, Avery L. Dietary choice behavior in Caenorhabditis elegans. *J Exp Biol*. 2006;209(Pt 1):89–102. doi:10.1242/jeb.01955.

204. Martin RJ, Verma S, Levandoski M, et al. Drug resistance and neurotransmitter receptors of nematodes: recent studies on the mode of action of levamisole. *Parasitology*. 2005;131 Suppl:S71–S84. doi:10.1017/S0031182005008668.

205. Martin RJ, Robertson AP, Buxton SK, Beech RN, Charvet CL, Neveu C. Levamisole receptors: A second awakening. *Trends Parasitol*. 2012;28(7):289–296. doi:10.1016/j.pt.2012.04.003.

206. Michalski ML, Griffiths KG, Williams S a., Kaplan RM, Moorhead AR. The NIH-NIAID filariasis research reagent resource center. *PLoS Negl Trop Dis*. 2011;5(11):e1261. doi:10.1371/journal.pntd.0001261.

207. Podgrabinska S, Braun P, Velasco P, Kloos B, Pepper MS, Skobe M. Molecular characterization of lymphatic endothelial cells. *Proc Natl Acad Sci U S A*. 2002;99(25):16069–16074. doi:10.1073/pnas.242401399.

208. Husson SJ, Costa WS, Schmitt C, Gottschalk A. Keeping track of worm trackers *. *WormBook*. 2012:1–17. doi:10.1895/wormbook.1.15.

209. Haessler U, Pisano M, Wu M, Swartz M a. Dendritic cell chemotaxis in 3D under defined chemokine gradients reveals differential response to ligands CCL21 and CCL19. *Proc Natl Acad Sci U S A*. 2011;108:5614–5619. doi:10.1073/pnas.1014920108.

210. Shin Y, Han S, Jeon JS, et al. Microfluidic assay for simultaneous culture of multiple cell types on surfaces or within hydrogels. *Nat Protoc*. 2012;7(7):1247–1259. doi:10.1038/nprot.2012.051.

211. Polacheck WJ, Charest JL, Kamm RD. Interstitial flow influences direction of tumor cell migration through competing mechanisms. *Proc Natl Acad Sci U S A*. 2011;108(27):11115–11120. doi:10.1073/pnas.1103581108.

212. Falcone FH, Zahner H, Schlaak M, Haas H. In vitro cultivation of third-stage larvae of Brugia malayi to the young adult stage. *Trop Med Parasitol*. 1995;46(4):230–234.

213. Liu P, Martin RJ, Dong L. Micro-electro-fluidic grids for nematodes: a lens-less, image-sensor-less approach for on-chip tracking of nematode locomotion. *Lab Chip*. 2013;13(4):650–61. doi:10.1039/c2lc41174a.

214. Buckingham SD, Sattelle DB. Fast, automated measurement of nematode swimming (thrashing) without morphometry. *BMC Neurosci*. 2009;10:84. doi:10.1186/1471-2202-10-84.

215. Bouchery T, Dénécé G, Attout T, et al. The Chemokine CXCL12 Is Essential for the Clearance of the Filaria Litomosoides sigmodontis in Resistant Mice. *PLoS One*. 2012;7(4):e34971. doi:10.1371/journal.pone.0034971.

216. Weber M, Hauschild R, Schwarz J, et al. Interstitial dendritic cell guidance by haptotactic chemokine gradients. *Science*. 2013;339(6117):328–32. doi:10.1126/science.1228456.

217. Randolph GJ, Angeli V, Swartz M a. Dendritic-cell trafficking to lymph nodes through lymphatic vessels. *Nat Rev Immunol*. 2005;5(8):617–628. doi:10.1038/nri1670.

218. Ewert a. Studies on the transfer of infective Brugia pahangi larvae from vector mosquitoes to the mammalian host. *Trans R Soc Trop Med Hyg*. 1967;61:110–113. doi:10.1016/0035-9203(67)90060-0.

219. Gunawardena NK, Fujimaki Y, Aoki Y. Chemotactic response of Brugia pahangi infective larvae to jird serum in vitro. *Parasitol Res*. 2003;90(4):337–342. doi:10.1007/s00436-003-0838-1.

220. Shields JD, Fleury ME, Yong C, Tomei A a., Randolph GJ, Swartz M a. Autologous Chemotaxis as a Mechanism of Tumor Cell Homing to Lymphatics via Interstitial Flow and Autocrine CCR7 Signaling. *Cancer Cell*. 2007;11(6):526–538. doi:10.1016/j.ccr.2007.04.020.

221. Haessler U, Teo JCM, Foretay D, Renaud P, Swartz M a. Migration dynamics of breast cancer cells in a tunable 3D interstitial flow chamber. *Integr Biol*. 2012;4(4):401. doi:10.1039/c1ib00128k.

222. Efimenko K, Genzer J. How to prepare tunable planar molecular chemical gradients. *Adv Mater*. 2001;13(20):1560–1563. doi:10.1002/1521-4095(200110)13:20<1560::AID-ADMA1560>3.0.CO;2-Z.

223. Boyd A, Won KY, McClintock SK, et al. A community-based study of factors associated with continuing transmission of lymphatic filariasis in Leogane, Haiti. *PLoS Negl Trop Dis*. 2010;4(3):e640. doi:10.1371/journal.pntd.0000640.